APPROACHES TO SEPARATIONS USING SILICA COLLOIDAL MEMBRANES

by

Patricia Anne Argana Ignacio-de Leon

A dissertation submitted to the faculty of
The University of Utah
in partial fulfillment of the requirements for the degree of

Doctor of Philosophy

Department of Chemistry

The University of Utah

August 2012

The University of Utah Graduate School

STATEMENT OF DISSERTATION APPROVAL

The dissertation of **Patricia Anne Argana Ignacio-de Leon**

has been approved by the following supervisory committee members:

Ilya Zharov	, Chair	**04-27-2012** Date Approved
Peter J. Stang	, Member	**04-27-2012** Date Approved
Ryan E. Looper	, Member	**04-27-2012** Date Approved
Jennifer Shumaker-Parry	, Member	**04-27-2012** Date Approved
Debra Mascaro	, Member	**04-27-2012** Date Approved

and by **Henry S. White** , Chair of the Department of **Chemistry**

and by Charles A. Wight, Dean of The Graduate School.

ABSTRACT

This thesis describes the synthesis and properties of free-standing nanoporous silica colloidal membranes where the molecular transport is controlled on the basis of size, charge, and chiral selectivity. To achieve this, free-standing membranes were prepared from colloidal solutions of silica nanospheres and the nanopore size and surface functionality were varied.

First, Au-coated membranes were prepared and the transport of neutral and charged small molecules through Au-coated silica colloidal membranes modified with poly(methacrylic acid) was studied. Polymer length was controlled by polymerization time to produce pH- and ion-responsive brushes inside the nanopores. By monitoring the flux of a diffusing species, it was demonstrated that the polyelectrolyte brush undergoes swelling and collapse when the pH is increased and decreased, respectively. We also observed an expansion and contraction in the absence and presence of counterions (e.g., $Na^{+}_{(aq)}$ and cationic dye Rhodamine B), respectively.

We studied the transport of enantiomers of a chiral dye molecule through silica colloidal membranes with attached chiral moieties. We used small molecules and polymers of amino acid derivatives and chiral calixarenes capable of chiral recognition as a result of stereochemically dependent noncovalent interactions with the diffusing molecule. We found that the selectivity remains approximately the same for membranes modified with small molecules and with polymers. This suggests that enantiopermselectivity depends primarily on the strength of noncovalent interactions rather than the availability of recognition sites.

Next, the transport of various generations of dendrimers through silica colloidal membranes was studied in a proof-of-concept experiment to demonstrate the size-selectivity of

our materials. Smaller dendrimers were found to diffuse faster and selectivity is improved by using smaller nanopores.

Finally, the transport of proteins through silica colloidal membranes was studied as a function of nanopore size and surface functionality. Poly(ethylene glycol) chains were attached inside the nanopores to minimize nonspecific protein adsorption. The membranes exhibit size-selectivity where smaller proteins generally diffused faster. From the results of this preliminary investigation, we propose that protein-nanopore interactions also affect diffusion rates and selectivity.

For Juliet Argana and Rodolfo Ignacio, Jr. and Joel de Leon

TABLE OF CONTENTS

LIST OF FIGURES

LIST OF TABLES

LIST OF ABBREVIATIONS

3-APTES	3-(Aminopropyl)triethoxysilane
3D	Three Dimension
ΔC	Concentration Gradient
δ	Chemical Shift
ε	Void Fraction
η	Viscosity of the Solution
λ_{max}	Wavelength of Maximum Absorbance
µg, mg, g	Microgram, Milligram, Gram
µM, mM, M	Micromolar, Millimolar, Molar
µm, nm, cm	Micrometer, Nanometer, Centimeter
µL, mL, L	Microliter, Milliliter, Liter
µmol, mmol, mol	Micromole, Millimole, Mole
τ	Tortuosity
ζ	Zeta Potential
-COOH	Carboxylic Acid
-NCS	Isothiocyanate
°C	Celsius Degree
A	Absorbance
a	Absorptivity of a Species
AAM	Anodic Alumina Membrane
AFM	Atomic Force Microscopy

Ag	Silver
Al	Aluminum
ATRP	Atom Transfer Radical Polymerization
Au	Gold
b	Path length
BHb	Bovine Hemogobin
Boc	*Tert*-Butyl Carbonate
BSA	Bovine Serum Albumin
C	Concentration
$CDCl_3$	Deuterochloroform
CH_2Cl_2	Dichloromethane
CH_3CN	Acetonitrile
$CHCl_3$	Chloroform
Cl	Chlorine
CNT	Carbon Nanotube
CTAB	Cetyltrimethylammonium Bromide
Cu	Copper
CuAAC	Copper(I)-Catalayzed Azide-Alkyne Cycloaddition
CuCl	Copper(I) Chloride
CV	Cyclic Voltammetry
D	Diffusion Coefficient
D_{eff}	Effective Diffusion Coefficient of the Species in Solution
D_{sol}	Diffusion Coefficient of the Species in Solution
DLS	Dynamic Light Scattering
DMF	*N*,*N*-Dimethylformamide
EDTA	Ethylenediaminetetraacetic Acid

EEDQ	*N*-Ethoxycarbonyl-2-ethoxy-1,2-dihydroquinoline
EtOH	Ethanol
eq.	Equivalent
fcc	Face Centered Cubic
Fc(CHO)	Ferrocenecarboxaldehyde
Fe	Iron
$Fe(bpy)_3^{2+}$	Tris(bipyridine)iron(II)
FFT, FT	Fourier Fast Transform, Fourier Transform
G	Generation
GC	Gas Chromatography
h	Hour
H	Proton
H_2O	Water
$HAuCl_4 \bullet 3H_2O$	Tetrachloroaurate(III) Trihydrate
HPLC	High Performance Liquid Chromatography
IR	Infrared
J	Flux
$J_{colloid}$	Flux through a Colloidal Membrane
K_2CO_3	Potassium Carbonate
k_B	Boltzmann Constant
kb	Kilobase
kDa	Kilodalton
$KHCO_3$	Potassium Bicarbonate
L	Membrane Thickness
Lz	Lysozyme
MΩ	Megaohm

Me_6TREN	Tris(2-aminoethyl)amine
MeOH	Methanol
$MgSO_4$	Magnesium Sulfate
MHz	Megahertz
MIP	Molecularly Imprinted Polymer
min	Minute
Mn	Manganese
mV	millivolt
MW	Molecular Weight
N_2	Nitrogen
Na_2CO_3	Sodium Carbonate
$NaBH_4$	Sodium Borohydride
$NaNO_3$	Sodium Nitrate
NaOH	Sodium Hydroxide
NBu_4OH	Tetrabutylammonium Hydroxide
NEt_3	Triethylamine
$NH_2OH•HCl$	Hydroxylamine Hydrochloride
NH_3	Ammonia
NH_4Cl	Ammonium Chloride
NH_4OH	Ammonium Hydroxide
Ni	Nickel
NMR	Nuclear Magnetic Resonance
PAMAM	Polyamidoamine
PCl_3	Phosphorus Trichloride
PEG	Poly(ethylene glycol)
pH	Negative Logarithm of the Hydrogen Ion Concentration

p*I*	Isoelectric Point of a Protein
pK_a	Negative Logarithm of the Acid Dissociation Constant
PMAA	Poly(methacrylic acid)
PNIPAAm	Poly(*N*-isopropylacrylamide)
Pt	Platinum
PTFE	Polytetrafluoroethylene
R_D	Diffusion Rate
R_f	Retention Factor
R_H	Stokes-Einstein Radius
RNA	Ribose Nucleic Acid
ROP	Ring Opening Polymerization
rpm	revolution per minute
RT	Room Temperature
S	Surface Area
s, sec	Second
SAM	Self-Assembled Monolayer
SEC	Size-Exclusion Chromatography
SEM	Scanning Electron Microscopy
Si	Silicon
SiO_2	Silica
ssDNA	Single Strand Deoxyribose Nucleic Acid
T	Temperature
TEM	Transmission Electron Microscopy
TEOS	Tetraethylorthosilicate
TFA	Trifluoroacetic Acid
TGA	Thermogravimetric Analysis

THF	Tetrahydrofuran
TLC	Thin Layer Chromatography
UV/Vis	Ultraviolet/Visible
wt %	Weight Percent
XPS	X-ray Photoelectron Spectroscopy

ACKNOWLEDGMENTS

With utmost respect and sincerity, I thank Dr. Ilya Zharov for his generous guidance, patience and encouragement. There is no other person who has helped me grow as a scientist as much as my advisor has, who has given me challenges and at the same time helped me overcome them. Thank you for accommodating all my questions and doubts, it is my honor and pleasure working with you. With much affection, I also thank the members of the Zharov Group, past and present, for the camaraderie and support. I wish everyone the best and thank you for making the lab a fun place to work in.

My gratitude extends to the Department of Chemistry at the University of Utah, particularly to my committee members for their invaluable suggestions and constructive criticism of this dissertation.

With much love, I am thankful to my family for their boundless love and warmest support. I especially thank my mother, Juliet Argana, and my father, Rodolfo Ignacio, Jr., for always being there for me and for believing in me; my brothers, Rodel and Rodolfo III, for the laughter despite the worries and cares. I always miss you. I would also like to thank my extended family especially Lionel de Leon and Frances de Leon for their encouraging prayers and support during this endeavor. My deepest thanks goes to my husband, Joel de Leon, for his patient love and comforting reminders that bore me through all.

Above all, I acknowledge and praise my Heavenly Father, the Lord God, apart from His grace and providence I can accomplish nothing.

CHAPTER 1

INTRODUCTION

Background and Significance

The transport of molecules, ions and particles across a semi-permeable barrier is a fascinating and important subject. The best examples of such transport include the complex processes by which living systems regulate the traffic of substances in and out of the cells. The desire and need to understand the underlying principles and mechanisms of such remarkably efficient, selective and specific transport contribute to a rapidly growing area of research on nanoporous membranes. Knowledge gained from fundamental studies of transport through nanochannels[1] is invaluable for the development of membranes for highly specialized and diverse applications such as separations for the isolation and purification of biomolecules[2] and other molecules of industrial and commercial interest (pharmaceutical molecules,[3] agrochemicals, food and perfume additives[4]), systems for delivery[5] and controlled release of drugs,[6] sensing of chemicals and biomarkers[7] and platforms for bionanoreactors[8] and catalysis.[9]

The transport properties of the nanoporous membranes that are described in this thesis have been studied for the purpose of evaluating their potential for separations. The use of membranes for separations offers several advantages over traditional separation methods such as chromatography, the most important of which are the ability to separate larger amounts of material and the continuous mode of operation (as opposed to batch processing). Furthermore, while chromatography can yield compounds with excellent purities, it does so at the cost of solvent, energy and labor.

The usefulness of membranes for separations stems from the ability to control the transport on the molecular scale using one or combinations of the following methods: (1) size selection of the permeating species, (2) charge selection of the species via electrostatic interactions, or (3) molecular recognition or enhancement of the transport of a preferred species as a result of favorable noncovalent interactions with the nanopore surface (Figure 1.1). While size-selectivity can be achieved with a straightforward manipulation of the pore size, the other two methods depend on interactions between the nanopore and diffusing species and thus usually require chemical modification of the nanopore surface with an appropriate functional group.

The wide variety of available membrane materials contributes to the tunability of the transport properties and operational parameters such as stability and longevity.[10] Membranes have been prepared from ion beam-etched silicon nitride,[11] track-etched polymers,[12] anodic-oxidized aluminum,[13] support- and/or matrix-embedded nanotubes,[14] zeolites[15] and self- or template-directed assembly of colloidal crystals.[16] However, challenges remain with the use of many of the above materials, particularly low transport rates due to low porosity and the lack of accurate control over the pore size. In addition, most of the above fabrication methods are disadvantageous in that they can be labor-intensive and technologically demanding. For these reasons, our strategy is to use self-assembled silica colloidal crystals characterized by high molecular flux through uniform nanopores whose surfaces are easily modified via well-known siloxane chemistry.[17] Free-standing silica colloidal membranes (nanofrits) that are investigated in this thesis conform to the requirements for practical membranes such as good mechanical strength, high surface area, low mass transfer resistance, high selectivity and versatile surface modification.[10,18]

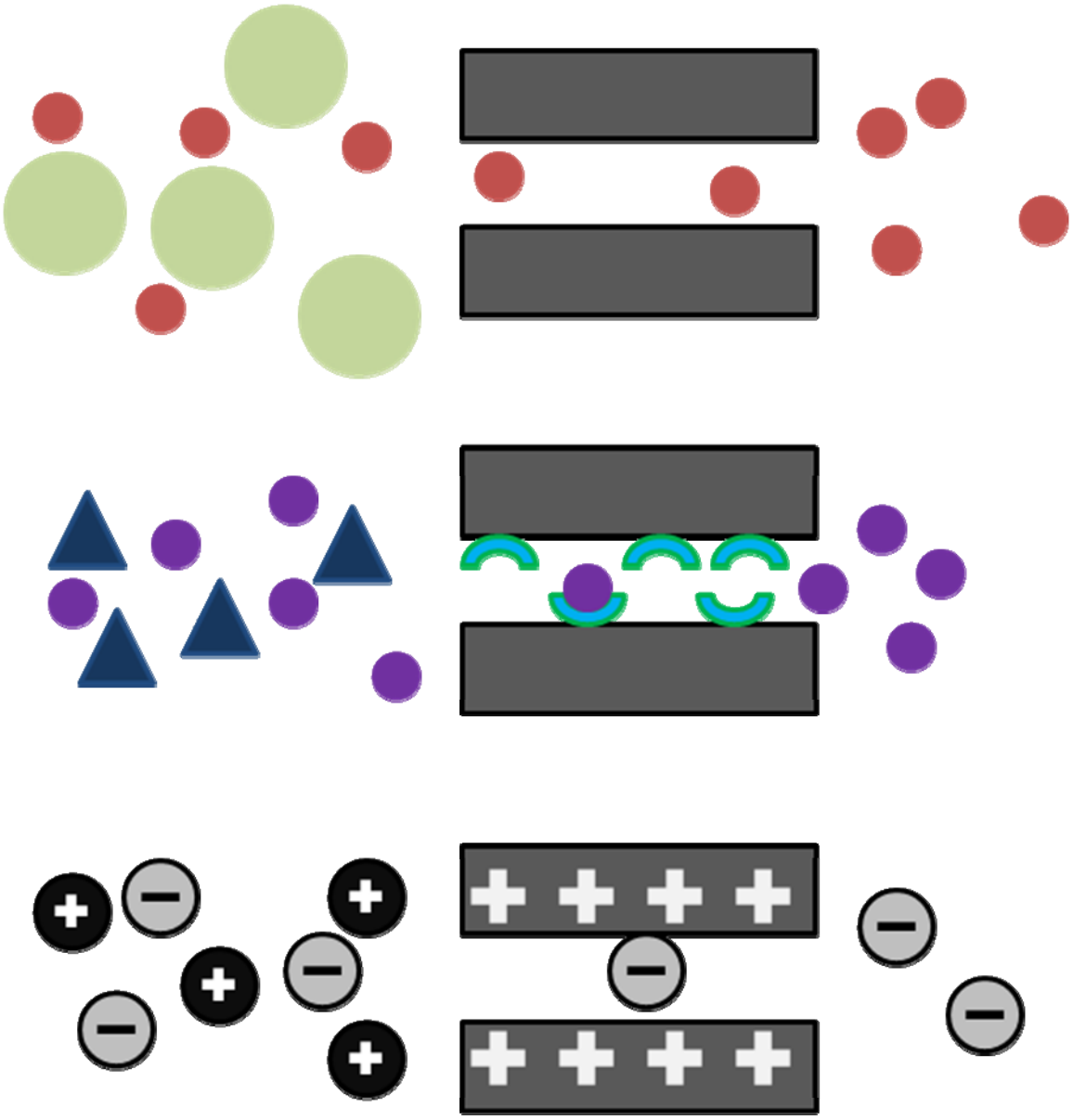

Figure 1.1. Three methods used to promote selectivity through porous membranes include: (Top) sterics, (Middle) molecular recognition and (Bottom) electrostatics.

Selectivity in Nanoporous Membranes

Size-selective separations techniques

Although popular separation techniques such as size-exclusion chromatography (SEC), size-selective precipitation, gel electrophoresis and (ultra)centrifugation have demonstrated excellent size-based resolutions, these methods are usually time-consuming or energy-intensive.[19] Filtration and porous membrane-based processes allow rapid separation based on a size-exclusion mechanism where species larger than the nanopore diameter cannot pass through the membrane.

Size-selective separations are relevant for macromolecules such as biomolecules. El-Safty and coworkers used anodic alumina membranes (AAM) rather than nanoporous polymers membranes that typically suffer from heterogeneity of pore diameters and structures. To vary the pore size, they modified the AAM pores with mesocylinder silica arrays[20] and silica nanotubes containing cubic mesoporous cages[21] (~5 nm pore entrance) and applied the resultant composites to the separation of mixtures of proteins (e.g., β-lactoglobulin, insulin, lysozyme). In a similar work, Zhang et al. fabricated mesoporous silica-coated carbon nanotubes (CNTs) using a surfactant-templated approach where the pore sizes of the silica coating were controlled by the concentration of CTAB.[22] A pore size of 2.72 nm was found to be effective and highly selective for the isolation of cytochrome *c* (12 kDa) from a mixture containing other larger proteins such as bovine serum albumin (69 kDa) and lysozyme (14 kDa). Roy and coworkers reported on protein separations using nanochannel titania membranes which had the advantage of declogging by degradation of adsorbed proteins upon UV illumination due to the photocatalytic activity of the membrane material.[23] Track-etched polycarbonate membranes with 50 nm pore size were shown to exhibit selectivities for the recovery of smaller ssDNA (10 vs. 80 bases).[24] Alternatively, well-defined nanoporous membranes with tunable nanopore sizes can also be prepared using click chemistry. Polysulfone membranes with surface azide groups were successfully grafted with propargyl poly(ethylene glycol)s (PEGs) via a Cu(I)-catalyzed azide-alkyne cycloaddition

(CuAAC).[25] The use of longer PEG chains led to narrower pore sizes for potential molecular sieving.

Larger pores are required for the separation of nanoparticles, whose importance lies in the need for chemical purity and size monodispersity in metal and semiconductor nanoparticles since these factors determine their optical, electronic and chemical properties.[26] Amphiphilic block copolymers have been reported to provide ordered membranes with pore sizes on the micron scale (3 μm) and were demonstrated to efficiently separate 2 μm from 5 μm polystyrene spheres.[27] Another example highlighted the filtration of 2 nm Au nanoparticles from a polydisperse mixture using self-assembled supramolecular membranes with a 5 nm-cutoff.[26]

Electrostatically controlled separations

Charge-selective separations result from either attractive or repulsive electrostatic interactions between the charged surfaces of a nanopore and the diffusing species. In the former case, electrostatic attraction could facilitate the transport of an oppositely charged species through the nanopore; in the latter, electrostatic repulsion could lead to hindered or blocked transport of a like charged species through the membrane. Such systems are typically pH- and ion-responsive as a result of the presence of ionizable groups on the nanopore surfaces.[28] Alumina and silica membranes possess inherently charged surfaces due to the weak acidity of aluminols ($4 < pK_a < 5$)[29] and silanols ($6 < pK_a < 8$) to give $Al\text{-}O^-$ and $Si\text{-}O^-$ upon immersion in water. Nanopore modifications with basic small molecules or weak cationic polyelectrolyte brushes give membranes that are protonated under acidic conditions with the effect of preferential transport of anions over cations (Figure 1.1). Upon deprotonation at higher pH, the nanopores become neutral and transport selectivity may be reversed depending on the availability of lone pairs of electrons on the surface-bound moieties for interaction with diffusing positively-charged species. Conversely, membrane modifications with acidic small molecules or weak anionic polyelectrolyte brushes create uncharged pores at low pH values. Dissociation of the acid

moieties under basic conditions switches the transport selectivity for cations over anions due to favorable electrostatic attractions.

Saxena et al. prepared both negatively charged (bearing sulfonic acid groups) and positively charged (bearing quaternized pyridinium groups) organic-inorganic hybrid membranes based on poly(vinyl alcohol)/silica systems for the isoelectric separation of proteins using pressures and electric gradients as coupled driving forces.[30] Isoelectric focusing was achieved by changing the mixture's pH. In an earlier study, Garem et al. applied cationic organic-inorganic nanofiltration membranes (polyethyleneimene-coated zirconium oxide on microporous carbon support) to the separation of amino acids, which were positively-, negatively-charged or zwitterionic at a given pH.[31] Charge-selective transport across polyelectrolyte multilayer membranes (e.g., poly(diallyl dimethylammonium chloride/poly(sodium styrenesulfonate)[32] of sub-nm pore sizes have also been reported for the separation of charged aromatic compounds (e.g., benzene and naphthalene sulfonates). Other examples of multilayer polyelectrolyte membranes obtained by alternating deposition of oppositely charged polyelectrolytes on porous supports have demonstrated enhanced anion transport selectivity ($Cl^-/SO_4^{2-} \sim 610$) as a result of Donnan rejection of the divalent anion.[33]

Molecular recognition-based separations

Molecular recognition for the separation of analytes takes advantage of differences in noncovalent interactions such as H-bonding, dipole-dipole, π - π stacking, CH - π and van der Waals forces between a membrane-bound selector and the diffusing species. One of the most widely studied applications is the enantioselective resolution of racemic mixtures. According to the Pirkle theory of chiral recognition,[34] stereoselective recognition requires a minimum of three simultaneous interactions between a bound chiral moiety and one of the enantiomers, where one of the interactions is stereochemically dependent (Figure 1.2). As selectand analytes approach the

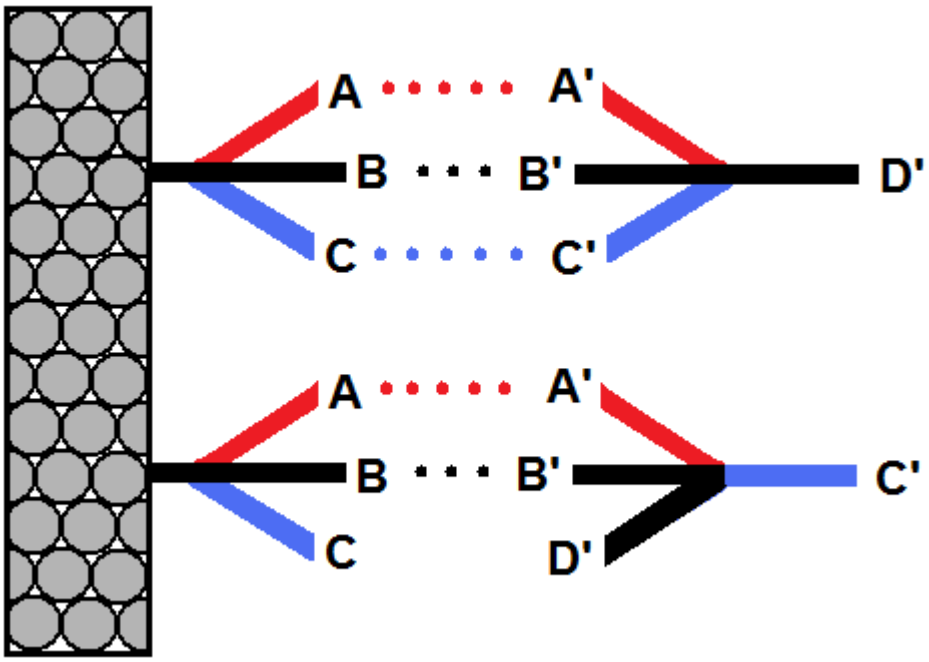

Figure 1.2. Schematic demonstrating the three-point requirements of chiral recognition.

chiral selector, one enantiomer is capable of three interactions while the other is only capable of two. Alternatively, separation in chiral membranes may be achieved by the preferential inclusion of one enantiomer over the other into a cavity within the polymer or porous material.[35] Cavity-guest interactions may arise from the installment of macromolecules such as crown ethers, cyclodextrans and calixarenes onto the nanopore surfaces. As a result of the stereochemistry, one enantiomer may be sterically hindered from accessing the cavity or may have different interaction energy within. A related concept of shape-dependent recognition is the technique of molecular imprinting. Such membranes are prepared in the presence of a chiral molecule that acts as a template. Removal of the imprint molecule (e.g., by calcination) leaves behind binding sites whose size, shape and preferential noncovalent interactions are complementary to the template.[36]

For example, self-standing membranes from novel polyureas were converted into molecular recognition materials with the incorporation of a chiral amino acid template molecule during the synthesis and preparation.[37]

As with chiral separations, molecularly imprinted polymers (MIP) have also been employed for protein specific recognition. Chen et al. reported the templating of bovine hemoglobin into polymer-coated Si nanowires for the rapid separation of the same protein.[38] These three methods create specific and efficient binding sites for the target enantiomer, allowing it to be distinguished from the other.[39]

Other than chiral recognition, biomimetic affinity binding represents another specific segment of the broader field of molecular recognition. Host-guest/substrate bioaffinity principles make for dedicated selectivities for proteins, peptides and glycans. Immobilization of "smart" ssDNA/RNA such as aptamers on graphene oxide nanosheets have been shown to specifically recognize and adsorb peptide toxins.[40] Aptamers are rapidly gaining popularity due to better or comparably high binding affinity, specificity and stability compared to antibodies and enzymes.

Diffusion through Nanoporous Membranes

The manner in which materials move across the membrane differs according to its type. Dense membranes are designed such that different molecules will dissolve into and move through it at different rates as measured by the solutes' permeability.[41] Permeability is the product of a molecule's solubility into and diffusivity (or diffusion coefficient) through the membrane material.[10] On the other hand, porous membranes are designed to contain pores that are ideally of similar size to the molecule of interest. The nanopores must be of uniform size and shape and must be continuous across the membrane to achieve a sieving effect.

For experiments in this thesis, the nanofrits separate two compartments, with one containing a solution of a probe molecule and the other a reservoir containing a pure solvent. Diffusion, defined as the spontaneous movement of molecules from areas of higher chemical

potential to areas of lower chemical potential, occurs as a result of differences in concentration across the membrane.[42] Flux *J*, defined as mass transfer per unit area of the membrane per unit of time, through the membrane can be calculated with Fick's Law (Equation 1.1), assuming steady-state diffusion:

$$J = - D \left(\frac{d\phi}{dx} \right) \tag{1.1}$$

where ϕ is the chemical potential as a function of position *x* and *D* is the diffusion coefficient of a species of interest. For nanoporous materials, and assuming ideal behavior of solutions, the above equation is transformed into:

$$J = \frac{D}{L} \times (\mathrm{C_a} - \mathrm{C_b}) \tag{1.2}$$

where C_a and C_b are the concentrations in the feed and reservoir compartments, respectively, separated by a membrane of thickness *L*. In the diffusion experiments performed in this thesis, experimental conditions are chosen such that $C_a >> C_b$, therefore :

$$J = \frac{\Delta \mathrm{C}}{L} \times D \tag{1.3}$$

where ΔC is the concentration gradient across the membrane, or simply the concentration of the solute in the feed solution. Equation 1.3 is the basic flux equation and is readily applied to cylindrical nanochannels after consideration of the void fraction ε corresponding to the ratio of

the volume taken up by the void space (i.e. nanochannel volume) to the total volume of the membrane.

Because the nanofrits employed in this thesis are prepared from silica colloidal crystals, the nanopores are not cylindrical and additional geometric characteristics have to be taken into account. As a result of the packing arrangement of silica nanospheres, the path that diffusing molecules must take through the membrane is extended by a factor called tortuosity τ that describes the nonlinearity of the pores (Figure 1.3). Both ε and τ are intrinsic properties of the colloidal crystal and have values of 0.26 and ca. 3, respectively.[43] Thus, molecular flux through a silica colloidal membrane can be expressed as Equation 1.4:

$$J_{\text{colloid}} = \frac{\Delta C}{L} \times \frac{\varepsilon}{\tau} \times D_{\text{sol}} \tag{1.4}$$

where D_{sol} is the diffusion coefficient of the solute in free solution. Equation 1.4 highlights one of the attractive features of using silica colloidal crystals, namely, the diffusivity remains high and is only an order of magnitude lower than in free solution ($\varepsilon/\tau \sim 0.1$) regardless of the nanopore size. Another advantage is that the tortuosity allows diffusing molecules to interact with nanopore surface functionalities more effectively, which can boost the transport selectivity compared to nanochannels of linear geometry.

To study the transport properties of our nanofrits, UV/Vis spectroscopy is utilized in this thesis. Flux is monitored as changes in the absorbance (A) measurements of the receiving solution with time, based on Beer's Law:

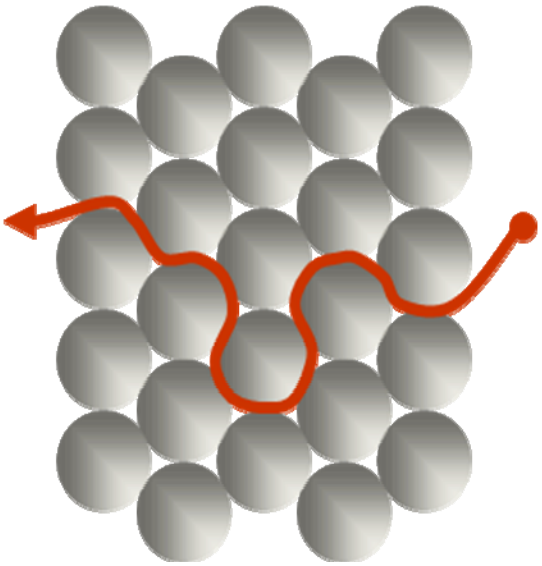

Figure 1.3. Schematic demonstrating how the geometric packing of silica spheres creates tortuous pathways (outlined in red) for diffusing molecules.

$$\mathrm{A} = a\mathrm{bC} \tag{1.5}$$

where a is the absorptivity of a species of concentration C interacting with incident light in a path length b. Thus, a plot of A vs. time t will have a slope (dA/dt) that is proportional to the diffusion rate R_D defined as the change in concentration with time (dC/dt). Equations 1.6 and 1.7 illustrate how flux through a membrane of surface area S, separating two solutions of equal volume V, is determined spectrophotometrically:

$$R_\mathrm{D} \propto \frac{\mathrm{dA}}{\mathrm{d}t} = \frac{\mathrm{V}}{a\mathrm{b}}\left(\frac{\mathrm{dC}}{\mathrm{d}t}\right) \tag{1.6}$$

$$R_\mathrm{D} = J_\mathrm{colloid} \times \mathrm{S} \tag{1.7}$$

Silica Colloidal Membrane Formation and Characteristics

Colloidal crystals are materials with a periodic arrangement of spherical particles of uniform size.[44] Silica colloidal crystals are formed when silica nanospheres undergo self-assembly[i] into a close-packed face-centered cubic lattice (*fcc*) (Figure 1.4). The silica colloidal crystals (Figure 1.5) contain highly ordered arrays of three-dimensional interconnected nanopores whose size is easily tuned by changing the diameter of the silica spheres used to create the assembly. The size of the nanopores is defined by the radius of the largest hard sphere that can fit within the void, i.e. the distance from the center of the pore to the nearest silica surface, the projection of which is ca. 8% of the silica nanosphere diameter. Thus, colloidal crystals from constituent spheres of diameters ranging from 50 to 1000 nm gives access to pores with 'radii' varying from about 4 to 80 nm.

Nanoparticles used to create membranes in this thesis are prepared using the so-called Stöber method. The method developed by Stöber et al.[45] dates back to 1968 and is now one of the most common and preferred procedures for the production of nonporous 'hard' silica particles because it can easily be carried out in ambient conditions and generally produces silica sphere batches of good monodispersity (10% or lower). In this synthesis, a precursor such as tetraethylorthosilicate (TEOS) is mixed with ammonia and water in ethanol to give the desired silica spheres (Figure 1.6). The mechanism of this process involves an initial base-catalyzed hydrolysis of TEOS followed by polycondensation of hydrolyzed silica species. The first step occurs more slowly and thus limits the over-all rate at which the particles grow. The size of the spheres can be controlled by adjusting the ratio of ammonia and water. Increased concentrations of the base in the reaction mixture produce larger silica spheres. The most widely accepted rationalization for this observation is that more basic conditions cause the forming silica particles

[i] Self-assembly is a spontaneous and reversible organization of a disordered system of pre-formed building blocks into structures that have a higher degree of orderliness than the isolated components.

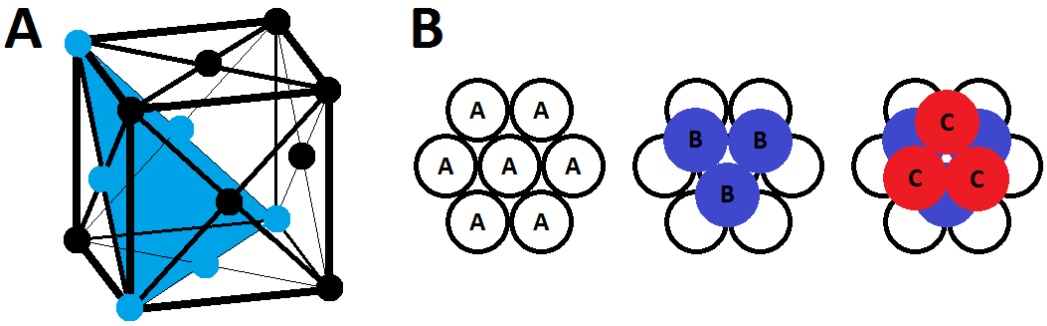

Figure 1.4. (A) The conventional unit cell is a cube with silica spheres occupying each of the vertices and middle of the faces. The blue-colored plane represents the (111) plane. (B) Each atom has 12 nearest neighbors, 6 coplanar and 3 each in the planes above and below in an ABC stacking manner.

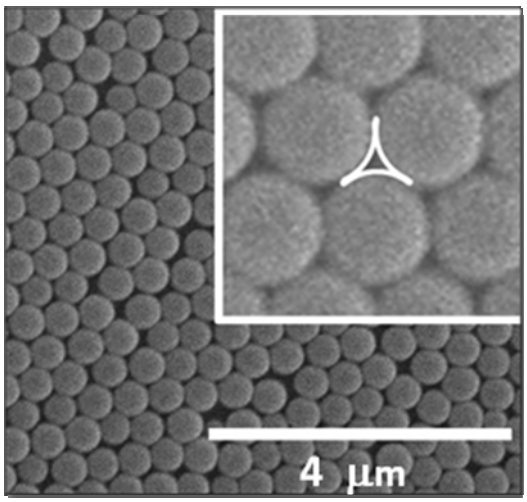

Figure 1.5. SEM image of a colloidal crystal prepared from silica spheres of 440 nm diameter (scale bar = 4000 nm). (Inset) The geometric projection of a pore observed from the (111) plane is outlined in white.

to be very unstable due to strongly negative surfaces. The instability makes the polycondensing species very reactive towards TEOS and other silica aggregates, enabling the particles to grow faster.[46] Particle growth continues until the magnitude of the overall surface charge is sufficiently decreased as to allow the spheres to precipitate out.

To promote crystallinity upon self-assembly and minimize dead space (as a result of interparticle repulsion), colloidal suspensions must be deionized exhaustively in polar solvents such as water.[47] The resultant silica colloidal crystals are thermodynamically stable formations (i.e., a product of static self-assembly) where the individual particles are held together by cohesive noncovalent interactions particularly van der Waals forces and H-bonding. It is noted that among the different techniques that can be used to assemble a crystal, convective assembly appears to be the most useful growth processes for the production of good quality crystals with a mainly *fcc* structure.[48]

The vertical deposition process, as employed in this thesis, is an example of convective assembly where a substrate (typically a glass slide) is immersed vertically into a colloidal solution of silica spheres in a quick-drying solvent such as ethanol (Figure 1.7). In addition to its high vapor pressure, the polarity of ethanol makes it a suitable medium to ensure good solvation of negatively charged silica particles resulting in a well-dispersed and stable colloidal suspension. The solvent is then allowed to evaporate in a vibration-free environment to produce colloidal crystals on the substrate. Modifications of this general method include the slow and controlled withdrawal of the immersed substrate from the colloidal solution[49] and the addition of a heat bath such that the colloidal solution is maintained at a temperature just below the boiling point of the solvent.

The evaporation-induced self-assembly of silica spheres into a colloidal crystal is driven by capillary forces in the solvent meniscus that drags more spheres from the colloidal solution into the growth front.[50] Once confined in the limited volume of the drying front, the silica spheres adopt the lowest energy conformation into a close-packed *fcc* lattice. The resultant

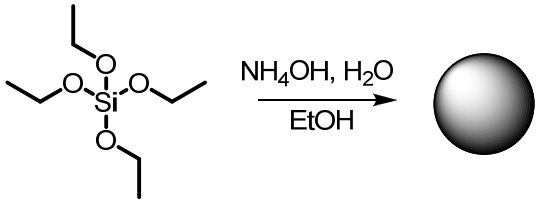

Figure 1.6. Synthetic scheme used to create monodisperse silica spheres.

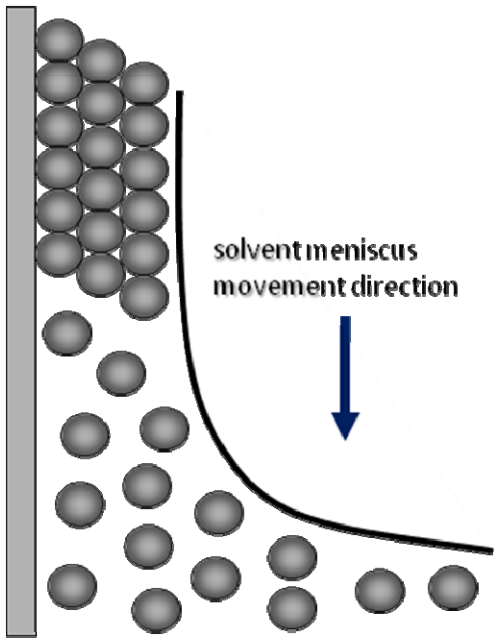

Figure 1.7. Schematic of the vertical deposition process used to self-assemble colloidal films. The spheres are drawn up the meniscus to the growth front by capillary action while the evaporating solvent lowers on the substrate along the drying front.

colloidal crystal can remain on the glass support even after drying due to adhesive van der Waals and H-bonding interactions between the silica spheres and the substrate. Vertical deposition is a simple, fast and reproducible way to create high quality colloidal crystals with large surface area and controlled thickness, and is thus the preferred method for the preparation of nanofrits in this thesis.

The thickness of the colloidal crystals is of importance for the study of transport properties; as can be seen in Equation 1.4, molecular flux through a membrane is inversely proportional to the membrane thickness. Several parameters in the vertical deposition method provide handles for the manipulation of the film thickness. First, the use of higher concentrations of colloidal solutions results in thicker films due to the fact that more particles are drawn up the meniscus at any given time during solvent evaporation. While overly thick membranes are undesirable due to decreased flux, it is noteworthy that sufficient thickness is necessary for the formation of practical, robust free-standing nanofrits. In this thesis, the use of 10 – 12 wt % colloidal solutions reproducibly yield nanofrits of approximately 0.2 – 1.0 mm thickness depending on the size of the constituent nanoparticles.

The second factor to consider is the size of the silica spheres that make up the colloidal crystals. For two colloidal solutions at the same concentration, the one consisting of smaller particles will produce a thicker film. For the same concentration, the number of smaller particles in colloidal solution is higher than that of larger spheres. Work in our group has demonstrated that 1.5 wt % solutions of silica spheres 440 ± 11 nm and 170 ± 14 nm produce 1.2 and 3.2 μm-thick colloidal films, respectively.[51] Furthermore, because larger particles can settle out of solution more quickly than smaller spheres, the former tend to produce thinner films.[52]

Third, evaporation rate also plays a role in the control of membrane thickness. A less volatile solvent usually gives thinner films because the slow removal rate provides the particles with time to settle out of solution, thereby reducing the number of spheres that will be drawn up by capillary forces onto the substrate. If alternative solvents of higher volatility are not available,

the application of elevated temperatures and/or vacuum are other means by which solvent removal may be accelerated.

Other techniques for colloidal assembly including gravitational methods such as sedimentation and centrifugation have also been used. In the former, self-assembly occurs at the bottom of the container when dispersed spheres settle out of the mixture. Crystals produced in this manner typically contain defects such as the presence of various domains that adversely affects reproducibility. Silica colloidal crystals have also been obtained by prolonged centrifugation. However, polarized transmission images revealed the presence of grains with varying crystallographic orientations. Stacking disorders were also apparent from striations within grains due to growth faults arising from the applied stress.[53] Other methods such dielectrophoretic ordering directs the assembly of colloidal particles into crystalline structures within seconds to minutes upon application of an electric field.[54] The kinetics of assembly and degree of orderliness has been shown to depend on particle size and charge, solution ionic strength and field strength and frequency. "Chemical" annealing has also been demonstrated for the rapid fabrication of large-scale colloidal crystals by immobilization within UV-cured polymers.[55]

Modification of Silica Surfaces

Small molecule surface modifiers

The transport properties of the nanopores in silica colloidal membranes can be controlled by covalent surface modification with an appropriate moiety. The hydroxyl groups present on the silica surface are sufficiently dense ($5/nm^2$) and can undergo facile reactions with a wide variety of functionalities. The easiest way to derivatize the silica surface is by treatment with siloxanes, wherein new Si-O-Si bonds are formed as a result of substitution of the hydroxyl groups with the siloxyl modifiers. The installment of amine groups using 3-aminopropyltriethoxysilane (3-APTES) (Figure 1.8) is another common surface modification method utilized in this thesis for

the consequent addition of other groups via amide bond formation with acyl chlorides, *N*-hydroxysuccinimide esters, sulfonyl chlorides and isothiocyanates (Figure 1.9). The amine group is also useful for metal-ligand bond formation with metal nanoparticles. Other modifications include the attachment of moieties that will serve as initiators for surface-initiated polymerization within the nanopores.

In the last few years, our group has demonstrated the chemical modification of nanoporous colloidal films with small molecules that impart transport selectivity on the basis of electrostatics (ionizable groups such as amines[56] and sulfonic acids[57]) and molecular recognition (chiral selector molecules[58]).

Polymer surface modifiers

Polymers are gaining popularity and importance as modifiers for the creation of "smart" surfaces with switchable properties in response to applied stimuli. The polymer structures are designed to obtain changes in the chain conformation as well as physical and chemical properties of the polymer upon variation of environmental conditions such as pH, temperature, ionic strength, solvent polarity, presence of small molecules or ions, and application of electromagnetic field.

There are two general methods for the covalent tethering of polymer chains onto a surface.[59] In the "grafting to" method, preformed polymer chains are end-functionalized with a reactive moiety that is activated for bond formation with groups present on the surface. As examples, *N*-hydroxysuccinimide and thionyl chloride are employed for the activation of carbonyl groups at polymer chain ends for nucleophilic attack with amine-modified surfaces. Silica surfaces can also undergo condensation reactions with polymer chains containing silane and hydroxyl groups while gold surfaces can be easily modified with monolayers of carboxyl and thiol groups. This approach generally leads to low grafting densities due to the increased steric hindrance that limits the diffusion of unreacted polymer chains onto the surface as the reaction

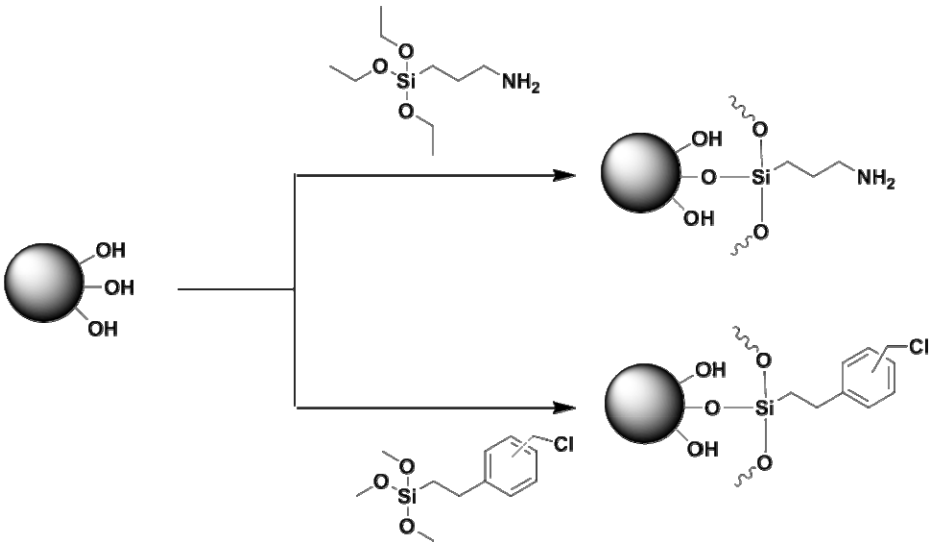

Figure 1.8. Modification of silica surfaces with siloxanes.

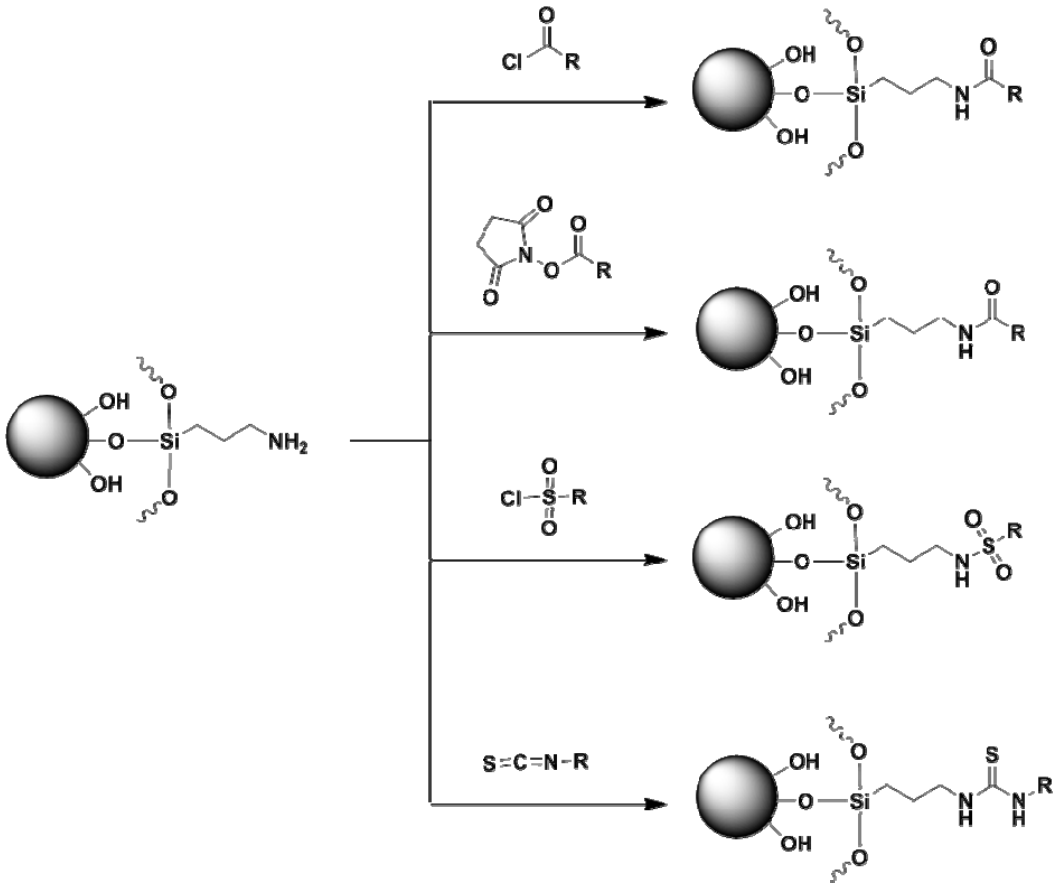

Figure 1.9. Reactions used for small molecule, macromolecule and polymer attachment.

progresses. One advantage of the "grafting to" method, though, is that it allows excellent control over the uniformity of tethered polymer chains with well-defined properties since they can be synthesized, purified and characterized separately. Recent work in our group has shown that nanopore surfaces can be "grafted to" with aptamers to manipulate the transport properties as a function of small molecule binding.[60]

Depending on the application, higher grafting densities may be desirable. If the goal is to control the nanopore size, the polymers have to be grafted with such density that the chains are forced to stretch away from the nanopore surface. Such polymer "brushes" are capable of maximized intermolecular interactions (both with the diffusing species and neighboring chains) in addition to steric hindrance to non-selective diffusion as a result of the more extended conformation of polymer chains. In this case, the "grafting from" is the technique of choice, where polymer brushes grow from a monolayer of surface-attached initiators.[61] In contrast to the "grafting to" method where bulky polymer chains migrate to the surface, this method minimizes steric hindrance to accessing initiator sites since smaller monomer units only need to approach the ends of the growing polymer brush layer. Thus, both high grafting densities and brush thicknesses can be obtained using various surface-initiated polymerizations such as ring-opening and controlled radical mechanisms among others as suited for a diverse range of monomers.[62] This thesis will describe the application of these two processes to produce polymer brushes attached to silica and gold surfaces inside colloidal membranes. Atom transfer radical polymerization (ATRP) is a particularly efficient method for the preparation of well-defined polymer brushes.[59] The mechanism (Figure 1.10) involves a transition metal catalyst such as Cu in the reversible activation/deactivation reaction between the growing polymer chain and the metal-ligand complex (e.g., Cu/bipyridine).[63] Silica surface-initiated polymerizations have been extensively investigated in our group wherein sulfonate-bearing brushes,[64] temperature-responsive polyacrylamides,[65] pH- and ion-responsive poly(aminomethacrylates)[66] and chiral

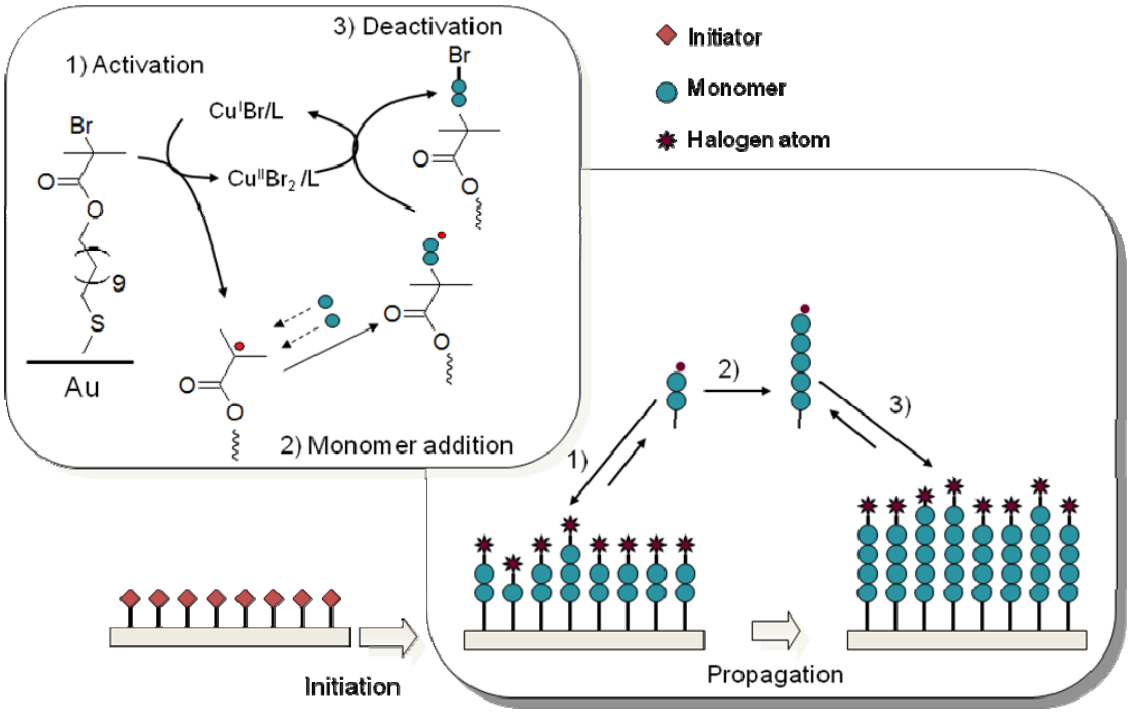

Figure 1.10. Mechanism of the ATRP of methyl methacrylate (as an example) from a Au surface modified with a thiol monolayer of the initiator.

moiety-bearing polymers have been grown via ATRP whereas polypeptides chains of *L*-alanine[67] have been grown via ring opening polymerization (ROP) to impart functionality and selectivity into the various systems studied. Polymerization inside the nanopores did not affect the integrity of the colloidal crystal.

Metallic surface modifiers

Silica-metal nanostructures have attracted significant attention because of their unique properties that make them well-suited for applications in catalysis, biosensing, optical devices and medicine.[68] In the area of catalysis, silica has been heavily investigated as support materials that

are impregnated with isolated metal atoms or monodisperse metal nanoparticles such as Mn,[69] Fe,[70] Ni[71] and Pt.[72] The applicability in biosensing and optical devices have likewise been evaluated particularly for silica-metal shell composites wherein the metal shells of Ag[73] and Au[74] exhibit enhanced Raman scattering.[75] Jankiewicz et al.[68] recently published a comprehensive review on silica-noble metal core-shell nanostructures that outlined main methods and strategies for their production followed by a summary of their characterization and applications.

Among the numerous methods for the preparation of silica-metal shell constructs, the seed-mediated growth strategy (where metal shells are formed on modified silica cores with pre-deposited metal nanoparticles) affords nanoshells of notably uniform thickness. This is important for controlling the surface properties of the resulting core-shell composites. This thesis will describe the synthesis of individually Au-coated silica nanoparticles following an electroless plating method as developed by Martin and co-workers.[76] The metal-modified spheres are then used for the preparation of Au-coated nanofrits for the purposes of increasing the mechanical robustness and surface densities of both small molecule and polymer modifiers. As previously mentioned, Au surfaces are readily modified via self-assembly of monolayers of thiols, amines and carboxylates through chemisorptions.[77]

Characterization of Colloidal Crystals

The use of silica colloidal crystals offers the ability to model the surface chemistry within the nanopores in the membranes by studying modifications carried out in colloidal solution, assuming close similarity in the behavior of both loose silica spheres and membrane samples. Silica spheres can be dispersed in a suitable solvent for common solution characterization techniques such as dynamic light scattering (DLS), infrared (IR), fluorescence, UV/Vis and nuclear magnetic resonance (NMR) spectroscopy. Transmission electron microscopy (TEM) and DLS are particularly useful for monitoring the size changes due to the subsequent surface modifications, particularly with polymers. Along with zeta-potential (ζ) measurements,

spectroscopic data give information on the chemical identities and structures of moieties on the surface. Thermogravimetric analysis (TGA) can also be conducted for the quantification of surface coverage with modifiers.

The characterization of modified silica colloidal crystals can be accomplished with common surface characterization techniques such as X-ray photoelectron spectroscopy (XPS), optical microscopy[78] which can be coupled with Fourier Fast Transform (FFT) image analysis,[79] scanning electron (SEM),[44] atomic force (AFM), confocal laser scanning,[80] X-ray microscopy[48] and reflection spectroscopy.[47,55] XPS can provide a wealth of information on the elemental composition (including the chemical or electronic state of each element) of the surface of a sample, while microscopy techniques reveal the physical features on the surface such as topography and arrangement of the nanoparticles.

Thesis Overview

This thesis will focus on the preparation and investigation of free-standing silica colloidal membranes whose nanopores are modified with a variety of small molecules and polymers for the size-, charge- and chiral-selective transport of neutral and charged species ranging from small dyes to biomolecules. Chapter 2 highlights the versatility of our nanoporous platform by demonstrating the self-assembly of thiol monolayers of both small molecule and polymer modifiers onto Au-coated silica colloidal crystals to create pH- and ion-responsive nanopores for the transport of neutral and charged dye molecules. Chapter 3 details the investigation of the potential of chirally-modified membranes for the enantiopermselective transport of chiral diffusion probes. Chapter 4 describes the preparation of unmodified nanofrits and diffusion studies of dendrimers of various generations as a function of probe size, nanopore size and surface charge density in a proof-of-concept experiment to assess the size-selectivity of the membranes. Chapter 5 applies the conclusions from the preceding chapter towards the study of PEG-modified silica colloidal frits for the size- and charge-selective transport of several protein

probes. A final chapter summarizes the work presented in this thesis and offers recommendations for future work.

References

(1) a) Liu, C.; Lv, Y.; Li, Z. *Journal of Chemical Physics* **2012**, *136*, 114506/1. b) Singh, K.P.; Kumar, M. *Lab on a Chip* **2012**, *12*, 1332. c) Su, J.; Olvera de la Cruz, M.; Guo, H. *Physical Review E: Statistical, Nonlinear and Soft Matter Physics* **2012**, *85*, 011504/1. d) Sheng, J.; Lui, K. *Soft Matter* **2012**, *8*, 367. e) Carr, R.; Comer, J.; Ginsberg, M.D.; Aksimentiev, A. *Lab on a Chip* **2011**, *11*, 3766.

(2) a) Achar, H.V.B.; Bhattacharya, E. *International Journal of Nanoscience and Nanotechnology* **2011**, *10*, 793. b) Daniel, S.; Chao, L.; *ACS Symposium Series* **2011**, *1062*, 99. c) El-Safty, S.; Shahat, A.; Nguyen, H. *Colloids and Surfaces, A: Physicochemical and Engineering Aspects* **2011**, *377*, 44.

(3) Zhu, X.-Y.; Zheng, Z.-J.; Xie, J.; Wang, P. *Journal of Separation Science* **2012**, *35*, 315.

(4) Xie, R.; Chu, L.-Y.; Deng, J.-G. *Chem. Soc. Rev.* **2008**, *37*, 1243.

(5) a) Hoare, T.; Timko, B.P.; Santamaria, J.; Goya, G.F.; Irusta, S.; Lau, S.; Stefanescu, C.F.; Lin, D.; Langer, R.; Kohane, D.S. *Nano Lett.* **2011**, *11*, 1395. b) Kulkarni, R.V.; Wagh, Y.J.; Setty, C.M.; Sa, B. *Polymer-Plastics Technology and Engineering* **2011**, *50*, 490. c) Mishra, R.K.; Datt, M.; Banthia, A.K. *AAPS PharmSciTech* **2008**, *9*, 395. d) Cardea, S.; Stessa, M.; Reverchon, E. *Industrial and Engineering Chemistry Research* **2010**, *49*, 2783.

(6) a) Wang, N.; Wu, C.; Cheng, Y.; Xu, T. *International Journal of Pharmaceutics* **2011**, *408*, 39. b) Wang, Y.; Shao, J.; Meng, Y.; Yang, Y. *Medicinal Chemistry Research* **2010**, *19*, 1055. c) Yang, S.Y.; Yang, J.-A.; Hahn, S.K.; Kim, J.K. *PMSE Preprints* **2009**, *101*, 994. d) Jao, W.-C.; Chen, H.-C.; Lin, C.-H.; Yang, M.-C. *Polymers for Advanced Technologies* **2009**, *20*, 680. e) Peppas, N.A.; Wood, K.M.; Thomas, J.B. in: Peinemann, K.-V.; Pereira Nunes, S. (Eds.) Membrane Technology, Wiley-VCH. Germany, 2008, 175-190.

(7) a) Albrecht, T. *Nature Nanotechnology* **2011**, *6*, 195. b) Girard-Egrot, A.P.; Maquette, C.A.; Blum, L.J. *International Journal of Nanotechnology* **2010**, *7*, 753. c) Mochizuki, K.; Iwatsu, H.; Sudoh, M.; Ishiguro, Y.; Suzuki, T. *Chemical Sensors* **2009**, *25*, 1. d) Koh, A.; Riccio, D.A.; Sun, B.; Carpenter, A.W.; Nichols, S.P.; Schoenfisch, M.H. *Biosensors and Bioelectronics* **2011**, *28*, 17. e) Li, J.; Yuan, R.; Chai, Y.; Che, X.; Li, W.; Zhong, X. *Microchimica Acta* **2011**, *172*, 163.

(8) a) Gaitzsch, J.; Appelhans, D.; Wang, L.; Battaglia, G.; Voit, B. *Angew. Chem. Int. Ed.* **2012**, doi 10.1002/anie.201108814. b) Ziaka, Z.D.; Navrozidal, A.; Paraschopoulou, L.; Vasileiadis, S.P. *Journal of Nanoscience and Nanotechnology* **2010**, *10*, 6276. c) Hu, W.; Chen, S.; Li, X.; Shi, S.; Shen, W.; Zhang, X.; Wang, H. *Materials Science and Engineering, C: Materials for Biological Applications* **2009**, *29*, 1216. d) Dedov, A.G.; Loktev, A.S.; Parkhomenko, K.V.; Tsodikov, M.V.; Teplyakov, V.V.; Uvarov, I.I.; Fedotov, A.S.; Moiseev, I.I. *Theoretical Foundations of Chemical Engineering* **2009**, *43*, 494.

(9) a) van den Bergh, J.; Nishiyama, N.; Kapteijn, F. in: Cybulski, A.; Moulijn, J.A.; Stankiewicz, A. (Eds.) Novel Concepts in Catalysis and Chemical Reactors 2010, 211-237. b) Gryaznov, V.M.; Ermilova, M.M.; Orekhova, N.V.; Tereschenko, G.F. *Chemical Industries* **2006**, *110*, 579. c) Lee, K.J.; Min, S.H.; Jang, J. *Small* **2010**, *6*, 2378. d) Shah, T.N.; Ritchie, S.M.C. *Applied Catalysis, A: General* **2005**, *296*, 12. e) Miachon, S.; Dalmon, J.-A. *Topics in Catalysis* **2004**, *29*, 59.

(10) Gin, D.L.; Noble, R.D. *Science* **2011**, *332*, 674.

(11) a) Lee, D.-S.; Song, H.-W.; Chung, K.-H.; Jung, M.Y.; Yoon, H.C. *Journal of Nanocience and Nanotechnology* **2011**, *11*, 4511. b) Wei, R.; Pedone, D.; Zuerner, A.; Doeblinger, M.; Rant, U. *Small* **2010**, *6*, 1406. c) Gadgil, V.J.; Tong, H.D.; Cesa, Y.; Benrink, M.L. *Surf. Coat. Technol.* **2009**, *203*, 2436.

(12) a) Wang, C.; Wang, L.; Zhu, X.; Wang, Y.; Xue, J. *Lab on a Chip* **2012**, *12*, 1710. b) Radji, S.; Alem, H.; Demoustier-Champagne, S.; Jonas, A.M.; Cuenot, S. *Macromol. Chem. Phys.* **2012**, *213*, 580. c) Kwon, K.; Park, C.-W.; Kim, D. *Sens. Actuators, A* **2012**, *175*, 108. d) Adrus, N.; Ulbricht, M. *J. Mater. Chem.* **2012**, *22*, 3088. e) Li, C.; Cao, B.; Wang, W.; Li, Q.; Zhao, J.; Zhang, L. *Polym. Adv. Technol.* **2010**, *21*, 698.

(13) a) Zhen, Y.; Wang, H.; Jia, X.; Jiang, H.; Liu, J. *Mater. Sci. Forum* **2011**, *694*, 585. b) Ferraz, N.; Hoess, A.; Thormann, A.; Heilmann, A.; Shen, J.; Tang, L.; Ott, M.K. *Journal of Nanoscience and Nanotechnology* **2011**, *11*, 6698. c) Wang, K.-K.; Kim, B.-J.; Ko, S.-H.; Choi, D.H.; Kim, Y.-R. *Journal of Nanomaterials* **2012**, 454507. d) Seshimo, M.; Ozawa, M.; Sone, M.; Sakurai, M.; Kameyama, H. *J. Chem. Eng. Jpn.* **2010**, *43*, 932. e) Kakiage, K.; Kyomen, T.; Unno, M.; Hanaya, M. *Appl. Organomet. Chem.* **2010**, *24*, 198.

(14) a) Sanip, S.M.; Ismail, A.F.; Goh, P.S.; Norrdin, M.N.A.; Soga, T.; Tanemura, M.; Yasuhiko, H. *Adv. Mater. Res.* **2012**, *364*, 272. b) Sadki, E.S.; Garaj, S.; Vlasserev, D.; Golovchenko, J.A.; Branton, D. *J. Vac. Sci. Technol., B* **2011**, *29*, 053001/1. c) Li, G.; Yang, D.; Zhu, Y.; Ma, J.; Nie, M.; Jiang, Z. *Chem. Eng. Sci.* **2011**, *66*, 4221. d) Madaeni, S.S.; Zinadini, S.; Vatanpour, V. *Sep. Purif. Technol.* **2011**, *80*, 155. e) Chan, Y.; Hill, J.M. *J. Membr. Sci.* **2011**, *372*, 57.

(15) a) Ji, M.; Liu, G.; Chen, C.; Wang, L.; Zhang, X. *Microporous Mesoporous Mater.* **2012**, *155*, 117. b) Drobek, M.; Motuzas, J.; van Loon, M.; Dirrix, R.W.J.; Terpstra, R.A.; Julbe, A. *J. Membr. Sci.* **2012**, *401-402*, 144. c) Zhou, R.; Zhang, Q.; Shao, J.; Wang, Z.; Chen, X.; Kita, H. *Desalination* **2012**, *291*, 41. d) Huang, A.; Wang, N.; Caro, J. *Chem. Commun.* **2012**, *48*, 3542. e) Shirakura, S.; Kojima, S.; Tanaka, K.; Kita, H. *Adv. Mater. Res.* **2012**, *383-390*, 1749.

(16) Zhang, H.; Dong, F.; Zhai, S.; Kang, X.; Fang, S. *Adv. Mater. Res.* **2012**, *399-401*, 677.

(17) a) Hanai, T.; *Adv. Chromatogr.* **2000**, *40*, 315. b) Kamp, U.; Kitaev, V.; von Freymann, G.; Ozin, G.A.; Mabury, S.A. *Adv. Mater.* **2005**, *17*, 438.

(18) Lu, G.Q.; Zhao, X.S., Eds.; *Nanoporous Materials: Science and Engineering*; Series of Chemical Engineering; Imperial College Press, 2004.

(19) Ye, G.; Norihisa, M. *J. Micromech. Microeng.* **2007**, *17*, 2308.

(20) El-Safty, S.; Shenashem, M.A. *Anal. Chim. Acta* **2011**, *694*, 151.

(21) El-Safty, S.; Shahat, A.; Nguyen, H. *Colloids Surf., A* **2011**, *377*, 44.

(22) Zhang, M.; Wu, Y.; Feng, X.; He, X.; Chen, L.; Zhang, Y. *J. Mater. Chem.* **2010**, *20*, 5835.

(23) Roy, P.; Dey, T.; Lee, K.; Kim, D.; Fabry, B.; Schmuki, P. *J. Am. Chem. Soc.* **2010**, *132*, 7893.

(24) Sheng, Y.; Bowser, M.T. *Analyst* **2012**, *137*, 1144.

(25) Meng, J.-Q.; Yuan, T.; Kurth, C.J.; Shi, Q.; Zhang, Y.F. *J. Membr. Sci.* **2012**, *401*, 109.

(26) Krieg, E.; Weissman, H.; Shirman, E.; Shimoni, E.; Rybtchinski, B. *Nature Nanotechnology* **2011**, *6*, 141.

(27) Wan, L.-S.; Li, J.-W.; Ke, B.-B.; Xu, Z.-K. *J. Am. Chem. Soc.* **2012**, *134*, 95.

(28) Saxena, A.; Shahi, V.K. *J. Membr. Sci.* **2007**, *299*, 211.

(29) Frini-Srasra, N.; Srasra, E. *Surface Engineering and Applied Electrochemistry* **2008**, *44*, 401.

(30) Saxena, A.; Kumar, M.; Tripathi, B.P.; Shahi, V.K. *Sep. Purif. Technol.* **2010**, *70*, 280.

(31) Garem, A.; Daufin, G.; Maubois, J.L.; Léonil, J. *Biotechnol. Bioeng.* **1997**, *54*, 291.

(32) Jin, W.; Toutianoush, A.; Tieke, B. *Appl. Surf. Sci.* **2005**, *246*, 444.

(33) Balachandra, A.M.; Dai, J.; Bruening, M.L. *Macromolecules* **2002**, *35*, 3171.

(34) Pirkle, W.H.; Pochapsky, T.C. *Chem. Rev.* **1989**, *89*, 347.

(35) Subramanian, G. (Ed.) Chiral Separation Techniques. A Practical Approach, Wiley-VC. New York, 2001.

(36) Okutucu, B.; Önal, S. *Talanta* **2011**, *87*, 74.

(37) Hatanaka, M.; Nishioka, Y.; Yoshikawa, M. *Macromol. Chem. Phys.* **2011**, *212*, 1351.

(38) Chen, T.; Shao, M.; Xu, H.; Zhuo, S.; Liu, S.; Lee, S.-T. *J. Mater. Chem.* **2012**, *22*, 3990.

(39) Garcia Del Blanco, S.; Donato, L.; Dridi, E. *Sep. Purif. Technol.* **2012**, *87*, 40.

(40) Hu, X.; Mu, L.; Wen, J.; Zhou, Q. *J. Hazard. Mater.* **2012**, *213-214*, 387.

(41) Liang, X.; Lu, X.; Yu, M.; Cavanagh, A.S.; Gin, D.L.; Weimer, A.W. *J. Membr. Sci.* **2010**, *349*, 1.

(42) Cussler, E.L. Diffusion: Mass Transfer in Fluid Systems, 2nd Ed., Cambridge University Press. New York, 1997.

(43) Newton, M.R.; Morey, K.A.; Zhang, Y.; Snow, R.J.; Diwekar, M.; Shi, J.; White, H.S. *Nano Lett.* **2004**, *4*, 875.

(44) Rodríguez, I.; Ramiro-Manzano, F.; Mesequer, F.; Bonet, E. *Eur. J. Phys.* **2011**, *32*, 505.

(45) Stöber, W.; Fink, A.; Bohn, E. *J. Colloid Interface Sci.* **1968**, *26*, 62.

(46) van Blaaderen, A.; van Geest, J.; Vrij, A.J. *Colloid Interface Sci.* **1992**, *154*, 481.

(47) Okamoto, J.; Tsuchida, A.; Okubo, T. *Colloid Polym. Sci.* **2011**, *289*, 1653.

(48) Hilhorst, J.; van Schooneveld, M.M.; Wang, J.; de Smit, E.; Tyliszczak, T.; Raabe, J.; Hitchcock, A.P.; Obst, M.; de Groot, F.M.F.; Petukhov, A.V. *Langmuir 2012*, doi 10.1021/la204580y.

(49) Gu, Z.Z.; Fujishima, A.; Sato, O. *Chem. Mater.* **2002**, *14*, 760.

(50) Yang, L.; Zhang, Y.; Luo, J.; Luo, Y.; Gao, K.; Li, D.; Meng, Q. *Phys. Rev. E* **2011**, *84*, 031605.

(51) Bohaty, A.K. "Studies of Diffusion of Molecules and Ions through Nanoporous Opal Films and Membranes" Ph.D. Dissertation, University of Utah, 2008.

(52) Jiang, P.; Bertone, J.F.; Hwang, K.S.; Colvin, V.L. *Chem. Mater.* **1999**, *11*, 2132.

(53) Suzuki, Y.; Endoh, J.; Mori, A.; Yabutani, T.; Tamura, K. "Gravitational Annealing of Colloidal Crystals" [Internet]. [Cited 2012 April 10]. Available from: http://arxiv.org/ftp/arxiv/papers/1201/1201.4361.pdf

(54) McMullan, J.M.; Wagner, N.J. *Langmuir* **2012**, *28*, 4123.

(55) Ishii, M.; Narita, T.; Hayata, Y.; Nishimura, A.; Tachi, K. *Macromol. Mater. Eng.* **2011**, *296*, 687.

(56) a) Newton, M.R.; Bohaty, A.K.; White, H.S.; Zharov, I. *J. Am. Chem. Soc.* **2005**, *127*, 7268. b) Newton, M.R.; Bohaty, A.K.; Zhang, Y.; White, H.S.; Zharov, I. *Langmuir* **2006**, *22*, 4429. c) Bohaty, A.K.; Smith, J.J.; Zharov, I. *Langmuir* **2009**, *25*, 3096. d) Bohaty, A.K.; Abelow, A.E.; Zharov, I. *J. Porous Mater.* **2011**, *18*, 297.

(57) a) Smith, J.J.; Zhaorv, I. *Langmuir* **2008**, *24*, 2650. b) Smith, J.J.; Zharov, I. *ACS Symposium Series* **2008**, *996*, 248.

(58) a) Cichelli, J.; Zharov, I. *J. Am. Chem. Soc.* **2006**, *128*, 8130. b) Cichelli, J.; Zharov, I. *J. Mater. Chem.* **2007**, *17*, 1870.

(59) Advincula, R.A.; Brittain, W.J.; Caster, K.C.; Ruhe, J. (Eds.) Polymer Brushes: Synthesis, Characterization and Applications, Wiley-VCH. Germany, 2004.

(60) a) Abelow, A.E.; Schepelina, O.; White, R.J.; Vallee-Belisle, A.; Plaxco, K.W.; Zharov, I. *Chem. Commun.* **2010**, *46*, 7984. b) Abelow, A.E.; White, R.J.; Plaxco, K.W.; Zharov, I. *Collect. Czech. Chem. Commun.* **2011**, *76*, 683.

(61) a) Ayres, N. *Polym. Rev.* **2011**, *51*, 138. b) Coessens, V.M.C.; Matyjaszewski, K. *J. Chem. Education* **2010**, *87*, 916. c) Yuan, J.; Zhou, M.; Yin, Y. in: Dixon, C.J.; Curtines, O.W. (Eds.) Nanotechnology, Nova Science Publishers, Inc. New York, 2010, pp. 309-330.

(62) Suresh, K.I. *Renewable Polymers* **2012**, 221.

(63) Dong, R.; Lindau, M.;Ober, C.K. *Langmuir* **2009**, *25*, 4774.

(64) a) Smith, J.J.; Zharov, I. *Chem. Mater.* **2009**, *21*, 2013. b) Smith, J.J.; Zharov, I. *PMSE Preprints* **2009**, *100*, 176.

(65) a) Schepelina, O.; Zharov, I. *Langmuir* **2007**, *23*, 12704. b) Schepelina, O.; Zharov, I. *Polymer Preprints* **2007**, *48*, 455. c) Schepelina, O.; Zharov, I. *Langmuir* **2006**, *22*, 10523.

(66) a) Schepelina, O.; Zharov, I. *Langmuir* **2008**, *24*, 14188. b) Schepelina, O.; Poth, N.; Zharov, I. *Adv. Funct. Mater.* **2010**, *20*, 1962.

(67) Abelow, A.E.; Zharov, I. *Soft Matter* **2009**, *5*, 457.

(68) Jankiewicz, B.J.; Jamiola, D.; Choma, J.; Jaroniec, M. *Adv. Colloid Interface Sci.* **2012**, *170*, 48.

(69) Schoenfeldt, N.J.; Ni, Z.; Korinda, A.W.; Meyer, R.J.; Notestein, J.M. *J. Am. Chem. Soc.* **2011**, *133*, 18684.

(70) Prieto-Centurion, D.; Notestein, J.M. *J. Catal.* **2011**, *279*, 103.

(71) Lv, X.; Chen, J.-F.; Tan, Y.; Zhang, Y. *Catal. Commun.* **2012**, *20*, 6.

(72) Peled, A.; Naddaka, M.; Lellouche, J.-P. *J. Mater. Chem.* **2012**, *22*, 7580.

(73) a) Lien, W.-F.; Huang, P.-C.; Tseng, S.-C.; Cheng, C.-H.; Lai, S.-M.; Liaw, W.-C. *Appl. Surf. Sci.* **2012**, *258*, 2246. b) Wang, W.; Jiang, Y.; Liao, Y.; Tian, M.; Zou, H.; Zhang, L. *J. Colloid Interface Sci.* **2011**, *358*, 567.

(74) Liang, Z.; Liu, Y.; Ng, S.S.; Li, X.; Lai, L.; Luo, S.; Liu, S. *J. Nanopart. Res.* **2011**, *13*, 3301.

(75) a) Kim, K.; Lee, H.B.; Choi, J.-Y.; Shin, K.S. *ACS Appl. Mater. Interfaces* **2011**, *3*, 324. b) Liu, T.; Li, D.; Yang, D.; Jiang, M. *Colloids Surf., A* **2011**, *387*, 17.

(76) a) Kohli, P.; Wharton, J.E.; Braide, O.; Martin, C.R. *Journal of Nanoscience and Nanotechnology* **2004**, *4*, 605. b) Yamada, K.; Gasparac, R.; Martin, C.R. *J. Electrochem. Soc.* **2004**, *151*, E14. c) Yu, S.; Lee, S.B.; Kang, M.; Martin, C.R. *Nano Lett.* **2001**, *495*.

d) Kang, M.-S.; Martin, C.R. *Langmuir* **2001**, *17*, 2753. e) Lee, S.B.; Martin, C.R. *Anal. Chem.* **2001**, *73*, 768.

(77) a) Saha, S.; Bruening, M.L.; Baker, G.L. *ACS Appl. Mater. Interfaces* **2011**, *3*, 3042. b) Dai, X.; Zhou, F.; Khan, N.; Huck, W.T.S.; Kaminski, C.F. *Langmuir* **2008**, *24*, 13182.

(78) Yang, L.; Wang, J.; Zhang, Y.; Luo, Y.; Li, D.; Meng, Q. *Langmuir* **2012**, doi. 10.1021/la205111v

(79) Mishchenko, L.; Hatton, B.; Kolle, M.; Aizenberg, J. *Small* **2012**, doi. 10/1002/smll.201102691

(80) Yoshikawa, K.; Okuzono, T.; Koga, T.; Taniji, T.; Yamanaka, J. *Langmuir* **2011**, *27*, 13420.

CHAPTER 2

pH- AND ION-RESPONSIVE TRANSPORT THROUGH GOLD-COATED FREE-STANDING COLLOIDAL MEMBRANES

Introduction

The isolation and purification of molecules is crucial for purposes of characterization and practical use (e.g., as pharmaceutical products). Column chromatography remains one of the most popular means of separating molecules on the bases of size, shape, polarity, affinity to the solid or mobile phase, etc.[1] However, the resolution of such columns is highly dependent on the manner in which the column is prepared and used. Potential problems associated with chromatography can be circumvented with the use of membranes.

Currently, most separations achieved via dialysis (movement of molecules by diffusion due to a concentration gradient through a semi-permeable membrane) employ commercially available organic membranes composed of regenerated cellulose. Chitin-chitosan[2] membranes have also been reported for the separations of amino acids and polypeptides.[3] However, disadvantages of using organic membranes include their limited compatibility with a wide range of solvents, irreversible sample binding to the membrane material, and their nonreusability. Alternatives to organic frameworks include inorganic materials such as ceramics, glass, carbon and metal. Anodic oxidation of aluminum[4] and ion beam etching of silicon nitride[5] lead to cylindrical pores within the membranes. The efficiency of separations can be improved by using membranes that contain convoluted pores instead of the cylindrical pores.[6] One example of such

pores are those in zeolites, which are closed loops built from tetrahedrally coordinated Si (or Al) and O atoms.[7] The bonding between the units and oxygen coordination to cations within the structure introduce ring strain and, as a result, channels within many zeolites are not cylindrical. Silica colloidal crystals provide another system with interconnected three-dimensional nanopores.[8] Silica colloidal crystals form via self-assembly[9] of silica nanospheres into a close-packed face-centered (*fcc*) lattice.[10] This results in three-dimensional interconnected tetrahedral and octahedral voids between neighboring spheres that provide tortuous pathways for molecules diffusing through the crystal.

Transport selectivity through nanoporous membranes based on charge, polarity, shape and chirality can be achieved by modifying the surface of the pores with organic functionalities such as polymers.[11] Functional membranes have been prepared both with noncovalent (e.g. layer-by-layer adsorption of polyelectrolyte multilayers) and covalent (polymerization from a surface-bound initiator) surface modification. Incorporation of responsive moieties in a membrane introduces chemical selectivity based on electrostatic and other noncovalent interactions with a particular diffusing species.

In this work, silica spheres are coated with a gold shell to impart increased mechanical strength to the resulting colloidal membranes, provide a method for nanopore size manipulation, introduce new types of nanopore surface modification, and increase the surface density of organic moieties compared to a silica surface (a maximum of 10 and 5 modifier groups/nm^2 for Au and silica surfaces, respectively). Reports on transport in gold-coated nanopores describe the use of track-etched polycarbonate as template. A surface modification with a self-assembled monolayer (SAM) of *L*-cysteine[12] or 11-mercaptoundecanoic acid[13,14] can result in pH-switchable transport selectivity for ions and proteins.[15] Comparison of the performance of membranes modified with perfluorodecanethiol or its alkyl analogue 1-decanethiol,[16] and with hexadecanethiol or 1-mercaptoethanol,[17] showed transport selectivity for hydrophobic molecules. In addition to the above small molecule modifiers, polymers such as polypeptides[18] and polyelectrolytes[19] have

also been grafted onto the Au-coated nanopores.[20] Lokuge et al. reported thermally-switchable and size-selective transport of dye-labeled dextrans through membranes with surface-grafted poly(*N*-isopropylacrylamide) (PNIPAAm) chains[21] while Yu and coworkers achieved size-based protein separations using poly(ethylene glycol) (PEG) to minimize protein adsorption.[22]

Recently, we showed that pH and ion-responsive transport through colloidal nanopores could be achieved by silica surface modification with weak cationic polyelectrolyte brushes.[23] The current work describes the preparation and characterization of Au-coated silica colloidal membranes whose surface has been modified either with *L*-cysteine, a 16-carbon *n*-alkylthiol, or the weak anionic polyelectrolyte poly(methacrylic acid) (PMAA). PMAA is a well-studied environmentally responsive polymer that is known to undergo various degrees of swelling depending on pH.[24] PMAA brushes change their thicknesses as a result of stronger electrostatic repulsion between the charged moieties with increasing number of dissociated –COOH groups as the pH is raised.[25] In addition, earlier studies on the swelling behavior of PMAA brushes in aqueous solution in the presence of various salts have established that polycarboxylates exhibit specific responses when exposed to different cations such as alkali, alkaline earth and transition metals.[26,27] Using absorbance measurements to monitor diffusion through our surface-modified Au-coated nanoporous membranes, we demonstrate in this chapter the ability to control the molecular transport through the nanopores by changing the environmental pH and ionic strength.

Experimental Section

Materials

Chemicals. Ammonium hydroxide (28-30% as NH_3, EMD Chemicals, Inc.), tetrabutylammonium hydroxide (40% wt solution in water, Sigma-Aldrich), triethylamine (J.T. Baker), hydroxylamine hydrochloride (Sigma-Aldrich), sodium hydroxide (Mallinckrodt Chemicals), sodium carbonate anhydrous (Mallinckrodt Chemicals), sodium bicarbonate (Mallinckrodt Chemicals), sodium nitrate (J.T. Baker), ammonium chloride (Mallinckrodt

Chemicals), magnesium sulfate anhydrous (Mallinckrodt Chemicals), (ethylenedinitrilo)tetraacetic acid disodium salt dihydrate (Mallinckrodt Chemicals), bromine solution (EMD Chemicals, Inc.), dichloromethane (Mallinckrodt Chemicals), nitric acid (68-70%, ACS-grade, EMD Chemicals, Inc.), trifluoroacetic acid (Acrōs), tetraethylorthosilicate (99.999+%, Alfa Aesar), ethanol (200 proof, ACS-grade, Pharmaco-Aaper), tetrachloroaurate(III) trihydrate (Acrōs Organics), sodium citrate dihydrate (Alfa Aesar), sodium borohydride (Alfa Aesar), sodium methacrylate (Alfa Aesar), copper(I) bromide (Aldrich), copper(II) bromide (Aldrich), 2,2'-dipyridyl (Aldrich), 11-mercapto-1-undecanol (Aldrich), 2-bromoisobutyryl bromide (Aldrich), L-cysteine (Aldrich), dihexadecyl disulfide (Aldrich), ferrocenecarboxaldehyde (Aldrich) and Rhodamine B (Sigma) were all used as received. Millipore water (18 MΩ•cm) used in all experiments was obtained from a Barnstead "E-pure" water purification system. Acetonitrile (HPLC grade, VWR Scientific) was freshly distilled from calcium hydride. Column chormatography was performed using silica gel (40-63μm) with 60Å pore diameter (Silicycle Chemical Division). TLC was performed using Silica gel 60 F_{254} on aluminium sheets (EMD Chemicals, Inc.).

Instrumentation. Scanning electron microscopy (SEM) images were obtained using either a Hitachi S3000-N or an FEI NanoNova instrument. Transmission electron microscopy (TEM) images were obtained using an FEI Philips Tecnai T-12 instrument. UV/Vis measurements were collected using an Ocean Optics USB2000 or USB4000 instrument. A Branson 1510 sonicator was used for all sonications. A Clay Adams Compact II Centrifuge (3200 rpm, Becton Dickinson) was used for all centrifugations. A Fisher Scientific Isotemp Programmable Muffle Furnace (Model 650) was used for all sintering purposes. All zeta-potential measurements were carried out in water using a NICOMP 380 ZLS Zeta Potential/Particle Sizer (PSS•NICOMP Particle Sizing Systems). Thermogravimetric analyses were performed using a TA Instruments TGA 2950 Thermogravimetric Analyzer.

Methods

Preparation of 350 nm silica spheres. All silica spheres were prepared according to modifications of previously reported procedures.[28,29] All glassware were cleaned with Millipore water prior to use. A batch of silica spheres was made by mixing 500.0 mL of an ethanolic solution containing TEOS (51.4 mL, 0.20 mol) with 500.0 mL of an ethanolic solution containing NH_4OH (70.0 mL, 1.1 mol) and water (257 g, 14.3 mol). These two solutions were poured simultaneously in a 2 L Erlenmeyer flask and vigorously stirred. The resulting mixture had final concentrations of 0.2 M TEOS, 1.1 M NH_3 and 17.0 M H_2O. The onset of turbidity after a short while indicated the start of silica sphere formation. After 24 h, the mixture was then poured into 15 mL centrifuge tubes (Corning) and centrifuged for 10 min. The supernatant was discarded, leaving the spheres as pellets at the bottom of the centrifuge tubes. Purification of the spheres was achieved by a repetitive cycle of suspending the spheres via sonication for 10 min followed by centrifugation for 10 min in a gradient series of 10 mL supernatant: 100% water, 25% ethanol, 50% ethanol, 75% ethanol (twice) and finally 100% ethanol. After the final rinsing, the supernatant was decanted and the silica spheres air-dried overnight. The dried spheres were then pre-shrunk by transferring to a Petri dish (breaking any large aggregates with a spatula) and placing in a furnace programmed to heat the spheres for 4 h at 600°C[30-32] (desired temperature achieved at a heating rate of 20°C/min). SEM images were obtained of the spheres and their size was determined from 100 individually measured spheres to be 350 ± 20 nm in diameter.

Preparation of 3 nm Au nanoparticles. Gold nanoparticles of nominal size 3nm were prepared according to literature.[33] Briefly, 90.0 mL of a 0.27 mM $HAuCl_4 \bullet 3H_2O$ aqueous solution was mixed with 2.0 mL 1% sodium citrate aqueous solution with stirring. After 1 min, 1.0 mL freshly prepared 0.075% $NaBH_4$ in 1% sodium citrate solution was added and the mixture stirred for another 5 min. The reaction temperature was maintained constantly at 4 °C. This stock solution of Au nanoparticles was then stored in the refrigerator. TEM images indicated that

the nanoparticles were prone to aggregation, leading to particles with sizes ranging from about 8 to 40 nm in diameter.

Preparation of Au-coated silica spheres. The preshrunk particles were aminated prior to Au-coating. To 13.3 g silica spheres dispersed in 200 mL dry acetonitrile, 0.40 mL of 3-aminopropyltiethoxysilane was added and the mixture was vigorously stirred and kept under N_2 (g) overnight. The modified particles were isolated by repeated centrifugation and resuspension in acetonitrile, tetrahydrofuran, xylene, twice in water and twice in acetonitrile, followed by air-drying. The aminated spheres were then immersed in a six-fold diluted aqueous solution of the Au nanoparticles for 10 h with stirring. The wine red color of the solution disappears as the Au nanoparticles chemisorbed onto the surface of the spheres. The faintly pink spheres were then collected via centrifugation and washed via sonication in deionized water at least three times prior to air-drying.

The spheres were ground up and poured into a 250-mL Erlenmeyer flask, to which then 200 mL of a Au-plating solution (0.1% w/w $HAuCl_4$ in 0.40 mM $NH_2OH{\bullet}HCl$) was added with vigorous stirring for 30 min. The colloidal solution turned into a deep purple color as Au shells were chemically deposited onto the surface of the silica spheres. The Au-coated spheres were collected in 15-mL Corning tubes, centrifuged and rinsed repetitively with deionized water at least five times. The modified spheres were dried under a stream of N_2 (g) to give a violet-colored powder. TEM images confirmed the formation of a Au coat of uniform thickness and relatively smooth surface around the silica spheres. The thickness of the Au shell was estimated to be ~20 nm based on comparison of SEM images of aminated and Au-coated particles.

Surface-modification with *L*-cysteine. *L*-cysteine chemisorption onto the Au surface was achieved according to literature.[34] Briefly, sintered membranes of Au-coated silica spheres were immersed into a 2 mM solution of *L*-cysteine in 80% ethanol for 24 h with stirring in an inert atmosphere. The membranes were then rinsed with ethanol and dried in air.

Surface modification with *n*-dihexadecyl disulfide. A SAM of a 16-carbon *n*-alkylthiol was chemisorbed onto the Au-coated nanopores by immersing sintered membranes in a 2 mM solution of dihexadecyl disulfide in 1-octanol for 24 h with stirring in an inert atmosphere. The membranes were then rinsed with copious amounts of ethanol and air-dried.

Synthesis of ATRP initiator. The initiator and its precursor were synthesized according to a previous publication.[35] Briefly, the precursor was prepared by dissolving 1.0225 g of 11-mercapto-1-undecanol in 37.5 mL dichloromethane and 5 mL 10% $KHCO_3$ solution in a round-bottom flask with stirring, to which 128 μL of bromine solution was added dropwise. After the brown color of bromine has disappeared, the aqueous phase was extracted with 50 mL dichloromethane. The organic phases were combined and dried with anhydrous $MgSO_4$. Solvent removal yielded a white solid (average 56.8% yield) whose ^{1}H NMR spectrum corresponded to literature. To 1.25 g of the disulfide precursor dissolved in 75 mL dichloromethane, 2.09 mL triethylamine was added and the mixture was maintained at 0 °C under an inert atmosphere. The resulting solution was stirred for 1 h after 0.94 mL of 2-bromoisobutyryl bromide was added dropwise. The temperature was then brought to 25 °C and stirring continued for another 2 h, after which the solution was extracted with 2 N Na_2CO_3 saturated with NH_4Cl. The organic solvent was evaporated to afford a pale yellow viscous liquid. The crude product was purified via flash chromatography using a mobile phase of 1:1 dichloromethane:acetonitrile. The final initiator product was a viscous, clear yellow liquid (average 65.9% yield) whose ^{1}H NMR spectrum was in good agreement with that of previous reports.

Surface-modification with polymer brushes. Poly(methacrylic acid) (PMAA) brushes were grown onto the surface of the Au via atom-transfer radical polymerization.[36] The Au-coated substrates (either loose spheres or sintered membranes) were submerged in 1 mM initiator solution in absolute ethanol overnight in a nitrogen atmosphere, after which the substrates were rinsed with ethanol and blown dry. In a N_2(g)-filled flask, 2.12 g (20 mmol) sodium methacrylate, 28.7 mg (0.20 mmol) CuBr, 9.0 mg (0.04 mmol) $CuBr_2$ and 78.4 mg (0.48 mmol)

2,2'-dipyridyl reagent were mixed together with 4 mL deionized water (pH 9, bubbled with N_2(g) for at least 30 min beforehand) with stirring at room temperature for ~5 min. The initiator-modified Au-coated substrates were then added into the flask and polymerization carried out at ambient temperature. The polymerization time was varied from 5 to 25 min for the loose spheres, and up to 45 min for sintered membranes. The substrates were then washed with deionized water, sonicated in 0.1 M EDTA solution, rinsed with water and ethanol and N_2(g)-dried.

Preparation of free-standing nanofrits. The nanofrits were prepared by vertical deposition onto a glass substrate from 12-15 wt% colloidal solutions of Au-coated silica spheres in ethanol. The resulting membranes were then gently lifted from the glass slides and sintered in a furnace for 10 h at 1000 °C (desired temperature achieved at a heating rate of 5 °C/min). The sintered colloidal membranes were now noticeably much more robust and durable, making handling easier. SEM images of the nanofrits were taken to give an average diameter of 338 ± 10 nm as measured from 100 individual spheres in each colloidal membrane. The thickness of each colloidal membrane was measured with a Vernier caliper at six points throughout the piece. The membranes were then subject to surface modification as outlined above. To make nanofrits, the pieces were then sandwiched between two PTFE washers (5.0 mm inner diameter, 14.0 mm outer diameter and 1.0 mm thickness, Small Parts, Inc.) with Loctite Hysol 0151 Epoxy. Nanofrits constructed as such were allowed to cure for at least 24 h prior to use for diffusion experiments.

Diffusion measurements through nanofrits. Diffusion experiments through the colloidal membranes were performed by placing a nanofrit between two connected 1-cm quartz cuvettes. The feed cell contained 4.00 mL of an aqueous dye solution while the reservoir cell contained 4.00 mL of the blank solution. The nanofrit was placed between two Kalrez o-rings to guard against leaking, and the whole assembly was then secured with a clamp. Each cell was covered with Parafilm to prevent eventual evaporation, and the contents of both cells continually stirred. The reservoir cell was placed between two fiber optic cables and was initially blanked. The flux was monitored by recording the absorbance in the reservoir cell for at least 18 h. In

diffusion experiments with a mixture of two dyes in the feed cell, the absorbances at both λ_{max} values for ferrocenecarboxaldehyde and Rhodamine B (488 nm and 546 nm, respectively) were simultaneously recorded. Data points were acquired every 150 s with an initial delay of 150 s. Prior to using a nanofrit for a new trial, the pieces were immersed in deionized water for at least 2 days and the water replaced occasionally to ensure removal of any previous probe molecule from within the colloidal films.

Results and Discussion

Preparation of free-standing Au-coated membranes

To prepare Au-coated silica colloidal crystals, amine groups were first introduced onto the surface of 320 nm silica spheres, resulting in thin polymeric layers of silamines. These amine groups acted as ligands for the chemisorption of gold nanoparticles (2 – 10 nm diameter) (Figure 2.1), which in turn served as nuclei that grew larger and eventually coalesced upon immersion of the nanoparticles in a gold-plating solution to form a coat of uniform thickness (~20 nm) around each silica sphere. Each of the modifications described above was followed by the changes in color of the colloidal solutions (Figure 2.2), and by using DLS, SEM and TEM (Table 2.1, Figure 2.3). If desired, we could vary the thickness of the gold layer by changing the reaction conditions such as plating time and the ratio of the amounts of the gold source ($HAuCl_4$) and the reducing agent (NH_2OH).

Nanoporous membranes were prepared next via the vertical deposition method from colloidal solutions of Au-coated silica spheres. Coating the silica spheres with a gold shell did not appear to affect the self-assembly of the spheres into an *fcc* arrangement (Figure 2.4). Free-standing membranes from gold-coated silica spheres were then produced by sintering at 1000 °C. In addition to providing mechanical integrity and strength to the membrane, sintering also ensured uniform coverage with surface modifiers in subsequent functionalizations. Indeed, a uniform Au layer on the membrane surface should be crucial for obtaining uniform films of

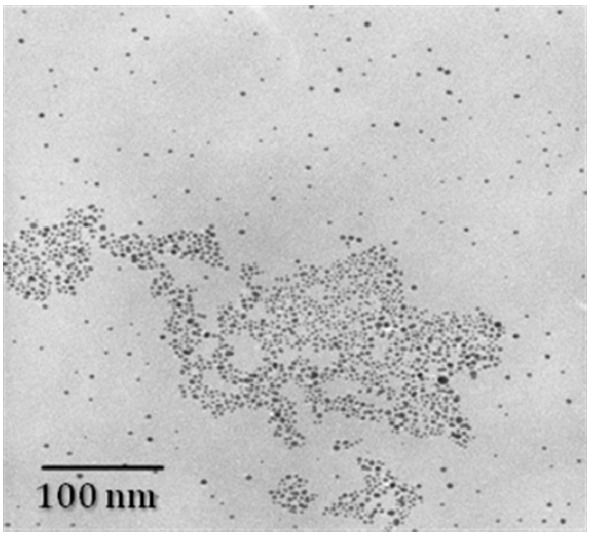

Figure 2.1. TEM image of Au nanoparticles (scale bar = 100 nm).

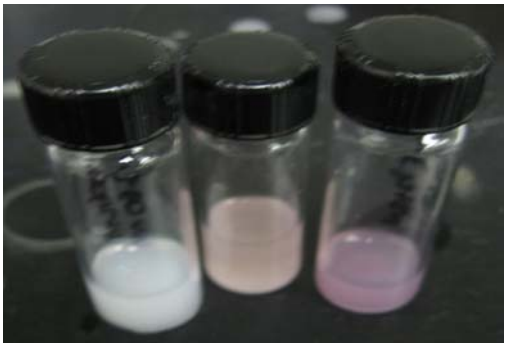

Figure 2.2. Colloidal solutions of (Left) aminated spheres, (Middle) with adsorbed Au nanoparticles and (Right) Au-coated.

Table 2.1. Summary of measured diameters (nm) for the prepared nanoparticles.

	DLS	SEM
As made	365 ± 40	350 ± 20
Preshrunk	368 ± 40	316 ± 20
Amine-modified	361 ± 40	317 ± 20
With adsorbed Au np	389 ± 40	323 ± 20
Au-coated	443 ± 40	338 ± 10
Sintered Au-coated		275 ± 10

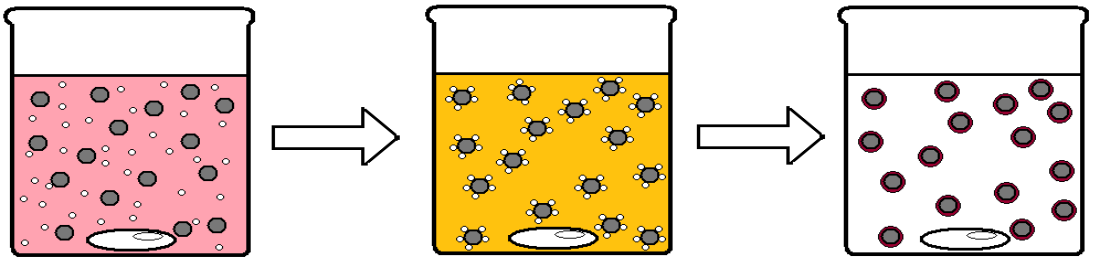

Figure 2.3. Electroless plating of SiO_2: (Left) Aminated nanospheres are immersed in a colloidal solution of Au nanoparticles, and are then (Middle) stirred in a plating solution of $HAuCl_4 \cdot 3H_2O$ in NH_2OH to produce (Right) a thin gold shell around the spheres.

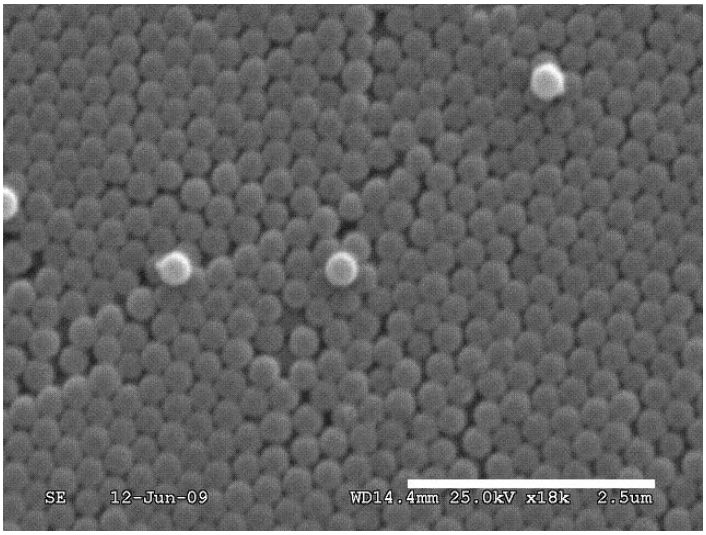

Figure 2.4. SEM image of sintered Au-coated SiO_2 membranes with PMAA grown for 10 min (scale bar = 2.5 μm).

SAMs. Tan et al.[37] reported that temperatures as low as 325 °C were sufficient to cause surface melting of the gold. TEM images showed that the gold-coated silica nanoparticles retained a uniform spherical shape (Figure 2.5). Sintering also led to the decrease in the nanosphere diameter, from 338 to 275 nm. Thus, the nanopore size in the resulting Au-coated nanofrits was 21 nm.

Surface-modification with *L*-cysteine

To determine whether charge-selective molecular transport could be achieved with the Au-coated nanofrits, we decided to study the concentration gradient (ΔC)-driven diffusion of a cationic dye, Rhodamine B, by measuring the diffusion rate R_D (mol·sec^{-1}) through a nanofrit of a known thickness L and area S (cm^2). R_D was determined by recording the number of moles of a molecule that diffused through the membrane as a function of time in an apparatus shown in

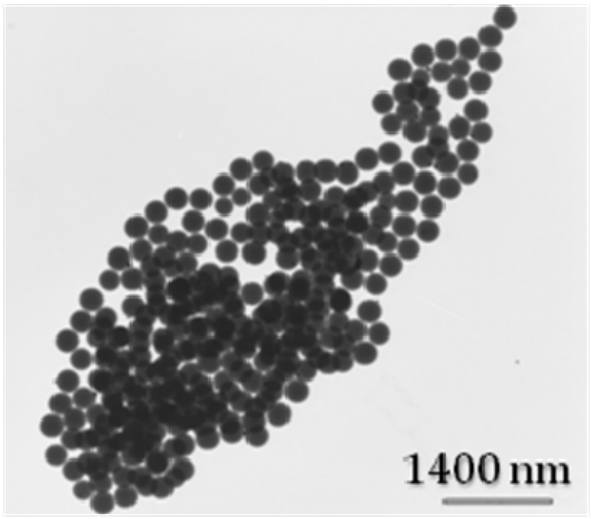

Figure 2.5. TEM image of Au-coated silica spheres (scale bar = 1400 nm).

Figure 2.6. Knowing the value of R_D allowed for the calculation of the molecular flux $J_{colloid}$ (mol·sec^{-1}·cm^{-2}) through the nanofrit (Equation 2.1).

$$R_D = J_{colloid} \times S \tag{2.1}$$

A solution for Fickian diffusion (Equation 2.2) can then be used to determine the effective diffusion coefficient D_{eff} (cm^2·sec^{-1}) of a diffusing species in a particular solvent (in this case water) as it traverses through the colloidal nanofrit.[38]

$$J_{colloid} = \frac{\Delta C}{L} \times D_{eff} \tag{2.2}$$

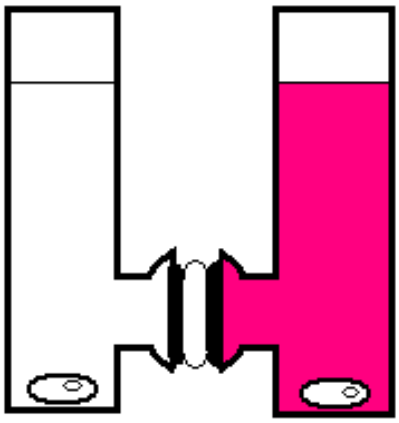

Figure 2.6. Diffusion experiment set-up. The absorbance at the reservoir cell (left) was monitored at the λ_{max} of the diffusing species from the feed cell (right).

D_{eff} values take into account the effect of intrinsic colloidal crystal properties such as void fraction ($\varepsilon = 0.26$) and tortuosity ($\tau \sim 3.0$) compared to the free diffusion coefficient in a given solvent D_{sol} (Equation 2.3):

$$D_{\text{eff}} = \frac{\varepsilon}{\tau} \times D_{\text{sol}} \tag{2.3}$$

Sintered Au-coated membranes were surface-modified by introducing a self-assembled monolayer (SAM) of *L*-cysteine (Figure 2.7). The presence of an IR band (Figure 2.8) corresponding to a carbonyl stretch (1735 cm^{-1}) confirmed the presence of *L*-cysteine on the surface but its weak intensity as well as negligible % weight loss in thermogravimetric analysis (TGA) experiments indicated less than optimal surface coverage. This explained the relatively low selectivity value (1.25) that was observed for the diffusion of Rhodamine B in the absence

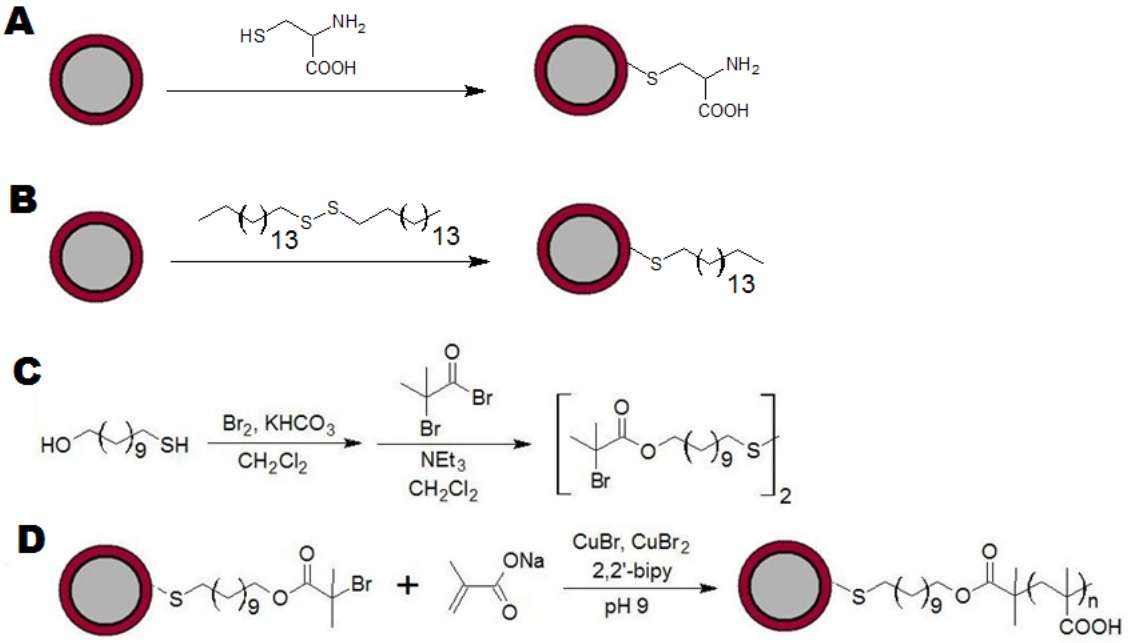

Figure 2.7. Reaction schemes for surface modification of the Au-coated SiO_2 spheres: (A) formation of a SAM of *L*-cysteine, (B) formation of a SAM of a 16-carbon *n*-alkyl chain, (C) synthesis of the initiator molecule for (D) the ATRP of PMAA.

and presence of trifluoroacetic acid (TFA) (Figure 2.9). Selectivity was calculated as the ratio of D_{eff} in the absence of and with acid. Upon addition of the acid, both amine and carboxylate groups in *L*-cysteine became protonated, resulting in a positively-charged nanopore surface. Thus, the diffusion rate was expected to be lower in the presence of the acid due to the electrostatic repulsion between the cationic dye and the nanopore surface and this was demonstrated to be the case from calculated D_{eff} values (Table 2.2).

To confirm that the above results were due to electrostatics, we decided to modify the nanopore surfaces with a non-ionizable moiety, specifically with a 16-carbon *n*-alkyl chain (Figure 2.7). Diffusion experiments of Rhodamine B through functionalized frits (Figure 2.10) showed no significant difference in calculated effective diffusion coefficients in the absence and

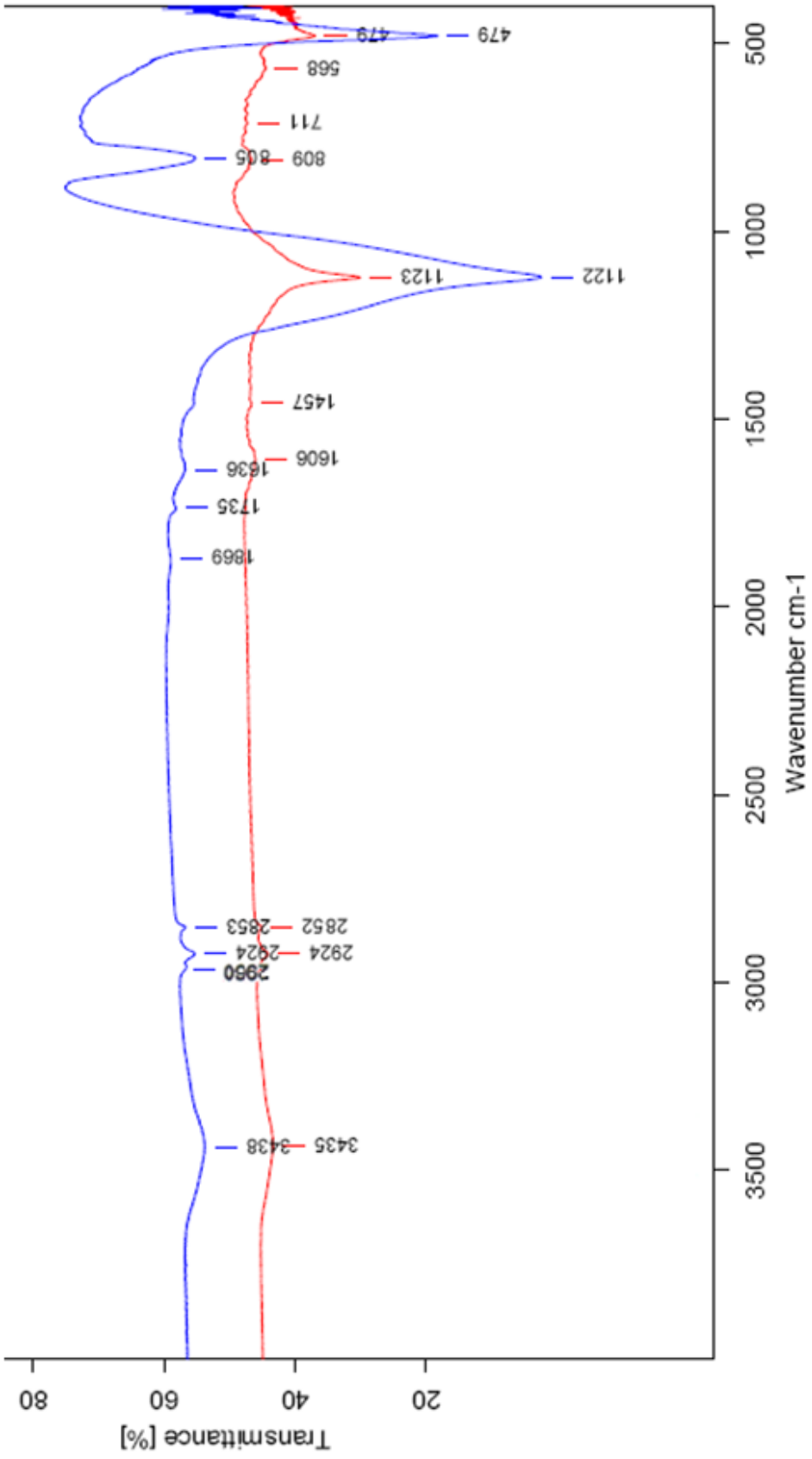

Figure 2.8. Comparison of the FT-IR spectra for unmodified (red) and *L*-cysteine-modified (blue) Au-coated SiO_2.

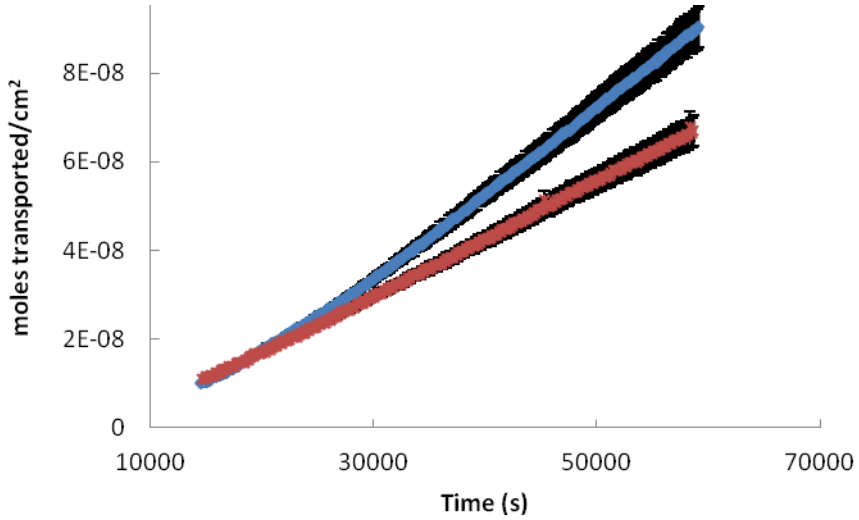

Figure 2.9. Comparison of the flux of Rhodamine B in the absence (blue) or presence (red) of an acid through *L*-cysteine-modified membranes.

Table 2.2. Summary of calculated average diffusion coefficients for Rhodamine B through *L*-cysteine and *n*-hexadecyl-modified gold-coated silica frits. Selectivity was calculated as the ratio of coefficients without and with acid.

Modified with	D_{eff} ($cm^2/sec \times 10^{-6}$)		Selectivity
	Without acid	With acid	
L-cysteine	3.6 ± 0.3	2.9 ± 0.2	1.3
n-hexadecyl	3.5 ± 0.1	3.6 ± 0.3	1.0

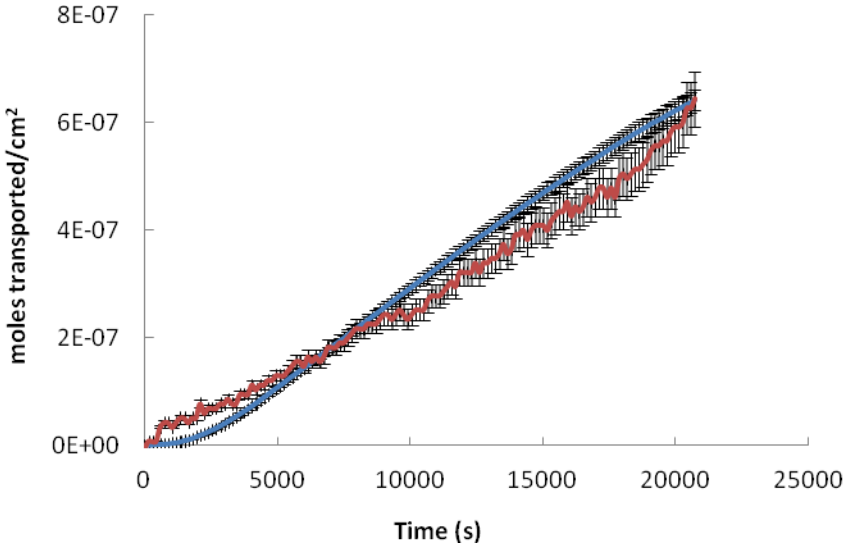

Figure 2.10. Comparison of the flux of Rhodamine B in the absence (blue) or presence (red) of an acid through *n*-hexadecyl-modified membranes.

presence of the acid (Table 2.2). It appears that these alkyl chains remained in a collapsed conformation near the nanopore surface as opposed to extending into the solution, as illustrated by the calculated diffusion coefficients (Table 2.2) that are similar to the literature value for Rhodamine B in free solution (3.6×10^{-6} cm^2/sec in water at 21.5 °C).[39] This behavior was expected since water is a poor solvent for hydrophobic moieties. In a less polar solvent, the alkyl chains can extend into the solution and this would reduce the effective pore size. In such case, lower diffusion rates would have been observed.

Surface-modification with PMAA

To manipulate the effective nanopore size, we wanted surface modifiers with tunable sterics arising from variations in molecular weight or conformation. Thus, weak polyelectrolyte brushes of PMAA were covalently bound to the gold surface. Exploiting this approach afforded a

three-dimensional arrangement of the -COOH groups compared to the planar arrangement in a typical SAM. In order to demonstrate that atom-transfer radical polymerization (ATRP) of PMAA can be performed on the gold surface (Figure 2.7), silica spheres in colloidal solution were modified with an initiator moiety followed by the treatment with sodium methacrylate in the presence of a copper(I) catalyst. TEM images of the modified nanoparticles (Figure 2.11) that were rigorously washed via sonication confirmed the presence of organic moieties that were covalently bound from the surface. The polymer growth as a function of polymerization time was monitored by DLS and TGA experiments, and the polymer brush length and degree of polymerization *n* were calculated. The results of these measurements are shown in Table 2.3. The TGA curves show increasing % weight loss with increasing ATRP time; % weight losses around ~240 – 250 °C can be attributed to initiator decomposition, while PMAA is lost from ~375 – 420 °C (Figure 2.12).

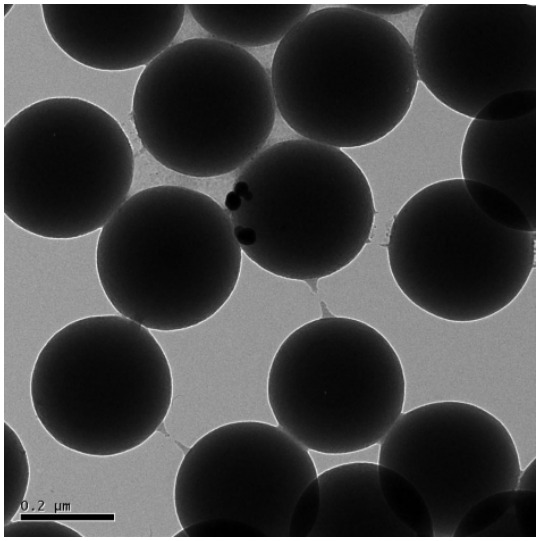

Figure 2.11. TEM image of Au-coated SiO_2 spheres with PMAA grown for 30 min (scale bar = 200 nm).

Table 2.3. Comparison of DLS and TGA data for PMAA-modified loose Au-coated silica spheres. The calculated polymer brush lengths based on TGA data were obtained with the assumption that all initiators reacted to grow PMAA and with the aid of Chem3D estimated 1.7 nm contribution of the initiator molecule and 0.25 nm each monomer unit.

	DLS Data	
	Diameter (nm)	Brush length (nm)
Initiator-modified	346 ± 20	
5 min ATRP time	386 ± 30	20
10 min ATRP time	425 ± 30	39
15 min ATRP time	509 ± 40	81
25 min ATRP time	560 ± 60	107
	TGA Data	
	% Weight loss above 200 °C	Calculated results
Initiator-modified	0.5614% initiator	4.16×10^6 initiators/sphere; 6.75 initiators/nm^2
5 min ATRP time	4.287% total organic matter (0.4122% initiator, 3.8748% PMAA)	29.75 repeating units; polymer brush length 9.14 nm
10 min ATRP time	4.687% total organic matter (0.4101% initiator, 4.2769% PMAA)	33.01 repeating units; polymer brush length 10 nm
15 min ATRP time	5.920% total organic matter (0.4038% initiator, 5.5162% PMAA)	43.25 repeating units; polymer brush length 12.5 nm
25 min ATRP time	8.197% total organic matter (0.3970% initiator, 7.800% PMAA)	62.18 repeating units; polymer brush length 17.3 nm

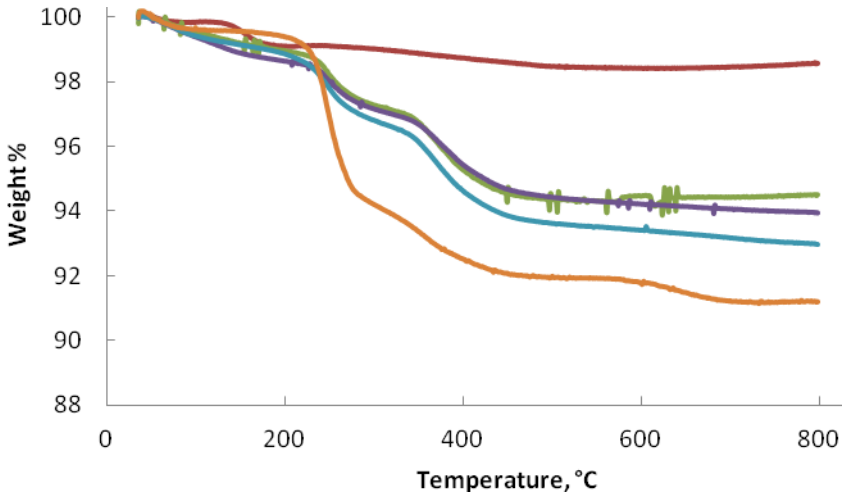

Figure 2.12. TGA of initiator-modified (red) Au-coated SiO_2 spheres with PMAA grown from the surface for 5 min (green), 10 min (purple), 15 min (blue) and 25 min (orange) polymerization times.

Next, we prepared PMAA-modified Au-coated nanofrits by ATRP. The sintered substrates were first modified with a SAM of the initiator then soaked in a mixture of the methacrylate monomer and copper(I) catalyst for various reaction times. To determine if PMAA polymer brushes inside the nanopores respond to variations in the pH, we decided to study the diffusion of a neutral dye so that any changes in flux could be attributed to changes in polymer conformation alone and not to interactions between PMAA chains and the diffusing species. Diffusion experiments of ferrocenecarboxaldehyde, Fc(CHO), through PMAA-modified nanofrits (Figures 2.4, 2.13) showed that there was a general trend of decreasing rate of diffusion with increasing length of polymer chains within the nanopores (Figure 2.14). The incorporation of polymers inside the nanopores resulted to a decrease in the effective size of the nanopores as they became partially blocked. Comparison of the calculated D_{eff} values showed that diffusion was hindered by a factor of 7.6 as the polymer brushes inside the nanopores were allowed to grow for

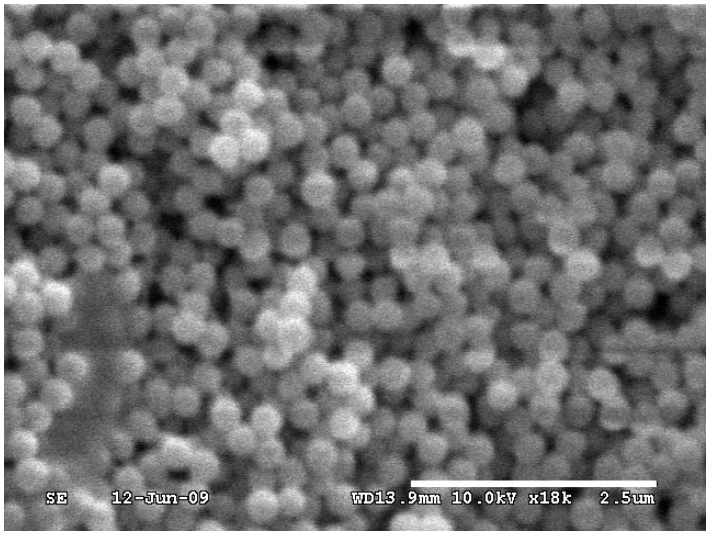

Figure 2.13. SEM image of sintered Au-coated SiO_2 membranes with PMAA grown for 30 min (scale bar = 2.5 μm). Prolonged polymerization times appeared to perturb the membrane surface.

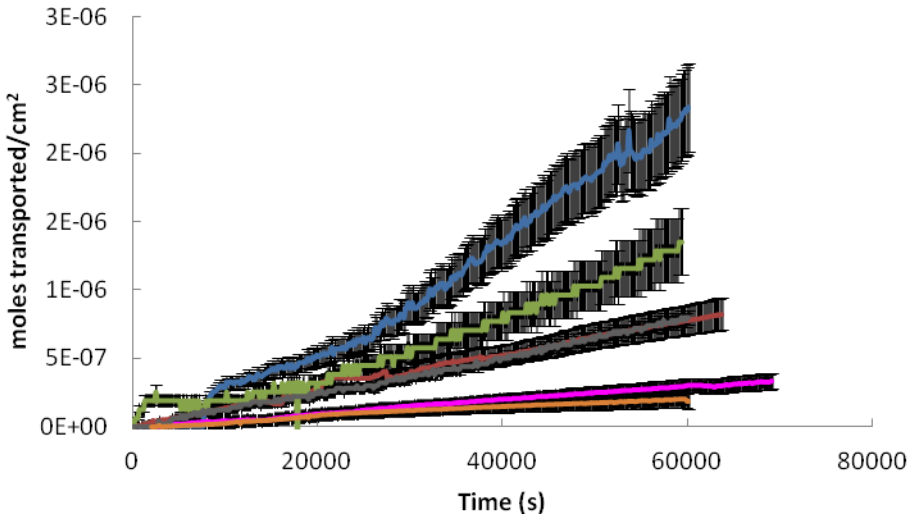

Figure 2.14. Comparison of the flux of ferrocenecarboxaldehyde through frits modified via ATRP for 10 min (with acid, blue; without acid, red), 30 min (with acid, green; without acid, pink) and 45 min (with acid, gray; without acid, orange).

30 min. We did not observe complete blockage of the nanopores even as ATRP time was extended until 45 min, as the calculated D_{eff} values for Fc(CHO) in 30- and 40-min ATRP-modified frits were similar. It is possible that the polymerization reaction slowed down considerably after 30 min.

Upon addition of 50 mM trifluoroacetic acid to the diffusion solution, we observed an increased flux for Fc(CHO) through the nanofrits (Table 2.4). This was consistent with the known behavior of PMAA in response to pH changes. In the absence of TFA, the polymer brushes are extended as a result of a significant degree of dissociation of the –COOH groups. Indeed, the solution pH~7 was higher than the pK_a~5 of PMAA.[40] In the presence of TFA, deprotonation along the chain is suppressed and thus the polymers undergo de-swelling as

Table 2.4. Summary of calculated average diffusion coefficients for ferrocenecarboxaldehyde and Rhodamine B through PMAA-modified gold-coated silica frits. Selectivity was calculated as the ratio of coefficients with and without acid.

Modified with	D_{eff} ($cm^2/sec \times 10^{-6}$)		Selectivity
	Without acid	With acid	
	Ferrocenecarboxaldehyde		
10 min PMAA	6.7 ± 0.6	16 ± 2	2.4
30 min PMAA	0.9 ± 0.2	12 ± 2	14
45 min PMAA	0.9 ± 0.3	10 ± 3	12
	Rhodamine B		
10 min PMAA	2.4 ± 0.2	2.2 ± 0.5	0.9
15 min PMAA	2.4 ± 0.6	1.0 ± 0.1	0.4
30 min PMAA	3 ± 2	0.18 ± 0.07	0.06
45 min PMAA	3 ± 2	0.2 ± 0.1	0.07

electrostatic repulsions are minimized. The PMAA chains fold and collapse closer to the surface, thus leading to larger channels within the nanopores. The calculated selectivities, obtained as the ratio of D_{eff} in the presence and absence of acid (Table 2.4), illustrated that the PMAA brushes within our nanopores were indeed pH-responsive. pH-permselectivity was only slightly more than 2 for a sintered Au-coated membrane after 10 min ATRP, but increased to 14 after the 30-min ATRP.

We then studied the nature of the interaction between the nanopore surface and the diffusing species on the transport properties of our membranes. Diffusion experiments for the cationic dye, Rhodamine B, were carried out with and without TFA present. Figure 2.15 shows that the results are opposite to the trend observed for Fc(CHO). Instead of exhibiting greater diffusion rates as the polymer chains were fully protonated, diffusion appeared to be more hindered under this condition, and less hindered through the nanopores carrying polyanionic

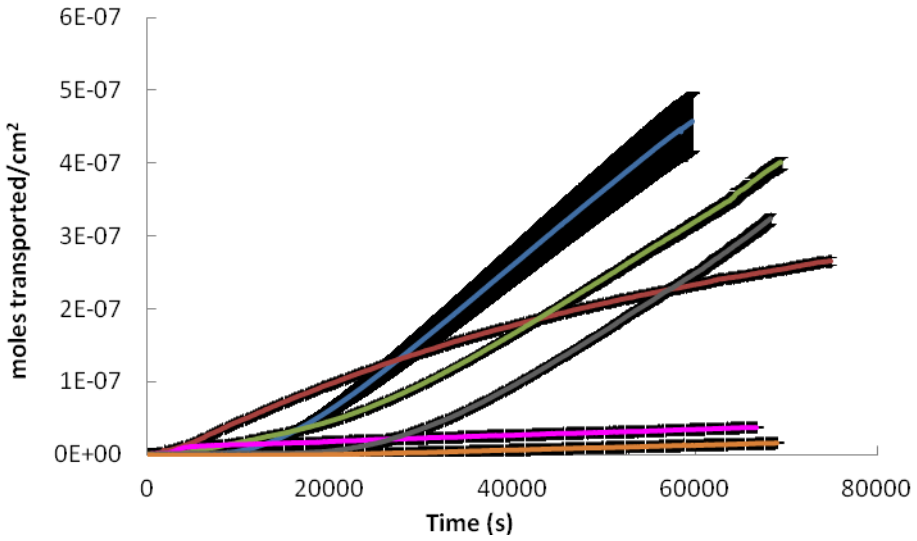

Figure 2.15. Comparison of the flux of Rhodamine B through frits modified via ATRP for 10 min (without acid, blue; with acid, red), 30 min (without acid, green; with acid, pink) and 45 min (without acid, gray; with acid, orange).

brushes (Table 2.4). Our rationalization of the above observations is presented below.

It is well-known that polycarboxylates show a specific response when exposed to different cations. A survey of literature revealed that PMAA brushes have unusual interactions with metal cations (Group 1A, 2A, transition metals) in that electrostatic attraction between the metal cations and the carboxylate groups results in a collapse of the brushes at metal cation concentrations as low as 1 mM.[25-27] The resulting zero net charge in the system leads to increased hydrophobic interactions as both polyanion and the cation undergo partial dehydration (i.e. water becomes a less effective solvent resulting in the shrinkage of the polymer).[24] In the presence of counterions other than $H^+_{(aq)}$, the behavior of PMAA depends on both electrostatic and hydrophobic interactions.

We propose that a similar phenomenon occurs in our case. At neutral pH (no acid added), the carboxylic acid moieties in our polymer brushes are dissociated to some extent and, therefore, carry negative charges. The binding of Rhodamine B (a cationic dye) to the polycarboxylate arises from electrostatic attraction. Accommodation of Rhodamine B as a counterion disrupts the extensive network of water molecules and expels some of the water molecules in the immediate vicinity of the dye-brush interaction. This partial dehydration enhances the hydrophobic interactions along the chain, which causes the polymer brushes to collapse. Without acid, we observed only small differences in D_{eff} for Rhodamine B going from 10- to 45-min PMAA-modified frits (Table 2.2). This suggests that the PMAA brushes were collapsed such that the effective nanopore size in all frits was roughly the same.

We did not observe a significant extent of polymer collapse upon addition of an acid, presumably due to the lack of deprotonated moieties that could interact with the dye cation. It seems that the polymer shrinkage as a result of interaction with Rhodamine B is greater compared to the effect of fully protonating the polymer chain. Thus, the polymer brushes were more extended in the presence of an acid and Rhodamine B diffused more slowly since the nanopores were more sterically blocked. Comparison of the calculated selectivities showed that this effect

was more pronounced with longer polymer chains (Table 2.2). The selectivity increased 6.6 times when polymerization time increased from 15 to 30 min.

We therefore performed a simple test to confirm the above rationalization. Size measurements via DLS for loose Au-coated spheres modified via ATRP for 30 min were used to investigate the brush length as a function of Rhodamine B concentration (Figure 2.16) in the range of concentrations comparable to that used in our diffusion experiments. It is apparent that PMAA brush lengths decreased with increasing concentration of Rhodamine B, supporting our proposed explanation. But a closer look at low dye concentrations (Figure 2.17) revealed that the extent of swelling initially increased and reached a maximum at a critical concentration of 0.1 mM of Rhodamine B. These swelling properties of PMAA affected by counterion concentration are similar to those in the presence of monovalent cations like Na^+, as reported extensively by Rühe and coworkers.[25-27] Below the critical concentration in what is referred to as the osmotic brush regime, the high concentration of Rhodamine B inside the polymer brush layer (compared to the bulk solution) caused a higher osmotic pressure in the brush than in the adjacent solution. This osmotic pressure difference and electrostatic repulsion explained the brush swelling. Above the critical concentration is the salted brush regime, the brush thickness decreased with increasing dye concentration as the charged groups along the chain became more effectively screened and as the differences in osmotic pressures became smaller.

We also compared the swollen brush lengths for polymer-coated spheres in the presence of 2.5 mM Rhodamine B alone, 50 mM TFA alone, and with both 2.5 mM Rhodamine B and 50 mM TFA added (Figure 2.16). These concentrations were the conditions employed in the diffusion experiments and it is noted that this dye concentration was above the experimentally determined critical concentration. From the results of diffusion experiments for Rhodamine B, it was expected that samples with Rhodamine B would have significantly less brush swelling than with TFA added alone. However, the measured differences were not pronounced since adsorption of the dye (1.6 nm diameter)[41] could be contributing to the hydrodynamic volume of

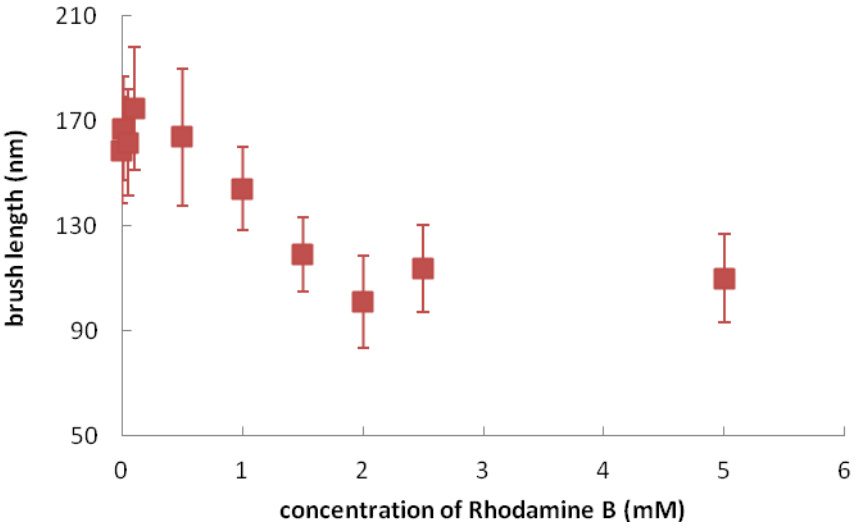

Figure 2.16. Brush length of PMAA grown for 30 min onto loose Au-coated SiO_2 spheres as a function of the concentration of Rhodamine B.

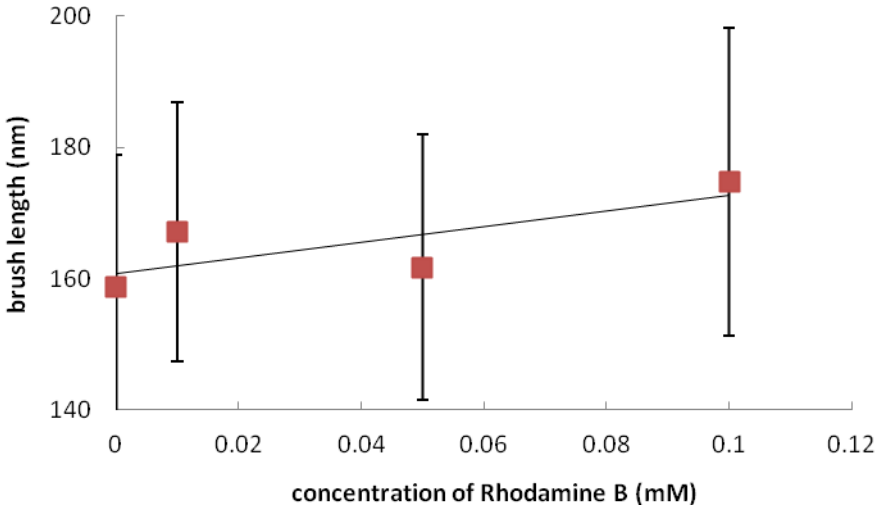

Figure 2.17. Brush length of PMAA grown for 30 min onto loose Au-coated SiO_2 spheres as a function of the concentration of Rhodamine B in the osmotic brush regime (the line is included as a guide for the eye).

the particles. As such, the hydrated brush lengths for polymers exposed to Rhodamine B alone, TFA alone or both dye and acid were all within experimental uncertainties.

We decided to further study the ion-response to Rhodamine B for PMAA inside the nanopores. Thus, we studied the diffusion of Fc(CHO) in the presence of either 2.5 mM Rhodamine B or 50 mM $NaNO_3$ (chosen to match the concentration of TFA and well above the transition from osmotic to salted brush regimes) through the membranes modified with PMAA grown for 30 min. Figure 2.18 shows a representative plot comparing the flux of the neutral dye as the environment is changed either by varying the pH or with the addition of cations that can interact with the polymer chains. Diffusion rates in the presence of either acid, Rhodamine B or Na^+ were all higher with respect to diffusion in water, in agreement with observations previously discussed. Table 2.5 summarizes the average D_{eff} values for Fc(CHO) and the transport selectivities calculated as the ratio of coefficients in the presence and absence of added counterions (Rhodamine B, $H^+_{(aq)}$ or $Na^+_{(aq)}$). The transport selectivity was consistently enhanced by a factor of ca. 15 by employing polymers grown for at least 30 min within the nanopores. Considering that the concentration of Rhodamine B was much smaller compared to either TFA or Na^+ (2.5 mM << 50 mM), this suggested that the cationic dye caused the de-swelling of PMAA chains most effectively. These results supported our theory that induced dominance of hydrophobic interactions within the polymer chain (as a result of adding the dye counterion) can lead to greater brush de-swelling than lowering the pH.

Conclusions

We prepared free-standing colloidal nanofrits composed of gold-coated silica spheres whose nanopore surfaces have been modified with various organic moieties, and studied the molecular transport of neutral and cationic species across the membranes as a function of pH and of the counterions present. We found that transport through nanopores with *n*-alkyl modifiers were not affected by changes in pH, but that diffusion rates for a cationic species through *L*-

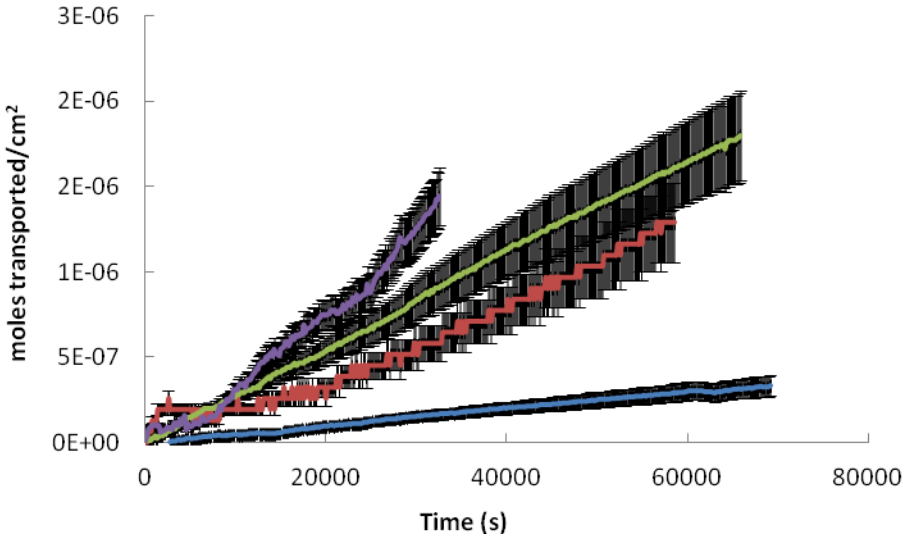

Figure 2.18. Comparison of the flux of ferrocenecarboxaldehyde through frits modified via ATRP for 30 min as the environment was varied: in water (blue), 50 mM TFA (red), 50 mM $NaNO_3$ (green) and 2.5 mM Rhodamine B (purple).

Table 2.5. Summary of calculated average diffusion coefficients for ferrocenecarboxaldehyde in various solutions through 30-min PMAA-modified gold-coated silica frits. Selectivity was calculated as the ratio of coefficients with respect to water.

Diffusion solution	D_{eff} (cm^2/sec $\times 10^{-6}$)	Selectivity
Water	0.9 ± 0.2	1.00
50 mM TFA	13 ± 2	14
2.5 mM Rhodamine B	12 ± 3	13
50 mM $NaNO_3$	12 ± 3	13

cysteine-modified nanopores decreased slightly in the presence of an acid due to electrostatic effects. We also grew PMAA brushes of various lengths inside the nanopores via surface-initiated ATRP by controlling the polymerization time. We discovered that the transport in the polymer-modified membranes is both pH- and ion-responsive. The diffusion rates of neutral molecules increased with decreasing pH and with increasing counterion concentration in the salted brush regime. This effect was more pronounced with longer PMAA chains due to combined electrostatic and steric effects. We also found that PMAA undergoes conformational changes in the presence of Rhodamine B in a manner similar to its swelling behavior in the presence of Na^+ arising from both electrostatic and hydrophobic interactions between the counterion and PMAA chains.

References

(1) IUPAC. Compendium of Chemical Terminology, 2nd ed. ("Gold Book") Compiled by A.D. McNaught and A. Wilkinson. Blackwell Scientific Publications, Oxford (1997).

(2) (a) Qurashi,A. in: Pilla, S. (Ed.), Handbook of Bioplastics and Biocomposites Engineering Applications, Scrivener Publishing. Massachusetts, 2011, 357-370. (b) Ma, H.; Burger, C.; Hsiao, B.S.; Chu, B. *Biomacromolecules* **2011**, *12*, 970. (c) Uragami, T. in: Kim, S.-K. (Ed.), Chitin, Chitosan, Oligosaccharides and Their Derivatives, CRC Press. Florida, 2011, 481-506. (d) Schiffman, J.D.; Schauer, C.L. in: Chang, W.N. (Ed.), Nanofibers, Nova Science Publishers, Inc. New York, 2009, 61-71.

(3) Pellegrino, J.J.; Geer, S.; Maegley, K.; Rivera, R.; Steward, D.; Ko, M. *Ann. N.Y. Acad. Sci.* **1990**, *589*, 229.

(4) Toh, C.-S.; Kayes, B. M.; Nemanick, E. J.; Lewis, N. S. *Nano Lett.* **2004**, *5*, 767.

(5) Tong, H. D.; Jansen, H. V.; Gadgil, V. J.; Bostan, C. G.; Berenschot, C. G. E.; van Rijn, C. J. M.; Elwenspoek, M. *Nano Lett.* **2004**, *4*, 283.

(6) McPhie, P. *Meth. Enzymol.* **1971**, *22*, 23.

(7) Burggraaf, A.J.; Keizer, K.; de Lange, R.S.A.; Vroon, Z.A.E.P.; Zaspalis, V.T. *Proc. Int. Zeolite Conf., 9th* **1993**, *1*, 47.

(8) Schepelina, O.; Zharov, I. *Langmuir* **2006**, *22*, 10523.

(9) Jiang, P.; Bertone, J. F.; Hwang, K. S.; Colvin, V. L. *Chem. Mater.* **1999**, *11*, 2132.

(10) Wong, S.; Kitaev, V.; Ozin, G. A. *J. Am. Chem. Soc.* **2003**, *125*, 15589.

(11) (a) Bruening, M.L.; Dotzauer, D.M.; Jain, P.; Ouyang, L.; Baker, G.L. *Langmuir* **2008**, *24*, 7663. (b) Tagliazucchi, M.; Rabin, Y.; Szleifer, I. *J. Am. Chem. Soc.* **2011**, *133*, 17753.

(12) (a) Huang, S.; Yin, Y. *Analytical Sciences* **2006**, *22*, 1005. (b) Sun, X.; Wang, X.; Du, S.; Zhao, W.; Li, Q.; Han, X. *Sensors Letters* **2011**, *9*, 958. (c) Wang, Y. *Microchimica Acta* **2011**, *172*, 419. (d) Umuhumuza, L.C.; Sun, X. *European Food Research and Technology* **2011**, *232*, 425.

(13) Hou, Z.; Abbott, N.L.; Stroeve, P. *Langmuir* **2000**, *16*, 2401.

(14) Chun, K.Y.; Mafé, S.; Ramírez, P.; Stroeve, P. *Chemical Physics Letters* **2006**, *418*, 561.

(15) Asandei, A.; Pintilie, F.; Luchian, T. *Romanian J. Biophys.* **2006**, *16*, 273.

(16) Velleman, L.; Shapter, J.G.; Losic, D. *Journal of Membrane Science* **2009**, *328*, 121.

(17) Hulteen, J.C.; Jirage, K.B.; Martin, C.R. *J. Am. Chem. Soc.* **1998**, *120*, 603.

(18) Smuleac, V.; Butterfield, D.A.; Bhattacharyya, D. *Chem. Mater.* **2004**, *16*, 2762.

(19) Zhang, H.; Ito, Y. *Langmuir* **2001**, *17*, 8336.

(20) (a) Fu, X.-C.; Wu, J.; Nie, L.; Xie, C.-G.; Liu, J.-H.; Huang, X.-J. Analytica Chimica Acta 2012, 720. (b) Zhang, H.; Xia, H.; Zhao, Y. *J. Mater. Chem.* **2012**, *22*, 845. (c) Rodriguez-Emmenegger, C.; Hasan, E.; Pop-Georgievski, O.; Houska, M.; Brynda, E.; Alles, A.B. Macromol. *Biosci.* **2012**, doi: 10.1002/mabi.201100425 (d) Baker, G.L. *Polymer Preprints* **2011**, *52*, 505. (e) Lobbicke, R.; Chanana, M.; Schlaad, H.; Pilz-Allen, C.; Gunter, C.; Mohwald, H.; Taubert, A. *Biomacromolecules* **2011**, *12*, 3753.

(21) Lokuge, I.; Wang, X.; Bohn, P.W. *Langmuir* **2007**, *23*, 305.

(22) Yu, S.; Lee, S.B.; Kang, M.; Martin, C.R. *Nano Letters* **2001**, *1*, 495.

(23) Schepelina, O.; Zharov, I. *Langmuir* **2008**, *24*, 14188.

(24) Advincula, R.C.; Brittain, W.J.; Caster, K.C.; Rühe, J. (Eds.) *Polymer Brushes: Synthesis, Characterization, Applications*; Wiley-VCH: Germany, 2004.

(25) Biesalski, M.; Johannsmann, D.; Rühe, J. *J. Chem. Phys.* **2002**, *117*, 4988.

(26) Zhang, H.; Rühe, J. *Macromolecules* **2005**, *38*, 4855.

(27) Konradi, R.; Rühe, J. *Macromolecules* **2005**, *38*, 4345.

(28) Stöber, W.; Fink, A.; Bohn, E. *J. Colloid Interface Sci.* **1968**, *26*, 62.

(29) Wang, W.; Gu, B.; Liang, L.; Hamilton, W. *J. Phys. Chem. B* **2003**, *107*, 3400.

(30) Le, T. V.; Ross, E. E.; Velarde, T. R. C.; Legg, M. A.; Wirth, M. J. *Langmuir* **2007**, *23*, 8554.

(31) Chabanov, A. A.; Jun, Y.; Norris, D. J. *Appl. Phys. Lett.* **2004**, *84*, 3573.

(32) Zheng, S.; Ross, E.; Legg, M. A.; Wirth, M. J. *J. Am. Chem. Soc.* **2006**, *128*, 9016.

(33) Lu, L.; Randjelovic, I.; Capek, R.; Gaponik, N.; Yang, J.; Zhang, H.; Eychmüller, A. *Chem. Mater.* **2005**, *17*, 5731.

(34) Lee, S.B.; Martin, C.R. *Anal. Chem.* **2001**, *73*, 768.

(35) Shah, R.R.; Merreceyes, D.; Husemann, M; Rees, I.; Abbott, N.L.; Hawker, C.J.; Hedrick, J.L. *Macromolecules* **2000**, *33*, 597.

(36) Dong, R.; Lindau, M.;Ober, C.K. *Langmuir* **2009**, *25*, 4774.

(37) Tan, B.J.Y.; Sow, C.H.; Koh, T.S.; Chin, K.C.; Wee, A.T.S.; Ong, C.K. *J. Phys. Chem. B* **2005**, *109*, 11100.

(38) Cussler, E.L. *Diffusion: Mass Transfer in Fluid Systems, 2nd ed.*; Cambridge University Press: New York, 1997.

(39) Rani, S.A.; Pitts, B.; Stewart, P.S. *Antimicrob. Agents Chemother.* **2005**, *49*, 728.

(40) Kim, B.; Lim, S.H.; Ryoo, W. *Journal of Biomaterials Science* **2009**, *20*, 427.

(41) Klein, S.A.; Wilk, S.J.; Thornton, T.J.; Posner, J.D. *International Symposium on Advanced Nanodevices and Nanotechnology Journal of Physics: Conference Series* **2008**, *109*, 012022.

CHAPTER 3

CHIRAL PERMSELECTIVITY IN COLLOIDAL NANOFRITS SURFACE-MODIFIED WITH CHIRAL MOIETIES

Introduction

Separations are important in almost all fields of chemistry (whether fundamental or applied) and in many industries, particularly in the production of pharmaceuticals, foods, agricultural chemicals, perfumes, and high purity reagents for research purposes, to name a few.[1,2] Perhaps one of the most challenging separations is the preparation of optically pure enantiomers.[3] In an achiral environment, enantiomers of a chiral molecule have indistinguishable physical and chemical properties[4] except for their non-superimposable mirror-image geometries[5] that allow them to interact with plane-polarized light differently. Once placed in a chiral environment (i.e., dissolution in a chiral medium or mixed with other chiral entities), however, one enantiomer may exhibit different chemical or biological properties than the other enantiomer.[4]

When one considers that two major components of living systems are produced in the body as enantiopure *D*-sugars and *L*-amino acids,[6] it is not surprising that most drug effects are dependent on interactions with chiral biological molecules.[7] Due to the stereoselectivity of enzymatic and other biological processes, each of the enantiomers can have vastly different pharmacologic behavior[8] with one isomer showing beneficial therapeutic activities and the other being an inert impurity at best unless it leads to undesirable side effects.[9] Many active drugs, agrochemicals, food flavorings and fragrance components are racemates (mixtures of equal

amounts of enantiomers) wherein the nondesired enantiomer may be regarded as 50% impurity.[10] For these reasons, the Food and Drug Administration has encouraged several years ago the drug manufacturers to supply enantiopure therapeutic agents or prove that the use of a racemic mixture would be more beneficial.[8] Since then, the demand for efficient chiral separations that can be especially adapted for large-scale purifications has significantly increased.[11]

Optically pure compounds can be obtained via asymmetric syntheses from achiral starting materials. However, for the reaction to favor one chiral product, a catalyst that is itself chiral and enantiopure is required.[5] The low over-all yields of many of these expensive synthetic routes and the slow progress in the development of optimized reaction conditions make this method unable to keep with the high demand for producing single enantiomers. Instead, a more popular alternative is the separation of racemic mixtures to yield the desired product in enantiopure form.

Most industrial separations employ either diastereomeric resolution or chromatography.[10] The former could include diastereomeric salt crystallization and kinetic resolution.[8,11] Selective crystallization may be as straightforward as exploiting the differences in the solubility of the racemate and one of the enantiomers, but this method requires an initial enantiomeric excess which, in turn, necessitates a preceding step to gain the enantiomeric enrichment.[10] Alternatively, an organic racemate can be resolved by treatment with an enantiopure agent that selectively forms an insoluble acid-base or host-guest complex with one of the enantiomers.[12] Overall, crystallization is expensive and time-consuming.[13] On the other hand, kinetic resolution can be achieved based on different reaction rates of each enantiomer with a chiral entity. This includes stereoselective enzyme catalysis that converts one of the enantiomers while the desired enantiomer remains. However, kinetic resolution can be very costly due to its single operation.

Chromatography offers several enantioselective methods such as HPLC, high resolution GC, multidimensional GC, capillary electrophoresis and supercritical fluid chromatography.[11] Chiral separations depend on the ability to recognize and discriminate one of the enantiomers.[14]

This relies on a difference in strength of interactions between the enantiomers and a chiral selector to form diastereomeric complexes of different stabilities.[15] Pirkle's 3-point rule states that a minimum of three simultaneous interactions between one of the enantiomers (*A*, *B* and *C* portions) and the chiral selector (corresponding regions *a*, *b* and *c*) is required, with at least one of these interactions being stereochemically dependent.[16] One of the enantiomers will have a suitable 3D structure such that *A*, *B* and *C* will align with *a*, *b* and *c*, respectively. In contrast, the other enantiomer will have a lower binding affinity because it is not able to have all three simultaneous interactions regardless of its rotation in space despite possessing all of the same groups *A*, *B*, *C* and *D*.[4] The interactions involved in chiral recognition are typically noncovalent and include H-bonding, coulombic, dipole-dipole, Van der Waals, hydrophobic and $\pi - \pi$ interactions to name a few. Chiral chromatographic separations rely on the formation of transient diastereomeric complexes between a chiral environment (active sites within the column such as chiral stationary phases) and one of the racemate components. If the association complexes are sufficiently energetically unequal, the enantiomer that forms the less stable complex is eluted first. Miyabe and coworkers[17] recently investigated the chiral recognition ability of a series of poly(phenyl isocyanide)s with macromolecular helicity as chiral stationary phases for HPLC. The optically active polymers exhibited enantioseparation factors (taken as the ratio of the retention times of the two enantiomers) ranging from 1 to 1.55 for racemates of cyclic ethers, amines, ketones and methyl acetylacetonate complexes. Hühnerfuss and Shah gave an excellent review on enantioselective chromatography containing a lengthy discussion on mechanisms of operation and an explanation of the key features of chromatograms using general principles of chirality.[16] The main limitation of chromatography is its nonsuitability for gram-quantity scale-up.[13] All methods mentioned thus far are plagued by high energy consumption, steep cost, low efficiency and discontinuous operation.[11]

Alternatively, membrane-based separations have generated immense interest[1,7-11,15,13,18-36] because of their attractive features such as economical, modular, easy to scale up and

continuous operation.[20] A thorough survey of literature shows that both liquid and solid membranes have been prepared and assessed for applicability in chiral separations. A comprehensive review by Xie and coauthors[11] summarized the principles and recent progress in the preparation and application of enantioselective liquid and solid membranes for chiral resolution. Liquid membranes are typically bulk water-oil-water (and occasionally oil-water-oil)[33] systems wherein liquid-liquid transport of one enantiomer is preferentially facilitated by chiral carriers within the liquid membrane that form soluble diastereomeric complexes. For liquid membranes to be an appropriate means of separation, the solubility of the free enantiomers in the liquid membrane must be minimal while the solubility of the carrier and enantiomer-carrier complex has to be negligible in the adjacent phases.[10] Glycopyranosyl derivatives,[37] chiral crown ethers,[26] chiral calixarenes modified with aminonaphthol moieties[31] or amino alcohol functionalities,[7] cinchona alkaloid derivatives,[28] cyclodextrins,[29,38] transition metal complexes bearing chiral ligands (such as Cu(II) *N*-dodecyl-(*L*)-hydroxyproline)[23] and serum albumins[33] have been employed as chiral carriers for the separation of racemic mixtures of chiral drug enantiomers[37] (such as ketoprofen and ibuprofen esters[33]), amino acids[26,28] and their derivatives,[7,31] chiral ions such ephedrinium,[38] pinenes[29] and mandelic acid[7,31] (an important intermediate reagent for asymmetric synthesis[19]). Despite the simplicity of the set-up of most liquid membranes (typically a U-cell), such systems could present difficulties due to the instability of the liquid membrane.[8]

Compared to liquid membranes, there is a much greater number of reports on utilizing solid membranes for chiral separations due to their durability. An interesting aspect of solid membranes is that the mechanism of selective transport may vary from one racemate to another depending on the strength of interactions between the enantiomers and the chiral recognition sites within the membrane. The terms vary across the literature, but the concepts can be summarized as follows. *Channel-type* membranes resolve racemates on the basis of differing diffusion rates of the two enantiomers.[11] Due to unequal binding affinities, one enantiomer will continuously

adsorb and desorb from one chiral site to the next such that its transport is said to be *facilitated* akin to a hopping mechanism. The higher permeation of such an enantiomer[34] leads to a *diffusion-enantioselective* mode of resolution. To maximize chiral permselectivity, smaller pore diameters are desirable to minimize the nonenantioselective diffusion of the weaker-binding enantiomer.[11] However, this translates into decreased permeability of the membrane and, consequently, lower flux of the diffusing species. This inherent trade-off between separation selectivity and throughput is the main disadvantage associated with the use of membranes operating based on this mechanism.[8]

The second mechanism of transport is *affinity-based* wherein the adsorbed enantiomer is retained within the membrane such that its transport becomes *retarded*.[11] The other enantiomer passes through the membrane at higher flux because of its lower binding affinity.[34] The substance-selector interactions are stronger than those in diffusion-selective membranes. The separation efficiency of these *adsorption-selective* membranes is mainly determined by the availability of binding sites; upon saturation of chiral recognition sites, enantioselectivity is lost.[11] But unlike the former mechanism, retarded transport allows for high enantioselectivity while retaining high flux. Other than the magnitude of the interactions between the analyte and the chiral environment, the choice of driving force for the mass transfer across the membrane can also affect the mechanism of enantioselective transport within the membrane. The use of a pressure gradient circumvents the slow permeation commonly observed with dialysis membranes that rely on concentration gradients[8] and can favor the membranes to function via the sorption-selective mode.[11] Enantioselective electrodialysis adopts a potential difference as a driving force and allows for tunable permselectivities by varying the applied potential difference.[27,30,32,35]

The almost limitless choice of materials for preparing solid membranes contributes to the popularity of these systems. These materials encompass the range of bioorganic, hybrid composites and inorganic. The rapid development of polymer-based membranes has generated much work, which has been nicely reviewed by Higuchi et al.[8] Chiral separation membranes

have been prepared from polymers that contain chiral centers either along the main chain or on the branches. Inherently achiral membranes can gain optical activity either via molecular imprinting or by exploiting the one-handedness of helical conformations of polymers. Amino acids such as aspartic acid[35] and glutamic acid[27] have been incorporated into polyamides as chiral moieties; lysine into polyurea[32] and polysulfone,[25] alanine derivatives[30] and arginine[20] into polysulfones. Hollow fibers of polysulfone, polyvinylidene fluoride[15] or propylene[13] have been incorporated with tartaric acid or transition metal complexes with a chiral ligand as active chiral sites to form composite membranes. Others have taken inspiration from living systems and prepared membranes from cellulose,[19] nitrocellulose,[22] marine polymers,[24] polypeptides[36] and immobilized DNA.[1,34] Hu and Jiang[39] uniquely demonstrated enantioselective transport using a protein crystal while Sueyoshi and colleagues[21] prepared bionanoporous membranes from chicken feathers and egg shells, taking advantage of the collective chiral environment arising from *L*-amino acids in proteins. Inorganic membranes composed of chirally imprinted mesoporous silica[18] and zeolites with chiral structures[40] have also been assessed for their potential in chiral separation processes. Despite the diversity in the choice of components, very few materials have been established as standard systems for chiral separation, much less for industrial use.[24] There is an obvious need for novel, intelligent designs of membranes and while the most important factor appears to be the nature of the chiral selector,[41] optimization requires a system that allows manipulation of chiral selector (structure and density) among other variables that could affect membrane performance such as solvent polarity and solute concentration.

We have decided to use silica colloidal crystals as a platform to address the challenges described above. The introduction of chiral moieties into nanoporous inorganic solids results in new types of advanced functional composites with potential for chiral sensing and separation, stereospecific catalysis and photonics.[18] Silica colloidal crystals are easily prepared by the self-assembly of silica nanoparticles from solution and the resulting materials possess features that allow manipulation of the two key factors for chiral membranes, namely, porosity and chirality.

The close packing of spheres into a face-centered cubic (*fcc*) lattice creates ordered arrays of interconnected 3D nanopores whose sizes are tunable depending on the nanoparticle diameter. Silica colloidal crystal membranes are characterized by large surface area and pores of uniform size. The facile surface chemistry of silica allows for covalent tethering of almost any moiety ranging from small molecules to polymers and biomolecules. This chapter will describe the preparation and characterization of free-standing silica membranes (nanofrits) whose surfaces have been modified with chiral entities such as amino acid derivatives, thiacalixarene and poly(*L*-alanine). Using absorbance measurements to monitor diffusion through these membranes, we investigated the effect of chiral selector structure and pore size on chiral permselectivity of the nanopores.

Experimental Section

Materials

Chemicals. Ammonium hydroxide (28-30% as NH_3, EMD Chemicals, Inc.), tetrabutylammonium hydroxide (40% wt solution in water, Sigma-Aldrich), *N*,*N*-diisopropylethylamine (99%, Sigma-Aldrich), triethylamine (≥99.5%, Sigma-Aldrich), hydroxylamine hydrochloride (Sigma-Aldrich), sodium hydroxide (Macron Chemicals), sodium bicarbonate (Mallinckrodt Chemicals), magnesium sulfate anhydrous (Mallinckrodt Chemicals), tetrachloroaurate(III) trihydrate (Acrōs Organics), sodium citrate dihydrate (Alfa Aesar), sodium borohydride (Aldrich), copper(I) chloride (99.995+%, Sigma-Aldrich), *L*-cysteine (Aldrich), ferrocenecarboxaldehyde (98%, Aldrich), (*R*)-(+)- α-methylbenzylamine (98%, Aldrich), (*S*)-(-)- α-methylbenzylamine (98%, Aldrich), *N*-α-methyl-*D*-valine hydrochloride (H-*D*-MeVal-OH, Novabiochem), (*R*)-(-)-2-phenylglycine (99%, Aldrich), *N*-(3-aminopropyl)methacrylamide hydrochloride (Polysciences, Inc.), benzoyl chloride (99%, Aldrich), 3,5-dinitrobenzoyl chloride (98+%, Aldrich), EEDQ (99+%, Aldrich), thionyl chloride (97%, Sigma-Aldrich),

tetraethylorthosilicate (99.999+%, Alfa Aesar), 3-aminopropyltriethoxysilane (99%, Aldrich), ((chloromethyl)phenylethyl)-trimethoxysilane (Gelest, Inc.), nitric acid (68-70%, ACS-grade, EMD Chemicals, Inc.), xylene (ACS, Fisher Scientific), ethanol (200 proof, ACS-grade, Pharmaco-Aaper), methanol (ACS Reagent, Sigma-Aldrich), dichloromethane (≥99.5%, Sigma-Aldrich), anhydrous *N*,*N*-dimethylformamide (extra dry, Acrōs Organics), ether (VWR International), hexanes (Mallinckrodt Chemicals), toluene (Mallinckrodt Chemicals), and acetone (Fisher Scientific) were all used as received. Millipore water (18 MΩ•cm) used in all experiments was obtained from a Barnstead "E-pure" water purification system. Acetonitrile (HPLC grade, VWR Scientific) and chloroform were freshly distilled from calcium hydride. Tetrahydrofuran (Mallinckrodt Chemicals) was freshly distilled from sodium/benzophenone.

Instrumentation. Scanning electron microscopy (SEM) images were obtained using either a Hitachi S3000-N or an FEI NanoNova instrument. Transmission electron microscopy (TEM) images were obtained using an FEI Philips Tecnai T-12 instrument. UV/Vis measurements were collected using an Ocean Optics USB2000 or USB4000 instrument. A Branson 1510 sonicator was used for all sonications. A Clay Adams Compact II Centrifuge (3200 rpm, Becton Dickinson) and ultracentrifuge Sorvall RC5B Plus (15000 rpm on a SA-600 rotor) were used for all centrifugations. A Fisher Scientific Isotemp Programmable Muffle Furnace (Model 650) was used for all sintering purposes. A Carver Laboratory Press (Model C) was used for the preparation of all colloidal glass membranes. All zeta-potential measurements were carried out in water using a NICOMP 380 ZLS Zeta Potential/Particle Sizer (PSS•NICOMP Particle Sizing Systems). Thermogravimetric analyses were performed using a TA Instruments TGA 2950 Thermogravimetric Analyzer.

Methods

Preparation of 220 nm silica spheres. All silica spheres were prepared according to modifications of previously reported procedures.[42,43] All glassware was cleaned with Millipore

water prior to use. A batch of silica spheres was made by mixing 500.0 mL of an ethanolic solution containing TEOS (51.4 mL, 0.20 mol) with 500.0 mL of an ethanolic solution containing NH_4OH (26.8 mL, 0.40 mol) and water (288 g, 16.0 mol). These two solutions were poured simultaneously in a 2 L Erlenmeyer flask and vigorously stirred. The resulting mixture had final concentrations of 0.2 M TEOS, 0.4 M NH_3 and 16.0 M H_2O. The onset of turbidity after a short while indicated the start of silica sphere formation. After 24 h, the mixture was then poured into 15 mL centrifuge tubes (Corning) and centrifuged for 10 min. The supernatant was discarded, leaving the spheres as pellets at the bottom of the centrifuge tubes. Purification of the spheres was achieved by a repetitive cycle of suspending the spheres via sonication for 10 min followed by centrifugation for 10 min in a gradient series of 10 mL supernatant: 100% water, 25% ethanol, 50% ethanol, 75% ethanol (twice) and 100% ethanol. After the final rinsing, the supernatant was decanted and the silica spheres air-dried overnight. The dried spheres were then preshrunk by transferring to a Petri dish (breaking any large aggregates with a spatula) and placing in a furnace programmed to heat the spheres for 4 h at 600°C[44-46] (desired temperature achieved at a heating rate of 20°C/min). SEM images of the spheres were taken and the sizes were determined from 100 individually measured spheres in each sample to be 230 ± 20 and 220 ± 20 nm in diameter before and after preshrinking, respectively (Table 3.1).

Preparation of 350 nm silica spheres. A batch of larger size silica spheres was also prepared and preshrunk using a modification of the procedure above. The final concentrations of the reagents were 0.2 M TEOS (51.4 mL, 0.20 mol), 1.1 M NH_3 (70.0 mL, 1.1 mol) and 17.0 M H_2O (257 g, 14.3 mol) in an ethanolic reaction solution of total volume of 1.0 L. The reaction mixture was stirred vigorously overnight at room temperature. SEM images of the spheres were taken and the diameter determined from 100 individually measured silica spheres to be 350 ± 20 nm after preshrinking (Table 3.1).

Preparation of 70 nm silica spheres. A batch of smaller size silica spheres was also prepared according to literature.[47] Briefly, a mixture of 24.2 mL NH_4OH (0.40 mol) and 456.0

mL absolute ethanol was added to 15.2 mL TEOS (0.06 mol) in a 1-L Erlenmeyer flask. The final concentrations of the reagents were 0.12 M TEOS and 0.8 M NH_3 in a reaction solution of total volume of 0.5 L. The reaction mixture was stirred vigorously overnight at room temperature. The spheres were collected and washed by ultracentrifugation for 20 min at 4°C using a gradient series of 100% water, 50% ethanol and absolute ethanol (twice). SEM images of the spheres were taken and the diameter determined from 100 individually measured silica spheres to be 70 ± 7 nm after preshrinking (Table 3.1).

Preparation of free-standing colloidal crystal membranes. Ordered nanofrits were prepared by vertical deposition onto a glass substrate of ~12 wt% colloidal solutions of pre-

Table 3.1. Summary of preparation conditions and sizes of silica spheres.

	Measured diameter, nm	
	DLS	SEM
[TEOS] = 0.2 M, [NH_3] = 0.4 M, [H_2O] = 16.0 M, 25 °C for 24 h		
As made	224 ± 20	227 ± 20
Preshrunk	213 ± 20	223 ± 20
Sintered		160 ± 10
[TEOS] = 0.2 M, [NH_3] = 1.1 M, [H_2O] = 17.0 M, 25 °C for 24 h		
As made	388 ± 30	
Preshrunk	360 ± 30	346 ± 20
Sintered		252 ± 10
[TEOS] = 0.12 M, [NH_3] = 0.8 M, [H_2O] = 1.74 M, 25 °C for 18 h		
As made	66 ± 10	69 ± 7
Preshrunk	57 ± 8	69 ± 7
Sintered		

shrunk silica spheres in ethanol. The resulting membranes were then gently lifted from the substrate and sintered in a furnace for 12 h at 1050°C.[44-46] The sintered silica colloidal membranes were noticeably more robust and durable, making handling easier. SEM images of these nanofrits were taken to give average diameters of 160 ± 10 nm and 250 ± 10 nm for the first and second silica samples respectively in the order of description above, as measured from 100 individual spheres in each colloidal membrane (Table 3.1). The thickness of each colloidal membrane was measured with a Vernier caliper at six different points throughout the piece. To make frits, the pieces were then sandwiched between two PTFE washers (5.0 mm inner diameter, 14.0 mm outer diameter and 1.0 mm thickness, Small Parts, Inc.) with Loctite Hysol 0151 Epoxy. Nanofrits constructed as such were allowed to cure for at least 24 h prior to use for diffusion experiments.

Preparation of free-standing colloidal glass membranes. Pressed frits were prepared in a hydraulic press by applying 7500 psi to loose, dry silica spheres contained in a die set with inner diameter of 12.0 mm. The resulting materials were then sintered and made into the membranes as outlined above.

Surface modification with 3-aminopropyltriethoxysilane. Silica samples immersed in 30 mL dry acetonitrile were surface-modified by addition of 0.20 mL of 3-aminopropyltriethoxysilane with stirring for 18 h under N_2 (g). The substrates were collected and washed with acetonitrile, tetrahydrofuran, xylene, twice with water and finally twice with acetonitrile, followed by air-drying.

Prior to performing this procedure on the sintered colloidal membranes, hydroxyl groups were reintroduced onto the surfaces by immersing the pieces in an aqueous pH 9.5 solution of tetrabutylammonium hydroxide (in a polyethylene bottle) maintained at 60°C for 24 h in an oil bath.[44] The rehydroxylated pieces were then washed with Millipore water, 1 M nitric acid, methanol, Millipore water and acetonitrile consecutively.

Synthesis of (*R*)-2-benzoylamino-3-methylbutyric acid (1). A mixture of *N*-α-methyl-*D*-valine hydrochloride (1.2418 g, 7.4 mmol) and benzoyl chloride (0.820 mL, 7.0 mmol) was stirred for 5min in 50 mL dry CH_2Cl_2. After the addition of *N*,*N*-diisopropylethylamine (1.20 mL, 7.0 mmol), the reaction was stirred for another 24 h at room temperature. The resulting pink solution was reduced to dryness followed by dissolution in 30 mL 1 M NaOH. The aqueous solution was extracted with three portions of 200 mL ether. The organic layer was evaporated to yield the crude product which was then purified via flash chromatography using a 50:50 ethyl acetate:hexane as mobile phase. The enantiopure product was obtained as a yellow solid (average 84.3% yield) whose ^{1}H NMR spectrum is in good agreement with that of previous reports.[48]

Surface-modification with compound 1. Chiral molecule **1** was tethered onto the surfaces of aminated silica using a modification of literature.[48] Briefly, 0.070 mmol of amines (aminated silica) was immersed in dry tetrahydrofuran followed by the addition of equimolar amounts of **1** (0.070 mmol) and *N*-ethoxycarbonyl-2-ethoxy-1,2-dihydroquinoline (EEDQ) (0.070 mmol) such that all species were 0.0645 M in solution. After 24 h at room temperature, the silica were collected and rinsed with two 50 mL portions each of THF, CH_2Cl_2, water and acetonitrile. This chiral modification was performed twice. The air-dried membranes were made into nanofrits as previously described.

Synthesis of (*R*)-(3,5-dinitrobenzoylamino)-phenylacetic acid (2). Compound **2** was prepared following a published procedure.[49] A stoichiometric mixture of (*R*)-(-)-2-phenylglycine (0.8784 g, 5.75 mmol) and 3,5-dinitrobenzoyl chloride (1.301 g, 5.50 mmol) in 15 mL tetrahydrofuran was stirred for 1 week at room temperature. The resulting cream-colored mixture was evaporated followed by dissolution in 25 mL 5% aqueous $NaHCO_3$. The solution was acidified to pH 5 and extracted with two portions of 50 mL ether. The organic layer was dried over anhydrous $MgSO_4$ and evaporated to yield a cream-colored solid (average 17.7% yield) whose ^{1}H NMR spectrum was identical to literature report.

Surface-modification with compound 2.[i] Chiral molecule **2** was installed onto the surfaces of aminated silica as described for compound **1**. The air-dried membranes were then made into nanofrits in the same manner above.

Synthesis of (*R*)-*N*-(2-(3-methacrylamidopropylamino)-2-oxo-1-phenylethyl)-3,5-dinitrobenzamide (3). Compound **2** was converted into a monomer stuitable for atom transfer radical polymerization (ATRP) as follows. Compound **2** (0.3358 g, 1.0 mmol) and EEDQ (0.2436 g, 1.0 mmol) were co-dissolved in 5.50 mL DMF to give a brown mixture. In a separate flask, *N*-(3-aminopropyl)methacrylamide hydrochloride (0.1739 g, 1.0 mmol) was dissolved in 2.00 mL DMF containing *N*,*N*-diisopropylethylamine (0.33 mL, 2.0 mmol). The two mixtures were combined to give a darker brown solution which was stirred for 20 h at room temperature. The solvent was removed *in vacuo* to give the crude product as brown oil. The final product was obtained as a viscous oil (average 58.2% yield) from flash chromatography (75:25 ethyl acetate:hexanes). ^{1}H NMR (300 MHz, $CDCl_3$): δ 9.13 (s, 1 H), 9.12 (s, 1 H), 8.88 (s, 1 H), 8.23 (d, 1 H), 8.18 (d, 1 H), 7.95 (s, 1 H), 7.73 (t, 1 H), 7.56 – 7.27 (m, 3 H), 5.74 (d, 1 H), 5.68 (s, 1 H), 5.28 (s, 1 H), 2.92 (s, 2 H), 2.85 (s, 2 H), 1.89 (s, 2 H).

Surface modification with ATRP initiator. Silica substrates (loose spheres and rehydroxylated membranes) immersed in 30 mL toluene were surface-modified by addition of 0.40 mL of ((chloromethyl)phenylethyl)-trimethoxysilane with stirring at 70°C for 18 h under N_2 (g). The substrates were collected and washed with 100 mL each of toluene, methanol, CH_2Cl_2 and toluene, followed by air-drying. The process was repeated for the membranes.

Surface-initiated ATRP of compound 3. The initiator-modified silica samples were immersed in 8.0 mL DMF solution of monomer **3** (0.469 g, 1.0 mmol). In a separate flask, CuCl (0.9 mg, 0.009 mmol) was added to Me_6TREN (0.08 mL, 0.03 mmol) in 2.0 mL DMF to give a green-colored solution. All mixtures were subjected to four freeze/pump/thaw cycles followed by

[i] Prepared by Julie Cichelli, University of Utah

equilibrating at 70 °C prior to mixing. The two mixtures were combined and the polymerization was carried out at 70 °C to give pale, beige-colored substrates. The polymerization time was varied from 5 to 40 min for the loose spheres and from 20 to 40 min for the ordered membranes. The reaction was quenched by rinsing with 100 mL portions of methanol (twice), water (twice) and acetone. The air-dried membranes were then made into nanofrits in the same manner above.

Surface modification with thiacalix[4]arene. The thiacalix[4]arene[ii] **4** (0.0384 g, 0.03 mmol) was activated for surface-tethering by addition of thionyl chloride (0.655 mL, 27 mmol). The resulting deep orange mixture was refluxed for 1 h followed by solvent removal under vacuum. The activated thiacalix[4]arene **5** was dissolved in 2.0 mL dry THF and added to aminated silica (0.3449, 0.1 mmol amines) immersed in 3.0 mL dry THF that has been bubbled with N_2 (g) for 30 min prior. The resulting mixture was kept in an inert atmosphere and stirred for 20 h at room temperature. The surface-modified samples were rinsed twice with 100 mL portions each of THF and CH_2Cl_2. The air-dried membranes were then made into nanofrits in the same manner above.

Surface modification with poly(*L*-alanine).[iii] The monomer *L*-alanine *N*-carboxyanhydride **6** was prepared following a known method.[50] A 25 mL CH_2Cl_2 solution of *N*-*tert*-butyloxycarbonyl alanine (0.95 g, 5.0 mmol) under N_2 (g) was cooled to 0°C in an ice bath. The reaction mixture was kept at 0°C and stirred for 4 h after addition of PCl_3 (0.524 mL, 6.0 mmol). The solvent was removed in vacuo and the residue was rinsed thrice with 20 mL CCl_4 to yield **6**. Graft polymerization was carried out onto aminated silica samples which have been pre-soaked in DMF for 6 h prior. Compound **6** (0.01 g, 0.09 mmol) was dissolved in 20 mL DMF containing the aminated silica. The polymerization time was varied from 5 to 60min and the polymer-modified substrates were washed twice with 100 mL water. The air-dried membranes were then made into nanofrits in the same manner above.

[ii] Prepared by Arkady Zhukov, Kazan State University
[iii] Prepared by Alexis Abelow, University of Utah

Preparation of 3 nm Au nanoparticles. Gold nanoparticles of nominal size 3nm were prepared according to literature.[51] Briefly, 90.0 mL of a 0.27 mM $HAuCl_4 \bullet 3H_2O$ aqueous solution was mixed with 2.0 mL 1% sodium citrate aqueous solution with stirring. After a

, 1.0 mL of freshly prepared 0.075% $NaBH_4$ in 1% sodium citrate solution was added and the mixture stirred for another 5 min. The reaction temperature was maintained constant at 4°C. This stock solution of Au nanoparticles was then stored in the refrigerator. TEM images indicated that the nanoparticles were prone to aggregation, leading to particles with sizes ranging from about 8 to 40 nm in diameter.

Preparation of Au-coated silica spheres. To form Au-coated silica spheres, the 350nm aminated particles were poured into a 250-mL Erlenmeyer flask, to which then 200 mL of a Au-plating solution (0.1% w/w $HAuCl_4$ in 0.40 mM $NH_2OH \bullet HCl$) was added with vigorous stirring for 30 min. The colloidal solution turned into a deep purple color as Au shells were chemically deposited onto the surface of the silica spheres. The Au-coated spheres were collected in 15-mL Corning tubes, centrifuged and rinsed repetitively with deionized water at least five times. The modified spheres were dried under a stream of N_2 (g) to give a violet-colored powder. TEM images confirmed the formation of a Au coat of uniform thickness and relatively smooth surface around the silica spheres. The thickness of the Au shell was estimated to be ca. 20 nm based on comparison of SEM images of aminated and Au-coated particles.

Preparation of free-standing Au-coated colloidal crystal membranes. The nanofrits were prepared as described for preshrunk silica spheres, with some slight modifications. The resulting membranes were sintered in a furnace for 10 h at 1000°C (desired temperature achieved at a heating rate of 5°C/min). SEM images of the nanofrits were taken to give an average diameter of 340 ± 10 nm as measured from 100 individual spheres in each colloidal membrane.

Surface modification with *L*-cysteine. *L*-cysteine chemisorption onto the Au surface was achieved according to literature.[52] Briefly, sintered membranes of Au-coated silica spheres

were immersed in a 2 mM solution of *L*-cysteine in 80% ethanol for 24 h with gentle stirring in an inert atmosphere. The membranes were then rinsed with ethanol and dried in air prior to nanofrit production.

Syntheses of ferrocen-2-yl methyl-(1-phenyl-ethyl)-amine (7*R* and 7*S*). The chiral probes **7*R*** and **7*S*** were prepared according to literature.[53] Ferrocenecarboxaldehyde (1.07 g, 5.0 mmol) was dissolved in 70 ml dry $CHCl_3$ containing either *R* or *S* enantiomers of α-methylbenzylamine (0.64 mL, 5.0 mmol) and NEt_3 (0.70 mL, 5.0 mmol). The mixture was refluxed for 3h under N_2 (g). The solvent was removed in vacuo to give the intermediate imine as a red-orange solid, which was then dissolved in 50 mL methanol maintained at 0°C using an ice bath. $NaBH_4$ (0.7692 g, 20 mmol) was gradually added to the mixture. After stirring for 30 min, 50 mL 1 M NaOH was added to the reduced solution followed by extraction with three 100 mL portions of $CHCl_3$. The organic layer was evaporated to afford the enantiopure **7*R*** or **7*S*** as a viscous dark brown oil (average 92 to 100% yield) whose ^{1}H NMR spectra matched published reports.

Diffusion measurements through nanofrits. Diffusion experiments through the colloidal membranes were performed by placing a nanofrit between two connected 1-cm quartz cuvettes. The feed cell contained 4.0 mL acetonitrile solution of 50 mM **7*R*** or **7*S*** while the reservoir cell contained 4.0 mL acetonitrile. The nanofrit was placed between two Kalrez o-rings to guard against leaking, and the whole assembly was then secured with a clamp. Each cell was covered with Parafilm to minimize evaporation, and the contents of both cells continually stirred. The reservoir cell was placed between two fiber optic cables and was initially blanked. The flux was monitored by recording the absorbance at 441 nm in the reservoir cell for at least 4 h. Data points were acquired every 150 s with an initial delay of 150 s. Prior to using a nanofrit for a new trial, the pieces were immersed in fresh acetonitrile for at least two days and the solvent replaced

occasionally to ensure removal of any previous probe molecule from within the colloidal membrane.

Results and Discussion

Preparation of free-standing membranes

Silica colloidal crystals were prepared by vertical deposition and subsequent sintering resulted in robust, free-standing ordered nanofrits (Figure 3.1) that are relatively defect-free. The molecular transport through such membranes occurs normal to the (111) plane of the *fcc*-packed structure. Diffusing species enter the crystal through the concave triangular openings between adjacent silica spheres. From a geometric consideration, these colloidal nanopores have a 'radius' (defined as the distance from center of the interstitial void projection to the surface of the nearest sphere) that is ca. 15% of the sphere radius.[54] This is different from the distance from the center of the tetrahedral void to the nearest sphere surface, which is 22.5% of the silica sphere radius.[55] Silica colloidal crystal membranes composed of 160 and 250 nm spheres contain nanopores of 12 and 18.75 nm 'radii', respectively.

The preparation of colloidal crystals from sub-100 nm spheres was also attempted but the resulting pieces were of insufficient size for the purpose of creating membranes. Alternatively, the 70 nm silica spheres were packed using a hydraulic press and subsequent sintering resulted in a new type of robust, free-standing nanofrits. Due to the lack of both long- and short-range order that typically accompanies self-assembly, the membranes were amorphous (Figure 3.2) and were labeled as colloidal glass membranes. Because individual spheres were not close-packed, it is difficult to define pore characteristics such as shape, size and distribution. The well-known values of intrinsic colloidal crystal properties, void fraction ε and nanopore tortuousity τ (0.26 and ca. 3, respectively), were not necessarily applicable to colloidal glass membranes. Nanopores within the pressed frits were expected to possess a non-uniform radius and tortuousity, with some

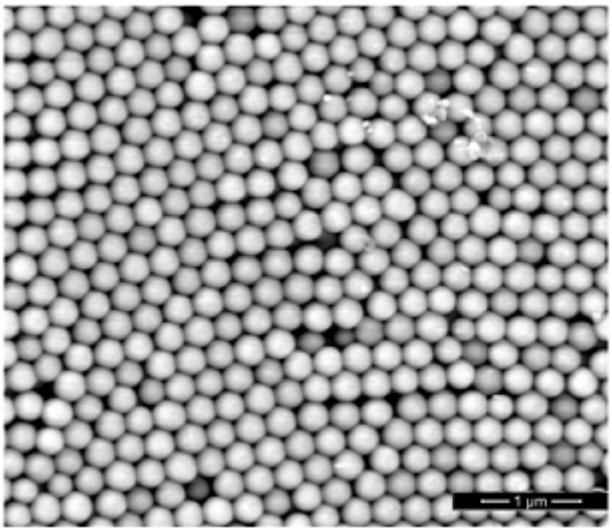

Figure 3.1. SEM image of a sintered colloidal crystal membrane made from 230 nm silica spheres (scale bar = 1000 nm).

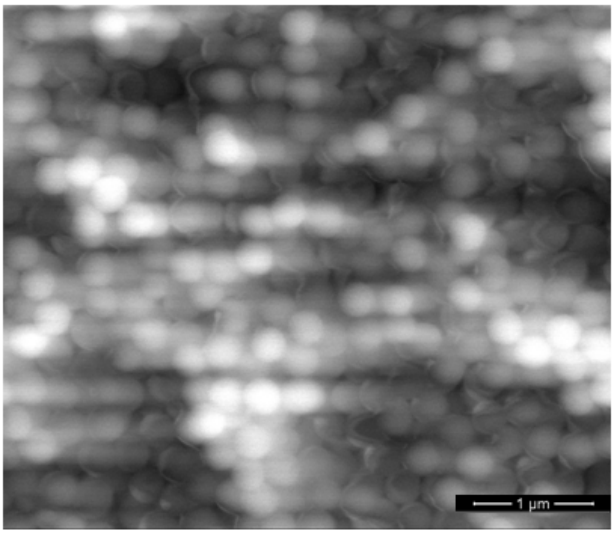

Figure 3.2. SEM image of a sintered colloidal glass membrane made from 230 nm silica spheres (scale bar = 1000 nm).

possibly approaching a linear geometry akin to nanochannels. Overall, higher flux may be expected of colloidal glass membranes compared to the more compact, ordered colloidal crystal membranes prepared from the same-size silica spheres. However, it is possible that with the use of significantly smaller component spheres, the void fraction could nevertheless be reduced to decrease the bulk diffusion through the material.

The molecular flux $J_{colloid}$ (mol·sec^{-1}·cm^{-2}) through the nanofrits can be calculated from a solution of Fick's first law (Equation 3.1):

$$J_{\text{colloid}} = \frac{\Delta C}{L} \times D_{\text{eff}} \tag{3.1}$$

where D_{eff} is the effective diffusion coefficient (cm^2/sec) for a particular species and ΔC is the concentration gradient across the membrane of thickness L. This equation is suitable for dialysis membranes where the concentration gradient is the driving force for mass transfer from regions of high concentration to regions of low concentration.[56] Alternatively, the flux can be determined using Equation 3.2:

$$R_{\text{D}} = J_{\text{colloid}} \times \text{S} \tag{4.2}$$

by measuring the diffusion rate R_D (mol·sec^{-1}) through a nanofrit of known area S (cm^2). In this work, R_D values were obtained by recording the number of moles of the diffusing probe **7** that diffused through the nanofrits as a function of time. Values of D_{eff} were calculated to account for the void fraction and the tortuousity (Equation 3.3):

$$D_{\text{eff}} = \frac{\varepsilon}{\tau} \times D_{\text{sol}} \tag{4.3}$$

where D_{sol} is the diffusion coefficient of the analyte in free solution. All calculations were similarly performed for both ordered and pressed nanofrits, despite the inaccuracy of the equation for the latter. The difference in magnitudes of the D_{eff} values could be used to assess the deviation of nanopore characteristics for colloidal glass membranes from the well-defined ones for ordered close-packed systems.

Surface-modification with small molecules

To determine whether chiral permselective molecular transport could be achieved with the nanofrits, we modified the surfaces of the nanopores with small molecule chiral recognition units **1** and **2** via the facile amide bond formation between amines on the silica surface and the –COOH moieties on the amino acid derivatives (Figures 3.3a, b). To date, numerous works on enantioselective transport concerning amino acids and their derivatives have been reported[10] because these chiral molecules are involved in a wide variety of biological processes and are frequently employed in the synthesis of pharmaceutical intermediates, especially protein-based drugs.[57] Earlier work in our group has demonstrated excellent chiral permselectivities of 4.5 and 2.2 for nanoporous thin films surface-modified with **1** and **2**, respectively, as measured via cyclic voltammetry (CV) for the redox-active chiral probes **7*S*** and **7*R***.[48]

These surface modifications were also carried out in colloidal solution to model the covalent modification of nanopore surfaces within the membranes and to facilitate characterization using colloidal techniques. Comparison of the IR spectra (Figure 3.4) for bare and aminated loose spheres showed the successful coverage of silica surfaces with silamines, evidenced by the appearance of alkane C-H and N-H stretches at 2850 cm^{-1} and ca. 2975 – 2900 cm^{-1}, respectively. The weakened intensity of the N-H stretches in the spectrum of **1**-modified samples indicated the successful coupling of the selector (the resulting amide has an imine resonance structure contribution). These were supported by dynamic light scattering (DLS)

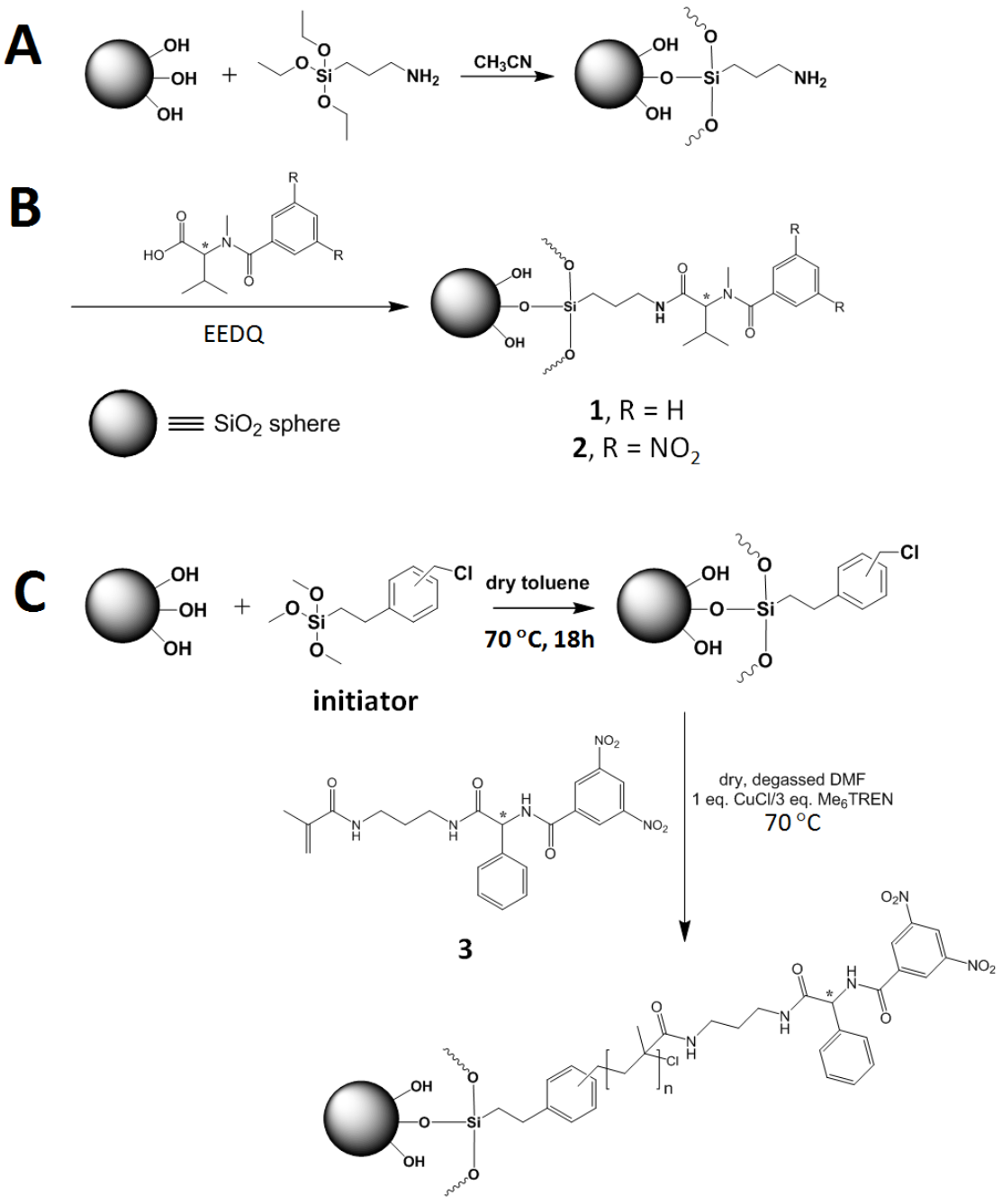

Figure 3.3. Schematic for the surface modifications of silica: (A) amination, (B) installment of small molecule chiral moieties **1** and **2** and (C) polymerization of **3** from a suitable surface-bound initiator, (D) installment of macromolecular chiral moiety **5** and (E) polymerization of **6** from a suitable surface-bound initiator.

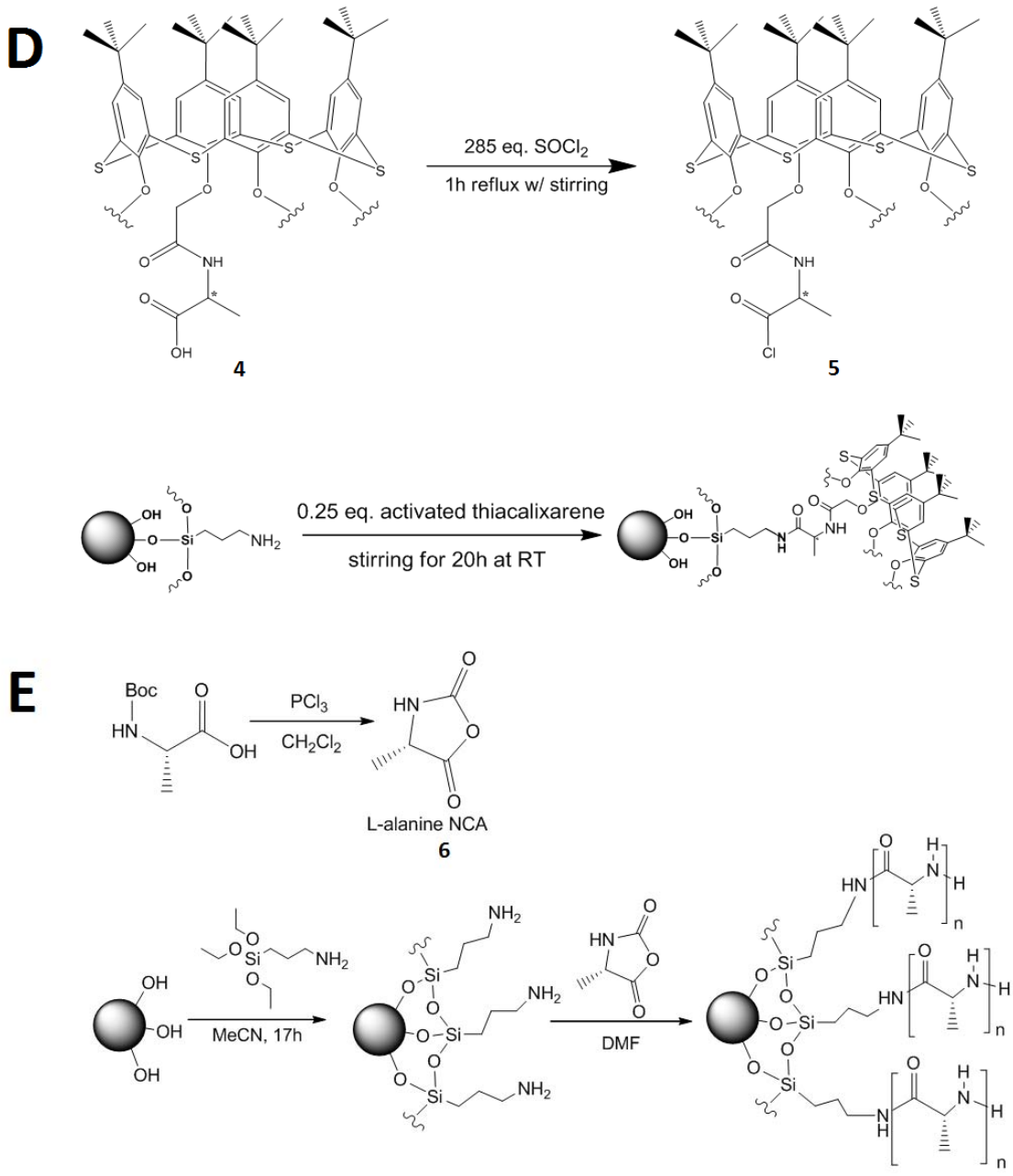

Figure 3.3. Cont.

measurements, which showed an increase in hydrodynamic diameter from 420 ± 60 to 450 ± 80 nm for bare and aminated silica spheres, respectively. As expected of a small-molecule modifier, the diameter remained the same as that of amine-modified spheres. Thermogravimetric analysis (TGA) was employed to quantify the surface coverage with **1**, summarized in Table 3.2, for loose silica spheres. Comparison of derivative TGA curves (Figure 3.5) for aminated and **1**-modified samples showed that % weight loss from 494 to 602 °C may be attributed to the degradation of silamines, while **1** was lost from 227 to 494 °C. Calculated surface densities confirmed the formation of thin polymeric layers of silamines and complete monolayer coverage with **1** (estimated from a maximum of 4 $-NH_2$ groups/nm^2).

Figure 3.6 shows the flux of the chiral probes **7*S*** and **7*R*** through **1**-modified ordered frits of 18.75 nm pore radius. Permselectivity α was calculated as the ratio of the D_{eff} values of enantiomers with faster transport compared to its slower antipode. A calculated permselectivity of 1.31 *S*/*R* revealed that **7*S*** was better transported through **1*R***-modified colloidal crystal membranes. Table 3.3 summarizes the calculated D_{eff} values and it was confirmed that flux became higher through colloidal glass membranes formed from the same-size silica sphere. Comparison of the D_{eff} values showed a two-fold increase in transport rates going from an ordered to a random system. This increase in throughput came at the cost of enantioselectivity as bulk diffusion dominated the transport mechanism. The use of colloidal glass membranes from smaller component spheres (12 nm pore radius) resulted in reduced diffusion rates but was accompanied by a recovery of enantiopermselectivity, which confirmed that minimization of non-enantioselective diffusion was critical for optimal separations. This suggested that these nanofrits were operating based on a diffusion-enantioselective mode wherein the facilitated transport of **7*S*** was attributed to its preferential diastereomeric complexation with **1*R*** albeit with a weak enough binding affinity that enabled the analyte to adsorb and desorb onto and from adjacent chiral recognition sites.

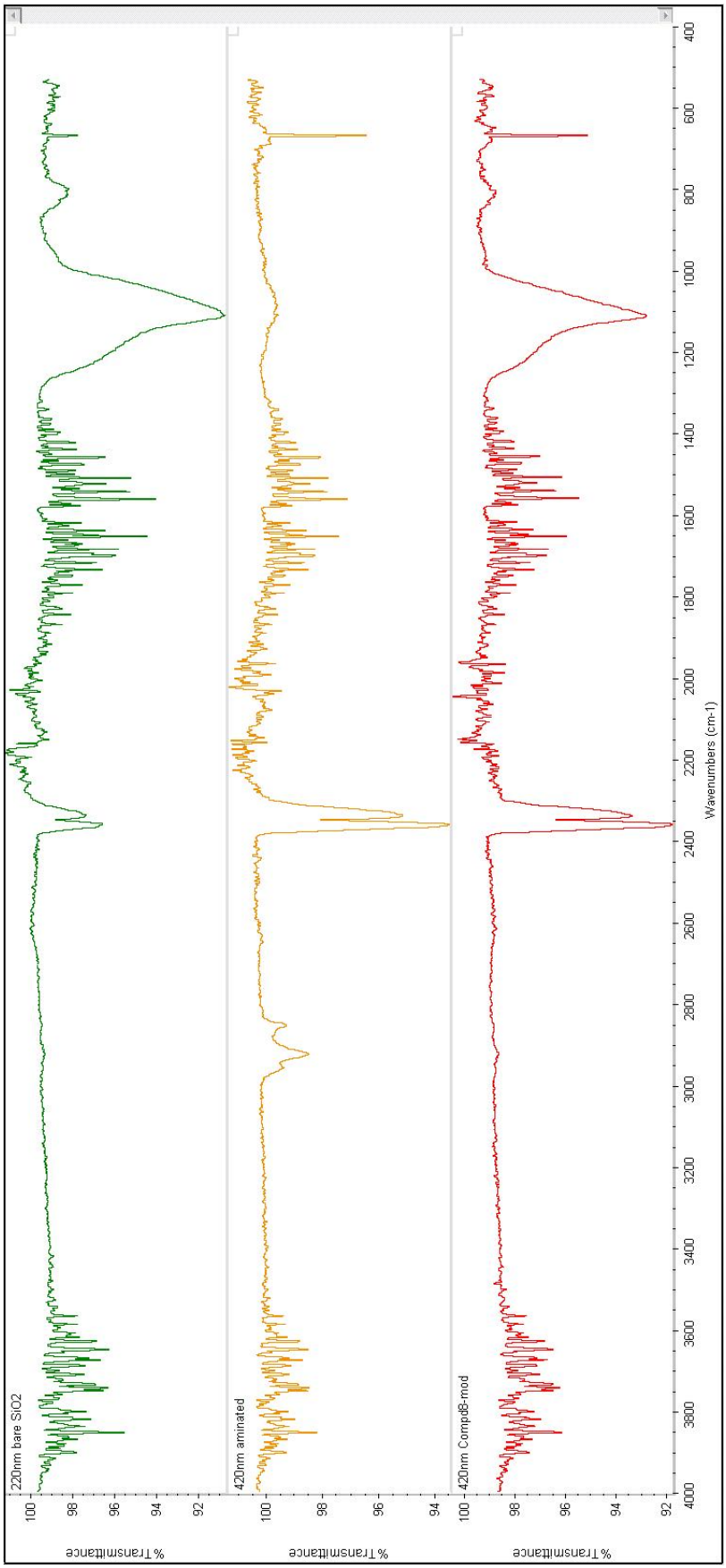

Figure 3.4. Comparison of the IR spectra for (Top) unmodified, (Middle) aminated and (Bottom) **1**-modified silica.

Table 3.2. Summary of TGA results.

Surface modifier	Diameter (nm)	% Weight loss	Surface density (molecule per nm^2)
Silamines	250	1.55% from 498 to 613 °C	28 $–NH_2$ (~6 layers)
1	250	0.99% from 200 to 491 °C	4.1 (monolayer of **1**)
4	70	2.83% from 214 to 385 °C	0.27 compound **4**
		2.31% from 385 to 724 °C	4.9 $–NH_2$ (monolayer)
	250	0.72% from 236 to 439 °C	0.48 compound **4**
		0.73% to 661 °C	11 $–NH_2$ (~3 layers)
Poly(**3**) initiator	250	1.59% from 150 to 800 °C	4.5 (monolayer)
Poly(**3**) 5min	250	1.17% from 95 to 455 °C	1.1 selectors ($n \sim 1$)
Poly(**3**) 20min	250	1.35% from 96 to 453 °C	13 selectors ($n \sim 13$)
Poly(*L*-ala) initiator[a]	160	0.09% from 150 to 600 °C	0.46 $–NH_2$
Poly(*L*-ala) 20min[a]	160	0.99% from 150 to 600 °C	5.7 selectors ($n \sim 12$)

a data for modified nanofrits prepared by Alexis Abelow, University of Utah

Figure 3.7 illustrates the steroespecific interactions between **1*R*** and the *R* and *S* enantiomers of the diffusing chiral probe. In the diastereomeric complex of **1*R*** with **7*S***, the –COOH group on the chiral selector interacted with the phenyl substituent on the chiral C of **7*S*** while the benzoylamino substituent on **1*R*** interacted with the ferrocen-2-yl methylamino group on **7*S***. The latter consisted of π - π interactions between the benzoyl and cyclopentadiene (Cp) rings in addition to a likely H-bond between the amidyl O of **1** and N—H on **7*S***. In contrast, favorable interactions between **1** ***R*** and **7*R*** include a possible H-bond between the –COOH and ferrocenyl N-H, as well as π - π interactions between the benzoyl and phenyl rings.

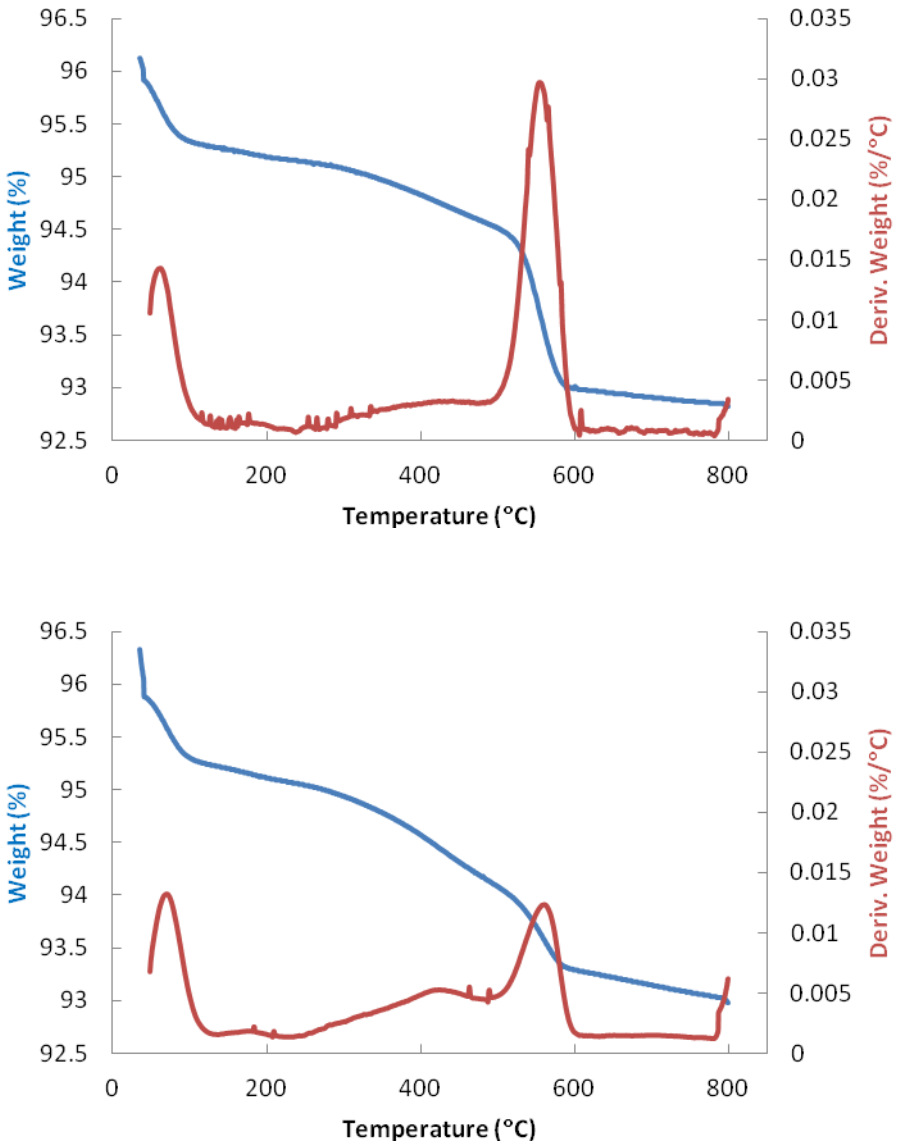

Figure 3.5. Comparison of the TGA curves for (Top) aminated and (Bottom) **1**-modified silica.

Table 3.3. Summary of calculated effective diffusion coefficients and chiral permselectivities through colloidal crystal membranes.

Surface modifier	Pore radius (nm)	D_{eff} ($cm^2/sec \times 10^{-5}$) *S*	*R*	Selectivity
1	18.75	2.3 ± 0.4	1.7 ± 0.2	1.31 ± 0.08 *S*/*R*
1[a]	18.75	4.4 ± 0.6	4.5 ± 0.4	1.0 ± 0.2 *S*/*R*
1[a]	12	1.64 ± 0.01	1.4 ± 0.1	1.2 ± 0.1 *S*/*R*
4	18.75	4 ± 2	3.1 ± 0.2)	1.3 ± 0.1 *S*/*R*
Poly(**3**) 20min	18.75	2.4 ± 0.8	2.3 ± 0.5	1.1 ± 0.1 *S*/*R*
Poly(**3**) 40min	18.75	3.2 ± 0.4	2.4 ± 0.4	1.32 ± 0.04 *S*/*R*
Poly(*L*-ala) 5min	12	2.59 ± 0.03	2.52 ± 0.07	0.97 ± 0.03 *R*/*S*
Poly(*L*-ala) 10min	12	2.8 ± 0.1	2.6 ± 0.1	0.91 ± 0.05 *R*/*S*
Poly(*L*-ala) 30min	12	1.9 ± 0.4	2.2 ± 0.5	1.14 ± 0.05 *R*/*S*
Poly(*L*-ala) 60min	12	0.29 ± 0.06	0.33 ± 0.03	1.1 ± 0.3 *R*/*S*
L-cys on Au	21	2.3 ± 0.4	2.4 ± 0.6	1.0 ± 0.1 *S*/*R*

a Diffusion through colloidal glass membranes

With the use of **2** as chiral selector, the observed *S*/*R* selectivity was enhanced to ca. 1.75.[iv] This suggested that the π - π interactions between the benzoylamino and ferrocen-2-yl methylamino groups in the **1*R***-**7*S*** diastereomeric complex was responsible for the apparent binding preference for **7*S*** over **7*R***. The presence of the electron-withdrawing $-NO_2$ groups can enhance the π-acidity of the benzoyl ring while the proximity of an amino group to the ferrocenyl moiety could favor the π-donor ability of the Cp rings.

[iv] Measured by Julie Cichelli, University of Utah

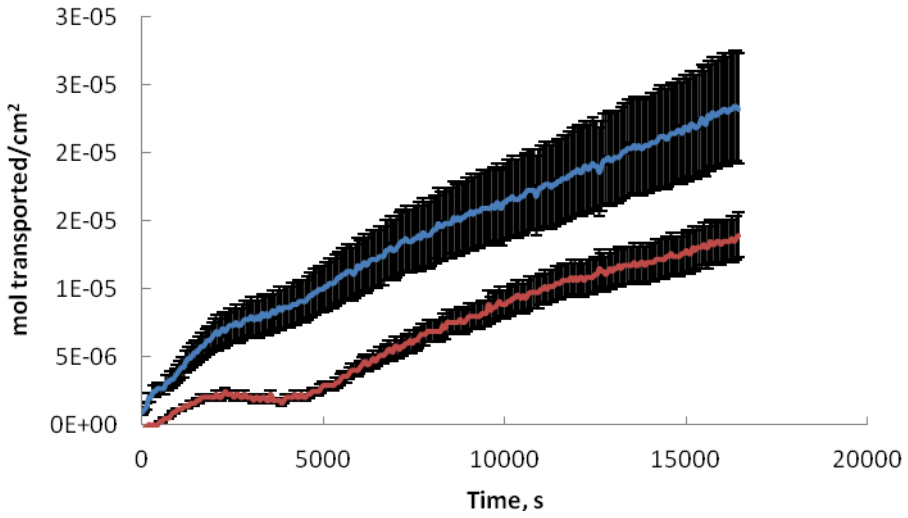

Figure 3.6. Comparison of the flux of **7*S*** (blue) and **7*R*** (red) through **1**-modified ordered frits with 18.75 nm pore 'radius'.

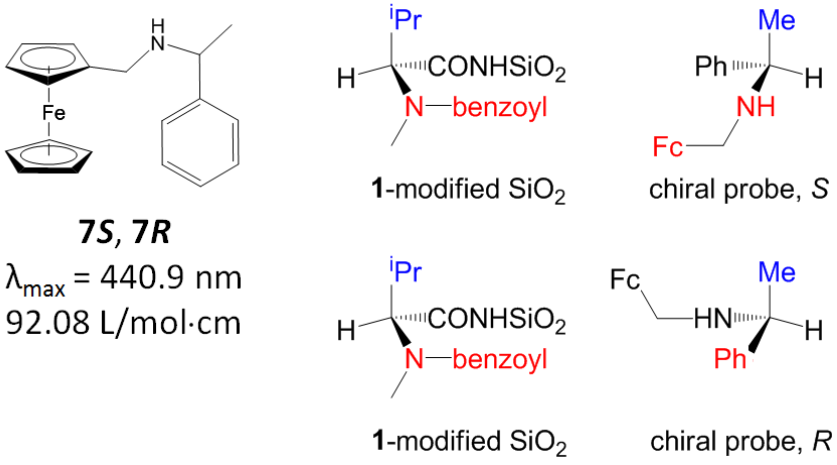

Figure 3.7. Stereospecific interactions between **1** and the diffusing chiral probe **7** included hydrophobic (blue) and π-π (red). The use of **2** (*S*/*R* 1.75) enhanced the π-acid/base interaction in **1**/**7*S*** due to the electron-withdrawing effect of the $-NO_2$ substituent on the benzoyl phenyl.

Overall, comparison of α values to earlier results obtained via CV[48] showed that nanofrits possessed lower chiral recognition abilities. This was attributed to a reduced surface density of chiral modifiers compared to silica surfaces in thin films that were not subjected to thermal sintering. Some surface silanols were irreversibly lost even with rehydroxylation as a result of the condensation of Si-O-Si bonds that fuse neighboring silica spheres at points of contact. Also, in the case of **2*R***-modified frits, the permselectivity was reversed into *S*/*R* compared to an *R*/*S* value of 2.16 for the corresponding thin film. This phenomenon has been commonly reported in literature upon switching from a concentration gradient to an applied potential difference as the driving force for enantioselective mass transfer.[27,32,35]

Surface modification with a thiacalixarene

Calixarenes are well-studied selective receptors for a variety of cations, anions and neutral molecules. In a recent work in our group,[58] we have demonstrated that non-covalent interactions with a charged transition metal complex such as $[Fe(bpy)_3]^{2+}$ resulted in surface-facilitated transport whereas neutral species such as ferrocene(dimethanol) experienced a simple diffusive transport. Sirit and coworkers have thoroughly investigated calixarene derivatives whose lower rims have been functionalized with chiral moieties such as tartaric ester[6] and amino alcohol functionalities[7] such as aminonaphthol units[31] for applications that rely on chiral recognition. The rigidity of the microenvironment of the cavity as well as the nature of the chiral substituents were found to be critical for enantiomeric recognition.[26]

In this work, thiacalix[4]arenes in 'cone' conformation and bearing chiral centers in each of the pendant chains at the bottom rim have been employed as chiral selectors for our nanofrits with the intention of exploiting the host-guest interactions between the surface-bound chiral thiacalixarene and diffusing enantiomers as a basis for chiral permselectivity. Chiral thiacalixarene **4** has methyl alanine components on its lower rim which are capable of non-covalent interactions such as H-bonding in addition to π - π stacking, alkyl - π and other Van der

Waals' forces with its cone. The tethering onto the nanopore surfaces was achieved by conversion of the –COOH groups into acyl chlorides that were reactive with the surface amines (Figure 3.3d). The reaction was monitored by DLS, which showed a decrease in hydrodynamic diameter from 380 ± 60 to 370 ± 70 nm for aminated and **4**-modified loose silica spheres, respectively. This can be explained as the result of poor hydrosolvation around the now hydrophobic surfaces of the modified silica due to the *t*-butyl phenyl groups on the upper rim of the macrocycle. Table 3.2 shows that, according to TGA, the chiral macromolecular selectors are grafted within the nanopores with significantly lower surface densities (ca. 0.5/nm^2) compared to small molecule modifiers. Low surface coverage is commonly observed with large molecules;[58] with increased relative size of the macrocycle compared to the silica sphere, fewer contact points are possible since the steric bulk of the cone would prevent compact packing of the modifier onto the silica surface. Comparison of derivative TGA curves (Figure 3.8) for aminated and **4**-modified samples showed that % weight loss from 236 to 439 °C corresponds to the combustion of thiacalixarenes.

Figure 3.9 compares the flux of **7*S*** and **7*R*** through **4**-modified colloidal crystal membranes of 18.75 nm pore 'radius'. The values of D_{eff} (Table 3.3) demonstrated the chiral recognition ability of the system that allowed for the preferential transport of **7*S*** over **7*R***. The slightly higher D_{eff} values for both **7*S*** and **7*R*** compared to **1**- and **2**-modified membranes could be indicative of weaker interactions between the chiral macrocycle and the diffusing enantiomers. The modest selectivity (1.3) may have been the effect of having bulky *t*-butyl groups on the upper rim of the cavity, which might have hindered access to the chiral environment near the silica surface. The average enantioselectivity for the membranes was slightly lower and opposite to that obtained from CV measurements (*R*/*S* 1.5) for permselective transport through **4**-modified thin films.[59]

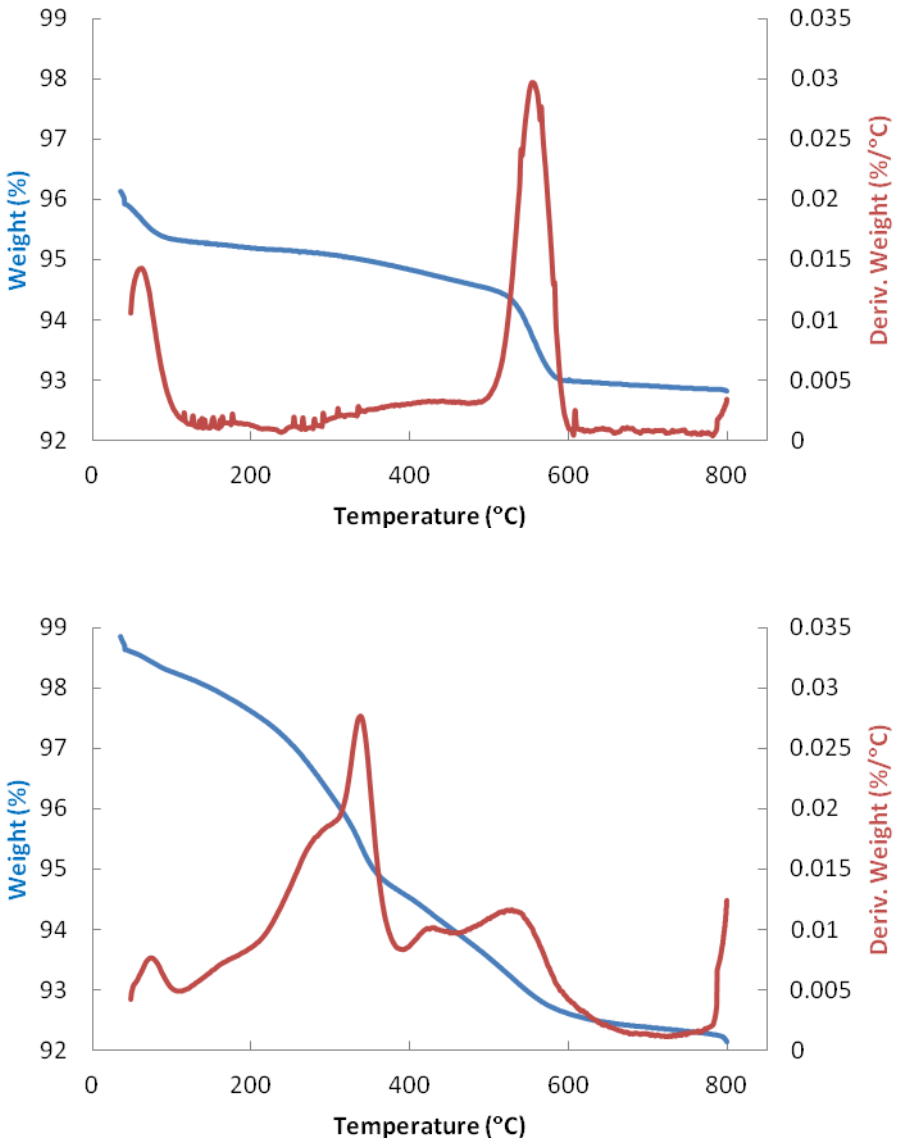

Figure 3.8. Comparison of the TGA curves for (Top) aminated and (Bottom) **4**-modified silica.

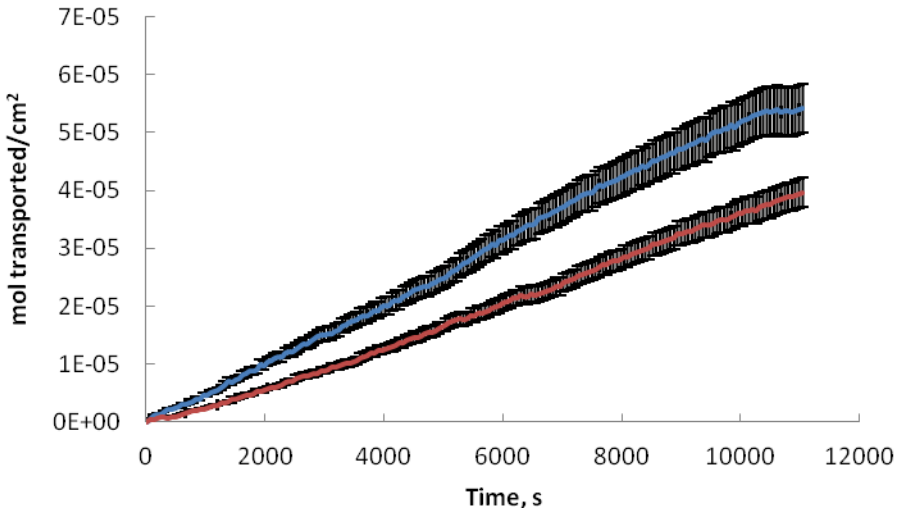

Figure 3.9. Comparison of the flux of **7*S*** (blue) and **7*R*** (red) through **4**-modified ordered frits with 18.75 nm pore 'radius'.

Surface modification with chiral polymers

To enhance the number of chiral recognition sites per unit surface area, polymers bearing chiral centers either on the side chains (**3**, Figure 3.3c) or along the main chain (**6**, Figure 3.3e) have been grown from covalently-bound initiators. Another advantage of polymeric surface-modifiers is that the growth of sufficiently long chains that would occupy the nanopore volume could help minimize nonenantiospecific diffusive transport through the nanopores so as to enhance the efficiency of chiral separation. As with the thiacalixarene, **2** had to be converted into a suitable species prior to polymerization. We took advantage of the well-established polymer chemistry of acrylamides to convert **2** into the polymerizable species **3**.[60,61]

A silane initiator followed by treatment with the monomer in the presence of a copper(I) catalyst. TEM images (Figure 3.10) clearly show the success of the polymerization via the appearance of a uniform organic coating enveloping each individual nanoparticle compared to the

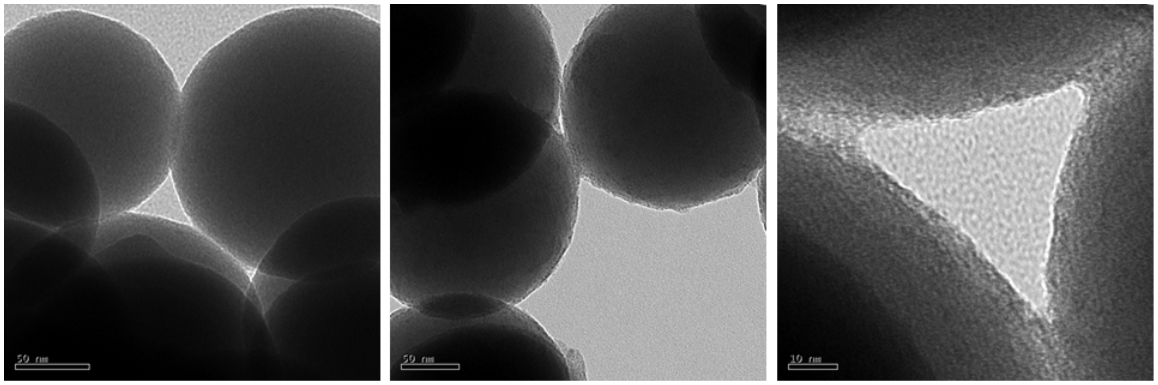

Figure 3.10. TEM images of (Left) unmodified silica (scale bar = 50 nm) and (Middle, Right) poly(**3**)-modified for 40 min (scale bars = 50 and 10 nm, respectively).

noticeably smoother surface of initiator-modified loose spheres. SEM images (Figure 3.11) revealed that the subsequent surface modification with polymer chains perturbed the order of the top layer of the colloidal crystal membrane (nanopore 'radius' 18.75nm). The polymer growth as a function of polymerization time was monitored by DLS and TGA, and the polymer brush length and degree of polymerization *n* were estimated (Tables 3.2 and 3.4). The TGA curves showed increasing % weight loss with increasing ATRP time (Figure 3.12), particularly within 100 to 450 °C where the bulk of the polymer decomposed. Comparison of the derivative TGA curves supported this assignment, while the silane initiator was degraded into inert SiO_2 at higher temperatures with the peak occurring at ca. 500 – 600 °C.

To determine if an increase in the number of available chiral recognition sites per unit surface area would lead to improved enantioseparation efficiencies, we studied the diffusion of the chiral probes **7*S*** and **7*R*** through ordered membranes containing polymers of **3** grown for 20 and 40 min. Figure 3.13 shows the preferential transport of **7*S*** over **7*R***, in agreement with the observed permselectivity for the monomer-modified nanofrit. The obtained *S*/*R* selectivity

increased with doubled polymerization time (Table 3.3); however, the values were modest and were actually lower than those for small molecule-modified membrane. This was consistent with our other findings in an unpublished report[62] wherein the observed permselectivities remained approximately the same for colloidal thin films modified with small-molecule and polymer brush chiral selectors. We believe that enantioselectivity may be an intrinsic transport property that may be best optimized with the careful design of chiral recognition moieties. As with the case of

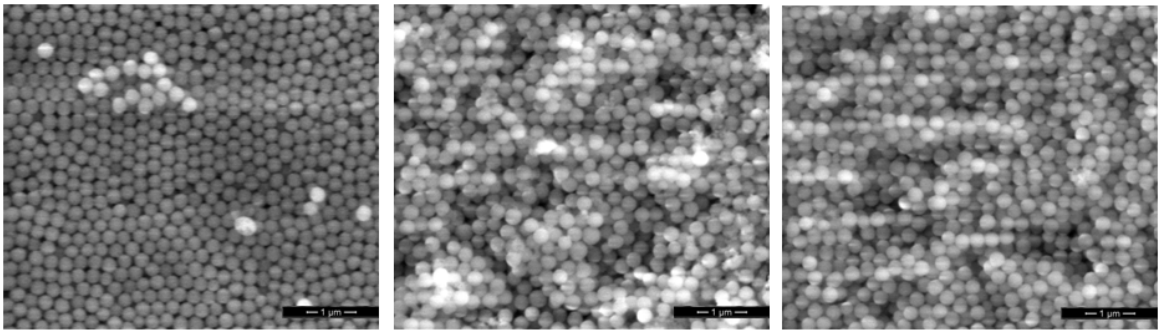

Figure 3.11. SEM images of (Left) initiator-modified and (Middle) poly(3)-modified for 20 min and (Right) 40 min (scale bars = 1000 nm) sintered colloidal crystal membranes.

Table 3.4. Poly(**3**) brush lengths as measured by DLS in acetone.

	Diameter (nm)	**Δr (nm)**
Preshrunk	193 ± 40	(-2)
Initiator-modified	195 ± 40	0
5 min ATRP time	216 ± 40	11
20 min ATRP time	328 ± 60	67
30 min ATRP time	393 ± 90	99
40 min ATRP time	437 ± 80	121

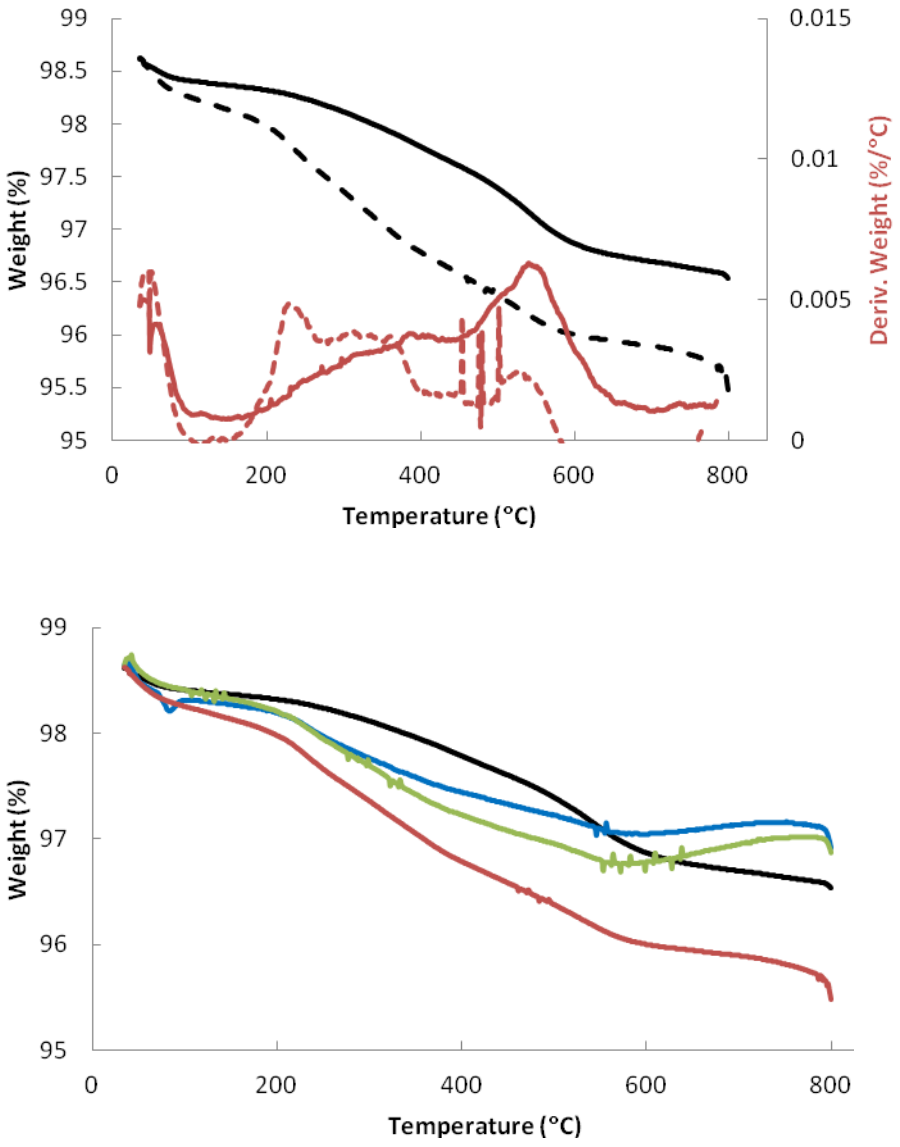

Figure 3.12. Comparison of the TGA curves for (Top) initiator- (solid) and poly(**3**)-modified silica for 40 min (dashed); (Bottom) TGA of initiator-modified (black)silica spheres with poly(**3**) grown from the surface for 10 min (blue), 20 min (green) and 40 min (red).

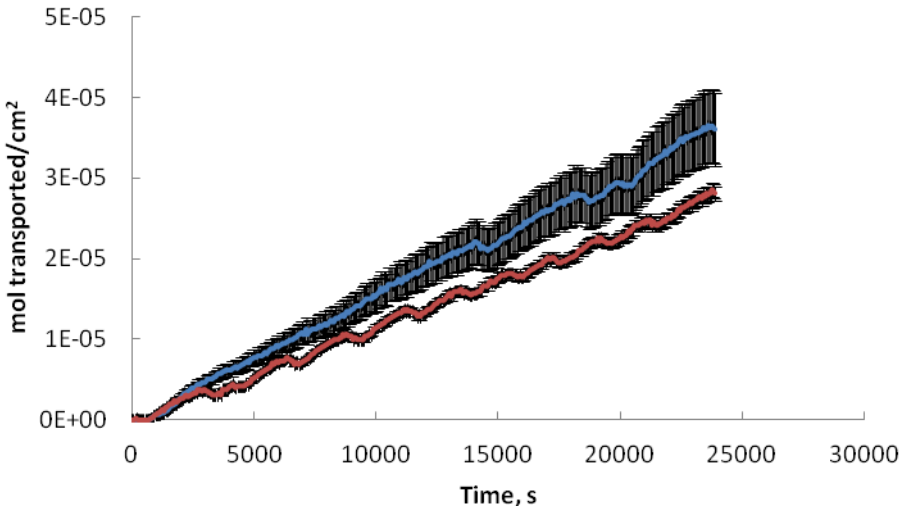

Figure 3.13. Comparison of the flux of 7***S*** (blue) and 7***R*** (red) through poly(**3**)-modified (40 min) ordered frits with 18.75 nm pore 'radius'.

2-modified membranes, the *S*/*R* preference was likewise opposite to an *R*/*S* 2.20 ± 0.40 selectivity obtained via CV analysis for thin films modified with the same chiral brushes.

We also employed polymers of the enantiopure amino acid *L*-alanine as chiral recognition units within nanopores of 'radius' 12 nm (Figures 3.3e, 3.14). Summarized results from TGA (Table 3.2) demonstrate that poly-*L*-alanine chains with n = 12 (similar to chain lengths from monomer **3** grown for the same time) were successfully polymerized within 20 min from the nanopore surfaces with a grafting density of about 0.5/nm^2. Table 3.3 shows the general trend of decreasing D_{eff} values for both enantiomers of the chiral probe **7** with increasing graft polymerization times, indicating the continuous growth of poly-*L*-alanine chains. The inverse relationship between flux and calculated enantiopermselectivities suggested that poly-*L*-alanine-modified colloidal crystal membranes were also operating on a diffusion-enantioselective mode wherein 7***R*** was preferentially transported over 7***S***. The poor selectivities (even for up to an hour

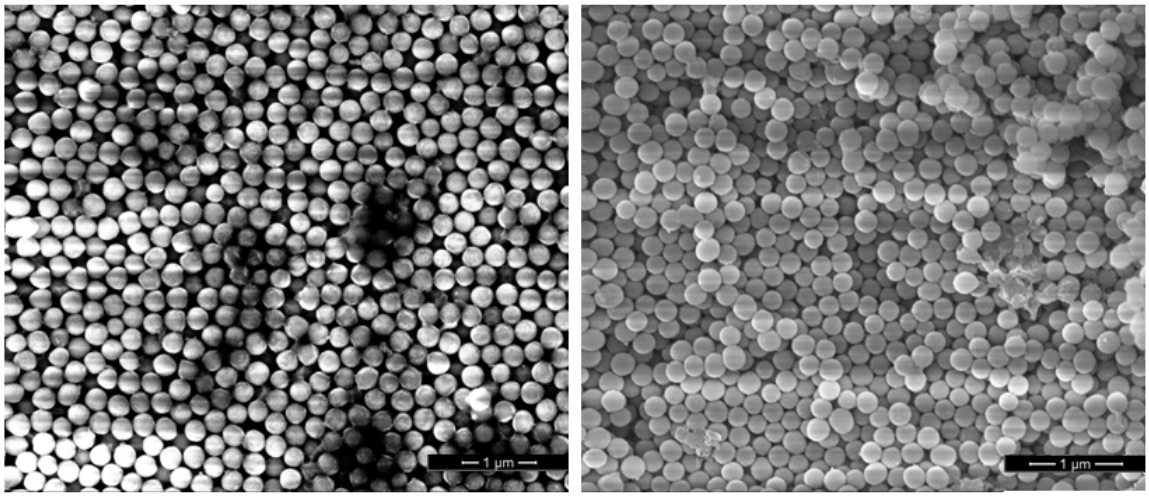

Figure 3.14. SEM images of (Left) aminated sintered silica colloidal crystal membrane with (Right) poly-*L*-alanine grown for 30 min (scale bars = 1000 nm).

of polymerization) emphasized the importance of choosing an optimized structure for the chiral selector. Poly-*L*-alanine does not possess moieties capable of π-π interactions with the diffusing probe **7**, thus explaining the low chiral recognition efficiencies. The little of enantioselectivity that was observed can be attributed to the inherent chirality and H-bonding ability of the polymer. Our previous studies of a similar polymerization on silica nanospheres showed no evidence of α-helical formation for poly-*L*-alanine according to circular dichroism experiments.[50] The *R*/*S* selectivity of 1.13 for the 1 h-modified membranes was opposite to the *S*/*R* permselectivity of 1.5 measured via CV for colloidal thin films grown with poly-*L*-alanine brushes for the same duration.[62]

Surface modification of gold-coated colloidal crystal membranes

In an effort to broaden the scope of this work, we have also prepared free-standing membranes from individually gold-coated silica spheres of diameter 280 ± 10 nm (pore 'radius'

of 21 nm). This system was chosen as an alternative to silica because gold surfaces offer doubled maximum grafting densities (up to 10 thiol modifiers/nm^2) compared to the maximum of 5/nm^2 for silica. In the previous chapter, we demonstrated that coating the silica spheres with a gold shell did not appear to affect the self-assembly from a colloidal solution into an *fcc* lattice. We modified our gold-coated nanopores with a self-assembled thiol monolayer of the enantiopure amino acid *L*-cysteine as chiral selectors (Figure 3.15). Figure 3.16 and calculated D_{eff} values (Table 3.3) for **7*S*** and **7*R*** showed that these membranes have negligible chiral recognition ability for the diffusing probe despite the chirality of the selector and its H-bond formation capabilities. This is most likely the result of both poor quality of *L*-cysteine as a chiral selector, due to the absence of moieties capable of π-π interactions with the diffusing probe **7**.

Conclusions

In this chapter, we have described chiral free-standing nanofrits with ordered (colloidal crystal membrane) or random (colloidal glass membrane) nanopores of different size. We achieved this by the covalent modification of silica surfaces with small molecules such as amino acids, a macrocycle capable of host-guest interactions (specifically a thiacalixarene derivative) and polymer chains of derivatized amino acids. Permselectivity values revealed that diffusion-enantioselectivity is the dominant mode of operation in these membranes, based on facilitated transport (as opposed to retarded transport) of one enantiomer. Comparison of chiral permselectivities obtained through small- vs. polymer-modified membranes showed negligible improvement despite an increase in the number of available chiral recognition sites per unit surface area. This suggests that the chiral selector structure is the most important factor controlling the selectivity, along with nanopore size.

The obtained chiral permselectivity values ranged from ca. 1.2 to 1.75, which put the performance of our composite organic-inorganic membranes on par with most polymer-based solid membranes and bulk liquid membranes reported in the literature.[11] In addition, our system

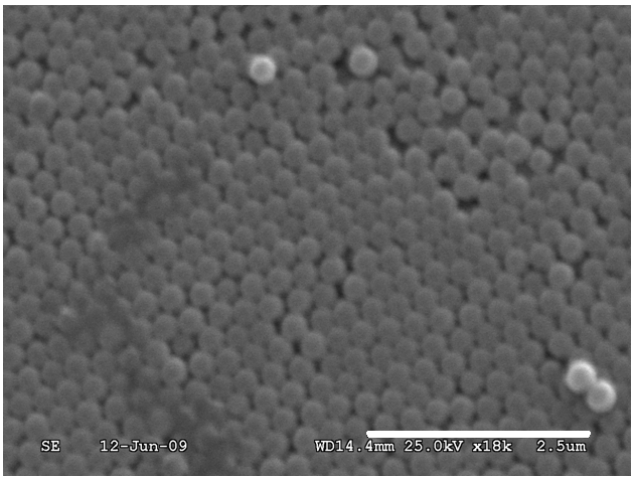

Figure 3.15. SEM image of sintered colloidal crystal membrane composed of gold-coated silica with a surface-bound monolayer of thiol (scale bar = 2500 nm).

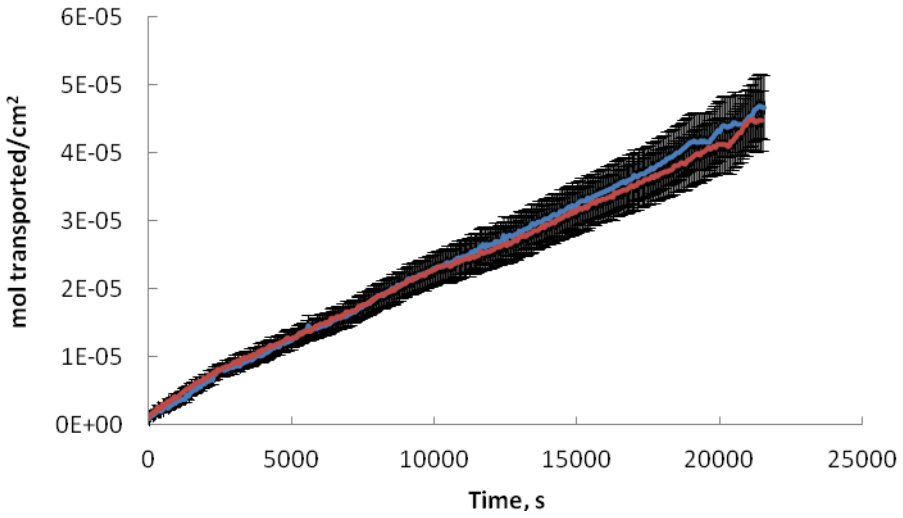

Figure 3.16. Comparison of the flux of **7*S*** (blue) and **7*R*** (red) through *L*-cysteine-modified gold-coated ordered frits with 21 nm pore 'radius'.

offers the advantage of durability and ease of preparation (two problems polymer and bulk liquid membranes). To the best of our knowledge, this is the first example of silica-based free-standing membranes bearing chiral functionalities for direct binding (as opposed to molecular imprinting)[18] of enantiomers for the purpose of semi-preparative-scale chiral separations. To achieve better separations, it would be possible to employ a multi-stage cascade of membranes.[34]

References

(1) Yoshikawa, M.; Maruhashi, M.; Iwamoto, Y.; Ogata, N. *Macromol. Symp.* **2007**, *249-250*, 557.

(2) Du, Y.; Guo, S.; Qin, H.; Dong, S.; Wang, E. *Chem. Commun.* **2012**, *48*, 799.

(3) Wei, W.; Qu, K.; Ren, J.; Qu, X. *Chem. Sci.* **2011**, *2*, 2050.

(4) McConathy, J.; Owens, M.J. *Primary Care Companion J. Clin. Psychiatry* **2003**, *5*, 70.

(5) Ooi, T. *Science* **2011**, *331*, 1395.

(6) Kaiakycuk, A.; Durmaz, M.; Sirit, A.; Yilmaz, M.; Demir, A.S. *Tetrahedron: Assymetry* **2006**, *17*, 1963.

(7) Bozkurt, S.; Yilmaz, M.; Sirit, A. *Chirality* **2012**, *24*, 129.

(8) Higuchi, A.; Tamai, M.; Ko, Y.-A.; Tagawa, Y.-I.; Wu, Y.-H.; Freeman, B.D.; Bing, J.-T.; Chang, Y.; Ling, Q.-D. *Polymer Reviews* **2010**, *50*, 113.

(9) Han, C.; Hou, X.; Zhang, H.; Guo, W.; Li, H.; Jang, L. *J. Am. Chem. Soc.* **2011**, *133*, 7644.

(10) Gou, L.; Robl, S.; Leonhard, K.; Lorenz, H.; Sordo, M.; Butka, A.; Kesselheim, S.; Wolff, M.; Seidel-Morgenstern, A.; Schaber, K. *Chirality* **2011**, *23*, 118.

(11) Xie, R.; Chu, L.-Y.; Deng, J.-G. *Chem. Soc. Rev.* **2008**, *37*, 1243.

(12) Liu, H.-L.; Hou, X.-L.; Pu, L. *Angew. Chem. Int. Ed.* **2009**, *48*, 382.

(13) Sunsandee, N.; Leepipatpiboon, N.; Ramakul, P.; Pancharoen, U. *Chemical Engineering Journal* **2012**, *180*, 299.

(14) Mirčeski, V.; Quentel, F.; L'Her, M. *Electrochemistry Communications* **2009**, *11*, 1262.

(15) Wang, Z.; Cai, C.; Lin, Y.; Bian, Y.; Guo, H.; Chen, X. *Separation and Purification Technology* **2011**, *79*, 63.

(16) Hühnerfuss, H.; Shah, M.R. *Journal of Chromatography A* **2009**, *1216*, 481.

(17) Miyabe, T.; Iida, H.; Ohnishi, A.; Yashima, E. *Chem. Sci.* **2012**, *3*, 863.

(18) Shopsowitz, K.E.; Qi, H.; Hamad, W.Y.; McLachlan, M.J. *Nature* **2010**, *468*, 422.

(19) Ma, C.; Xu, X.-L.; Ai, P.; Xie, S.-M.; Lu, Y.-C.; Shan, H.-Q.; Yuan, L.-M. *Chirality* **2011**, *23*, 379.

(20) Singh, K.; Ingole, P.G.; Bhrambhatt, H.; Bhattachayra, A.; Bajaj, H.C. *Separation and Purification Technology* **2011**, *78*, 138.

(21) Sueyoshi, Y.; Hashimoto, T.; Yoshikawa, M.; Watanabe, K. *Waste Biomass Valor* **2011**, *2*, 303.

(22) Jiang, Y.-D.; Zhang, J.-H.; Xie, S.-M.; Lu, Y.-C.; Zhang, M.; Ma, C.; Yuan, K.-M. *Journal of Applied Polymer Science* **2012**, *124*, 5187.

(23) Huang, D.; Huang, K.; Chen, S.; Liu, S.; Yu, J. *Chem. Biochem. Eng. Q.* **2008**, *22*, 447.

(24) Iwamoto, Y.; Yoshikawa, M.; Yamaoka, K.; Ogata, N. *Desalination and Water Treatment* **2010**, *17*, 268.

(25) Ingole, P.G.; Bajaj, H.C.; Singh, K. *Indian Journal of Chemical Technology* **2011**, *18*, 197.

(26) Aydin, I.; Aral, T.; Karakaplan, M.; Hoşgören, H. *Tetrahedron: Assymetry* **2009**, *20*, 179.

(27) Ikeuchi, Y.; Nakagawa, M.; Yoshikawa, M.; Yoshida, H.; Sakurai, S. *Journal of Polymer Science: Part A: Polymer Chemistry* **2009**, *47*, 2530.

(28) Canepari, S.; Girelli, A.M.; Mattei, E.; Tosti, D. *J. Braz. Chem. Soc.* **2009**, *20*, 429.

(29) Kanyanee, T.; Jakmunee, J.; Grudpan, K.; Dasgupta, P. *J. Am. Chem. Soc.* **2010**, *132*, 18045.

(30) Mizushima, H.; Yoshikawa, M.; Robertson, G.P.; Guiver, M.D. *Macromol. Mater. Eng.* **2011**, *296*, 562.

(31) Durmaz, M.; Bozkurt, S.; Naziroglu, H.N.; Yilmaz, M.; Sirit, A. *Tetrahedron: Assymetry* **2011**, *22*, 791.

(32) Hatanaka, M.; Nishioka, Y.; Yoshikawa, M. *Macromol. Chem. Phys.* **2011**, *212*, 1351.

(33) Nakagawa, H.; Shimizu, K.; Yamada, K.-I. *Chirality* **1999**, *11*, 516.

(34) Higuchi, A.; Higuchi, Y.; Furuta, K.; Yoon, B.O.; Hara, M.; Maniwa, S.; Saitoh, M.; Sanui, K. *Journal of Membrane Science* **2003**, *221*, 207.

(35) Hashimoto, T.; Yoshikawa, M. *Current Nano Science* **2011**, *7*, 915.

(36) Müller, M.; Ouyang, W.; Appelhans, D.; Voit, B. *Polymeric Materials: Science and Engineering* **2008**, *99*, 107.

(37) He, Y.; Chai, X.-J.; Zeng, S. *Journal of Chinese Pharmaceutical Sciences* **2010**, *19*, 104.

(38) Kataky, R.; Lopes, P. *Chem. Commun.* **2009**, 1490.

(39) Hu, Z.; Jiang, J. *J. Phys. Chem. B* **2009**, *113*, 15851.

(40) Tang, L.; Shi, L.; Bonneau, C.; Sun, J.; Yue, H.; Ojuva, A.; Lee, B.-L.; Kritikos, M.; Bell, R.G.; Bacsik, Z.; Mink, J.; Zou, X. *Nature Materials* **2008**, *7*, 381.

(41) Tobis, J.; Boch, L.; Thomann, Y.; Tiller, J.C. *Journal of Membrane Science* **2011**, *372*, 219.

(42) Stöber, W.; Fink, A.; Bohn, E. *J. Colloid Interface Sci.* **1968**, *26*, 62.

(43) Wang, W.; Gu, B.; Liang, L.; Hamilton, W. *J. Phys. Chem. B* **2003**, *107*, 3400.

(44) Le, T. V.; Ross, E. E.; Velarde, T. R. C.; Legg, M. A.; Wirth, M. J. *Langmuir* **2007**, *23*, 8554.

(45) Chabanov, A. A.; Jun, Y.; Norris, D. J. *Appl. Phys. Lett.* **2004**, *84*, 3573.

(46) Zheng, S.; Ross, E.; Legg, M. A.; Wirth, M. J. *J. Am. Chem. Soc.* **2006**, *128*, 9016.

(47) Hiramatsu, H.; Osterloh, F.E. *Langmuir* **2003**, *19*, 7003.

(48) Cichelli, J.; Zharov, I. *J. Mater. Chem.* **2007**, *17*, 1870.

(49) Pirkle, W.H.; House, D.W.; Finn, J.M. *J. Chromatogr.* **1980**, *192*, 143.

(50) Abelow, A.E.; Zharov, I. *Soft Matter* **2009**, *5*, 457.

(51) Lu, L.; Randjelovic, I.; Capek, R.; Gaponik, N.; Yang, J.; Zhang, H.; Eychmüller, A. *Chem. Mater.* **2005**, *17*, 5731.

(52) Lee, S.B.; Martin, C.R. *Anal. Chem.* **2001**, *73*, 768.

(53) Hess, A.; Sehnert, J.; Weyhermüller, T.; Metzler-Nolte, N. *Inorg. Chem.* **2000**, *39*, 5437.

(54) Newton, M.R.; Morey, K.A.; Zhang, Y.; Snow, R.J.; Diwekar, M.; Shi, J.; White, H.S. *Nano Lett.* 2004, 4,875.

(55) Krishna, P.; Pandey, D. Close-packed structures. International Union of Crystallography, [Internet]. [cited 2012 March 14]. Available from: http://www.iucr.org/education/pamphlets/5/full-text

(56) Cussler, E.L. *Diffusion: Mass Transfer in Fluid Systems*, Cambridge University Press, New York, 2nd edn, 1997.

(57) Demirtas, H.N.; Bozkurt, S.; Durmaz, M.; Yilmaz, M.; Sirit, A. *Tetrahedron* 2009, 65, 3014.

(58) Mollard, A.; Ibragimova, D.; Antipin, I.S.; Konovalov, A.I.; Stoikov, I.; Zharov, I. *Microporous and Mesoporous Materials* **2010**, *131*, 378.

(59) Cichelli, J.A. "Permselective Transport of Chiral Molecules Through Nanoporous Opal Membranes". Ph.D. dissertation, University of Utah, 2009.

(60) Schepelina, O.; Zharov, I. *Polym. Prepr.* **2007**, *48*, 455.

(61) Schepelina, O.; Zharov, I. *Langmuir* **2007**, *23*, 12704.

(62) Cichelli, J.A.; Abelow, A.E.; Ignacio-de Leon, P.A.; Zharov, I. "Chiral Permselectivity in Nanoporous Colloidal Films Modified with Chiral Polymer Brushes" *Manuscript in Preparation*.

CHAPTER 4

SIZE-SELECTIVE TRANSPORT OF DENDRIMERS THROUGH NANOPOROUS FREE-STANDING COLLOIDAL MEMBRANES

Introduction

One of the most useful means of separating molecules based on their size (specifically, according to their hydrodynamic volume) is size exclusion chromatography (SEC).[1] However, the resolution of SEC columns is affected by the manner in which the column is prepared and used. To achieve good separations, proper column packing as well as a good pouring technique and column maintenance must be performed.[2] Indeed, overpacking can diminish pore size within the beads while underpacking can cause smaller molecules to elute more easily along with the bulk of the solvent rather than being trapped in the pores. In addition, the presence of a solvent head at the top of the column can broaden the elution band as the sample is diluted upon loading. These problems can be circumvented by using membranes. In addition, one need not monitor the separation process when employing membranes because there is no need to continually add more of the mobile phase, thereby also making the separations easier.

The over-all goal of this project is to apply free-standing nanoporous colloidal membranes (nanofrits) to the separation of biologically important molecules, which will be discussed in Chapter 5. In a proof-of-concept experiment, polyamidoamine (PAMAM) dendrimers have been chosen as diffusion probes. Dendrimers are highly suitable for this purpose due to their high monodispersity and well-defined molecular architecture.[3] Because

dendrimers are available in sizes ranging from 2-20 nm, they are good diffusion probes for nanoporous structures. For example, determination of the largest size dendrimer that can diffuse through a colloidal membrane may be used to define the effective nanopore size.[4] Full generation (G1, G2, etc.) PAMAM dendrimers are terminated with primary amine groups, which are readily subjected to standard dye-labeling methods.[5]

This chapter describes the preparation of nanoporous colloidal membranes using the vertical deposition method by self-assembly of silica spheres of 260 – 430 nm diameter from a colloidal solution. Sintering produces free-standing nanofrits with a relatively large surface with no noticeable mechanical defects. Diffusion rates of Rhodamine B isothiocyanate-labeled PAMAM dendrimers were studied as a function of dendrimer size, nanopore size and nanopore surface charge density to determine transport selectivity of as-sintered and rehydroxylated colloidal membranes.

Experimental Section

Materials

Chemicals. Ammonium hydroxide (28-30% as NH_3, EMD Chemicals, Inc.), tetrabutylammonium hydroxide (40% wt solution in water, Sigma-Aldrich), chloroform (ACS grade, VWR International), methanol (HPLC grade, Mallinckrodt), nitric acid (68-70%, ACS-grade, EMD Chemicals, Inc.), tetraethylorthosilicate (99.999+%, Alfa Aesar), ethanol (200 proof, ACS-grade, Pharmaco-Aaper), PAMAM dendrimer 1,4-diaminobutane core, amidoamine surface, generation 1 (20% wt solution in methanol, Dendritic Nanotechnologies Inc.), PAMAM dendrimer 1,4-diaminobutane core, amidoamine surface, generation 2 (20% wt solution in methanol, Dendritic Nanotechnologies Inc.), PAMAM dendrimer 1,4-diaminobutane core, amidoamine surface, generation 3 (20% wt solution in methanol, Aldrich), PAMAM dendrimer 1,4-diaminobutane core, amidoamine surface, generation 4 (10% wt solution in methanol, Dendritic Nanotechnologies Inc.), PAMAM dendrimer 1,4-diaminobutane core, amidoamine

surface, generation 5 (10% wt solution in methanol, Aldrich), Rhodamine B isothiocyanate (mixed isomers, Sigma) were all used as received. Millipore water (18 MΩ•cm) used in all experiments was obtained from a Barnstead "E-pure" water purification system. Acetonitrile (HPLC grade, VWR Scientific) was freshly distilled from calcium hydride. TLC was performed using Silica gel 60 F_{254} on aluminium sheets (EMD Chemicals, Inc.). Dialyses were performed using Slide-A-Lyzer dialysis cassettes (2,000 MWCO, Thermo Scientific).

Instrumentation. Scanning electron microscopy (SEM) images were obtained using either a Hitachi S3000-N or an FEI NanoNova instrument. UV/Vis measurements were performed using an Ocean Optics USB2000 or USB4000 instrument. A Branson 1510 sonicator was used for all sonications. A Clay Adams Compact II Centrifuge (3200 rpm, Becton Dickinson) was used for all centrifugations. A Fisher Scientific Isotemp Programmable Muffle Furnace (Model 650) was used for all sintering purposes.

Methods

Preparation of 350nm-diameter silica spheres. All silica spheres were prepared according to modifications of previously reported procedures.[6] All glassware was cleaned with Millipore water prior to use. A batch of silica spheres was made by mixing 500.0 mL of an ethanolic solution containing TEOS (51.4 mL, 0.20 mol) with 500.0 mL of an ethanolic solution containing NH_4OH (70.0 mL, 1.1 mol) and water (257 g, 14.3 mol). These two solutions were poured simultaneously in a 2 L Erlenmeyer flask and vigorously stirred. The resulting mixture has final concentrations of 0.2 M TEOS, 1.1 M NH_3 and 17.0 M H_2O. The onset of turbidity after a short while indicated the start of silica sphere formation. After 24 h, the mixture was then poured into 15 mL centrifuge tubes (Corning) and centrifuged for 10 min. The supernatant was discarded, leaving the spheres as pellets at the bottom of the centrifuge tubes. Purification of the spheres was achieved by a repetitive cycle of suspending the spheres via sonication for 10 min followed by centrifugation for 10 min in a gradient series of 10 mL supernatant: 100% water,

25% ethanol, 50% ethanol, 75% ethanol (twice) and finally 100% ethanol. After the final rinsing, the supernatant was decanted and the silica spheres air-dried overnight. The dried spheres were then preshrunk by transferring to a Petri dish (breaking any large aggregates with a spatula) and placing in a furnace programmed to heat the spheres for 4 h at 600 °C[7] (desired temperature achieved at a heating rate of 20 °C/min). SEM images were taken of the spheres and the size was determined from 100 individually measured spheres to be 346 ± 15 nm in diameter.

Preparation of 230nm-diameter silica spheres. A batch of smaller size silica spheres was also prepared and preshrunk as outlined above. The final concentrations of the reagents were 0.2 M TEOS (51.4 mL, 0.20 mol), 0.4 M NH_3 (26.78 mL, 0.4 mol) and 16.0 M H_2O (288 g, 16.0 mol) in an ethanolic reaction solution of total volume of 1.0 L. The reaction mixture was stirred vigorously for 24 h at room temperature. SEM images of the spheres were taken and the diameters determined from 100 individually measured silica spheres in each sample to be 261 ± 20 nm and 231 ± 20 nm before and after preshrinking, respectively.

Preparation of 430nm-diameter silica spheres. A batch of larger size silica spheres was also prepared and preshrunk using a modification of the procedure above. The final concentrations of the reagents were 0.2 M TEOS (51.4 mL, 0.20 mol), 4.0 M NH_3 (267.8 mL, 4.0 mol) and 5.0 M H_2O (90 g, 5.0 mol) in an ethanolic reaction solution of total volume of 1 L. The reaction mixture was stirred vigorously and its temperature maintained at 10 °C for 6 h. SEM images of the spheres were taken and the diameters determined from 100 individually measured silica spheres in each sample to be 432 ± 27 nm and 427 ± 29 nm before and after preshrinking, respectively.

Preparation of as-sintered nanofrits. The nanofrits were prepared by a vertical deposition onto a glass substrate of ~12 wt % colloidal solutions of preshrunk silica spheres in ethanol. The resulting membranes were then gently lifted from the substrate and sintered in a furnace for 12 h at 1050 °C[7] (desired temperature achieved at a heating rate of 20 °C/min). The sintered silica colloidal membranes were noticeably more robust and durable, making handling

easier. SEM images of these nanofrits were taken to give average diameters of 252 ± 10 nm, 100 ± 6 nm and 362 ± 27 nm, respectively in the order of description above, as measured from 100 individual spheres in each colloidal membrane. The thickness of each colloidal membrane was measured with a Vernier caliper at six different points throughout the piece. To make as-sintered frits, the pieces were then sandwiched between two PTFE washers (5.0 mm inner diameter, 14.0 mm outer diameter and 1.0 mm thickness, Small Parts, Inc.) with Loctite Hysol 0151 Epoxy. Nanofrits constructed as such were allowed to cure for at least 24 h prior to their use for diffusion experiments.

Preparation of rehydroxylated nanofrits. Rehydroxylated frits may be prepared as well. Hydroxyl groups were reintroduced onto the surfaces of the colloidal membranes by immersing the pieces in an aqueous pH 9.5 solution of tetrabutylammonium hydroxide (in a polyethylene bottle) maintained at 60 °C for 24 h in an oil bath.[7a] The rehydroxylated pieces were then washed with Millipore water, 1 M nitric acid, methanol, Millipore water and acetonitrile consecutively. The air-dried pieces were then made into nanofrits in the same manner mentioned above.

Modification of Dendrimers. PAMAM dendrimers of generations 1 to 5 were used as received and dye-labeled with Rhodamine B isothiocyanate in a facile manner according to the following procedure. The dye was initially dissolved by stirring in no more than 2.00 mL of absolute ethanol under an inert atmosphere (N_2 gas). An aliquot of the dendrimer solution was then added to the dye solution and allowed to react for 1 h at room temperature. The dendrimers were found to react nearly stoichiometrically with the isothiocyanate group on the dye. The resultant ratio of dye per dendrimer molecule ranged from 2 to 6, as evaluated by UV/Vis Absorbance measurements at 546 nm (determined λ_{max} with measured ε = 52,829 M^{-1} cm^{-1} from prepared standard solutions of the dye). The success of the reaction was confirmed by TLC analysis (mobile phase, $CHCl_3$/MeOH/H_2O in a 70:30:4 v/v/v ratio).[8] The dye-labeled PAMAM had an R_f value of 0 while the excess dye was observed at R_f close to 1. The dye-labeled

dendrimers were purified via dialysis. The reaction mixture was placed in a Slide-A-Lyzer dialysis cassette with a 3-mL volume capacity and 2,000 MW cut-off and dialyzed overnight with stirring against 400 mL of deionized water. The dialysis bath was changed three times.

Diffusion measurements through nanofrits. Diffusion experiments through the colloidal membranes were performed by placing a nanofrit between two connected 1-cm quartz cuvettes. The feed cell contained 4.00 mL of an aqueous dye-labeled dendrimer solution while the reservoir cell contained 4.00 mL of deionized water. The nanofrit was placed between two Kalrez o-rings to guard against leaking, and the whole assembly was then secured with a clamp. Each cell was covered with Parafilm to prevent loss of sovent due to evaporation, and the contents of both cells continually stirred. The reservoir cell was placed between two fiber optic cables and was initially blanked. The flux was monitored by recording the absorbance at 546 nm in the reservoir cell for at least 18 h. Data points were acquired every 150 s with an initial delay of 150 s. Prior to using a nanofrit for a new trial, the pieces were immersed in deionized water for at least two days and the water replaced occasionally to ensure removal of any previous probe molecule from within the colloidal films. All measurements were repeated in triplicate.

Results and Discussion

Nanoporous silica films can be easily prepared by deposition of silica nanospheres from colloidal solutions. However, the resulting films were quite fragile and needed a solid support such as glass to prevent disintegration (Figure 4.1). To prepare free-standing robust membranes, the silica spheres needed to be sintered. They have to be initially preshrunk at 600 °C prior to forming the films. Calcinating the spheres is reported to prevent the formation of cracks within the membrane upon sintering at further elevated temperatures.[7b] Calcination ensured the complete removal of solvent molecules (water and ethanol) trapped inside the silica spheres and produced denser spheres as evidenced by the decrease in diameter as measured by both dynamic light scattering (DLS) and scanning electron microscopy (SEM) (Table 4.1). Figure 4.1 shows an

SEM image of a colloidal crystal sintered at 1050 °C and demonstrates the absence of major defects, such as cracks, over a large area. Occasional point defects within the *fcc* lattice were present but did not seem to persist beyond one or two layers of the spheres. The adjacent spheres became fused at contact points. Sintering led to even greater decreases in the sizes of the spheres. It seemed that smaller spheres experienced greater reductions in size, presumably due to their larger surface area-to-volume ratio compared to larger spheres. Spheres with preshrunk diameter of 235 nm decreased in size by 57.4 % to yield membranes comprised of 100 nm spheres; 345 nm

Table 4.1. Summary of preparation conditions and sizes of silica spheres.

	Measured diameter, nm	
	DLS	SEM
[TEOS] = 0.2 M, [NH_3] = 1.1 M, [H_2O] = 17.0 M, 25 °C for 24 h		
As made	388 ± 30	
Preshrunk	359 ± 30	345 ± 20
Sintered		252 ± 10
[TEOS] = 0.2 M, [NH_3] = 0.4 M, [H_2O] = 16.0 M, 25 °C for 24 h		
As made	260 ± 30	261 ± 20
Preshrunk	239 ± 30	235 ± 20
Sintered		100 ± 6
[TEOS] = 0.2 M, [NH_3] = 4.0 M, [H_2O] = 5.0 M, 10 °C for 6 h		
As made	444 ± 40	432 ± 30
Preshrunk	418 ± 30	427 ± 30
Sintered		362 ± 30

(preshrunk) spheres decreased by 27.0 % to 252 nm while 427 nm (preshrunk) spheres decreased in size by only 15.2 % to a diameter of 362 nm. The robust free-standing colloidal membranes were then prepared for diffusion experiments by sandwiching between two washers using an epoxy resin as an adhesive (Figure 4.2).

The size of the 3D nanopores inside the nanofrits can be estimated from the geometry of an *fcc* system. The distance from the center of the nanopore projection to the nearest silica sphere surface is ca. 15 % of the sphere radius.[9] Thus, nanofrits composed of 100 and 362 nm-diameter spheres will have nanopores whose projection centers are 7.5 and 27.2 nm, respectively, away from the nearest silica sphere surface.

To determine whether size-selective molecular transport could be achieved with the nanofrits and to determine the effect of the size of the nanopore size and nanopore surface charge, we decided to study the diffusion of dendrimers of increasing generations and increasing diameters (Table 4.2). This was done by measuring the diffusion rate R_D (mol·sec^{-1}) through a nanofrit of a known thickness L and area S (cm^2) as driven by a known concentration gradient ΔC. R_D was determined by recording the number of moles of a molecule that diffuses through the membrane as a function of time in an apparatus shown in Figure 4.3. Knowing the value of R_D allowed for the calculation of the molecular flux $J_{colloid}$ (mol·sec^{-1}·cm^{-2}) through the nanofrit (Equation 4.1). A solution of Fick's law for diffusion (Equation 4.2) can then be used to determine the effective diffusion coefficient D_{eff} (cm^2·sec^{-1}) of a diffusing species in a particular solvent (in our case water) as it traversed through the colloidal nanofrit.[10] D_{eff} values take into account the effect of intrinsic opal properties such as void fraction ($\varepsilon = 0.26$) and tortuosity ($\tau \sim 3.0$) compared to the free diffusion coefficient in a given solvent D_{sol} (Equation 4.3).

$$R_D = J_{colloid} \times S \qquad (4.1)$$

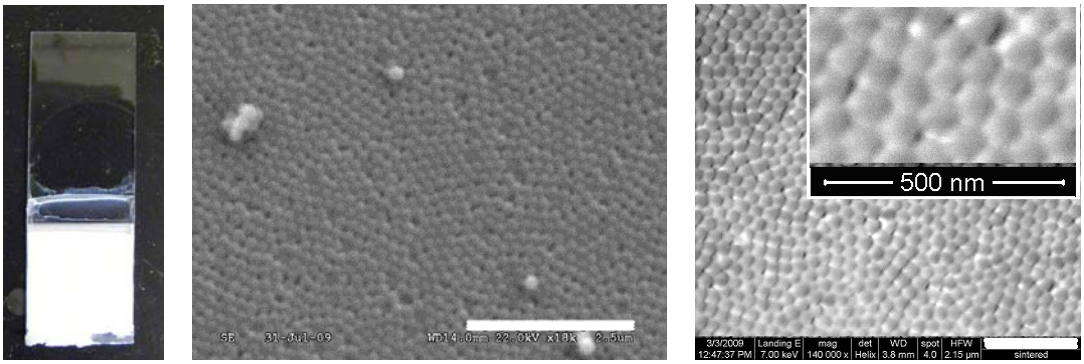

Figure 4.1. **(**Left) A colloidal film formed by vertical deposition onto a glass slide. (Middle) SEM image of a sintered membrane made from 235 nm (preshrunk diameter) silica spheres (size bar = 2.5 μm). This image shows that there are no major cracks or defects within the *fcc* lattice of the sample. (Right) High-Resolution SEM image of a sintered membrane made from 101 nm (DLS data, as-made) silica spheres (size bar = 500 nm). The inset is a magnified image that shows adjacent spheres fused at contact points.

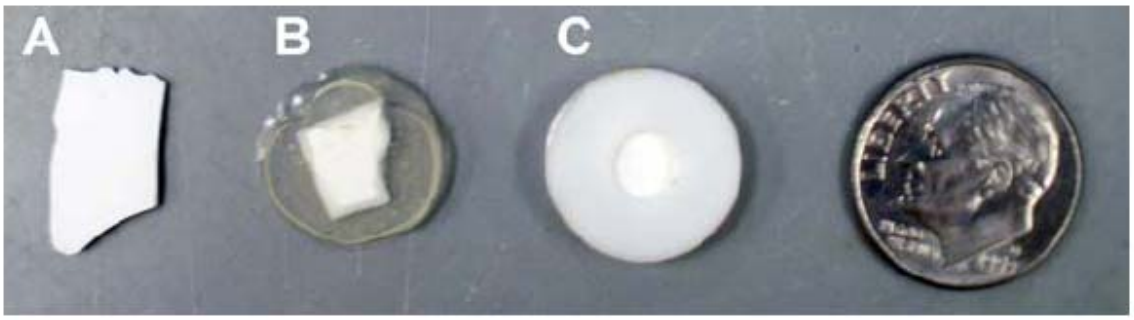

Figure 4.2. (A) A sintered colloidal membrane (B) embedded in epoxy and (C) sandwiched between a pair of PTFE washers to construct a nanofrit (a dime is included for size comparison).

$$J_{\text{colloid}} = \frac{\Delta C}{L} \times D_{\text{eff}} \tag{4.2}$$

$$D_{\text{eff}} = \frac{\varepsilon}{\tau} \times D_{\text{sol}} \tag{4.3}$$

In order to monitor the diffusion of the dendrimers through the nanofrits, dye-labeled PAMAM dendrimers from generations 1 to 5 were prepared (Figure 4.4). The conjugation of the dye to the -NH_2 termini of the dendrimers occured in a facile reaction involving a nucleophilic attack of the thiocarbonyl C in Rhodamine B-NCS by the -NH_2 endgroups of the dendrimer.[11] Removal of excess unreacted dye was achieved by dialysis against deionized water. The extent of dye-labeling of each dendrimer sample was estimated from absorbance measurements of the dialyzed samples. We checked for the complete removal of unreacted dye by TLC. The extent of dye-labeling was purposefully kept low so as not to cause significant changes in the sizes of the diffusion probes (Table 4.2).

Figure 4.5 shows the flux of various diffusing species through a nanofrit as a function of time. These flux plots are representative of the observed differences in the diffusion rates of the different dendrimer species employed through the numerous nanofrits constructed and investigated. Tables 4.3 and 4.4 summarize the calculated D_{eff} values for the dye-labeled PAMAM dendrimers used in the current work. Comparison of the calculated D_{eff} values for the same nanofrit showed that there is a general trend of decreasing rate of diffusion with increasing size of the diffusing species (Figure 4.6).

The above trend can be demonstrated quantitatively by calculating the ratio of diffusion coefficients for each of the higher generation dendrimers relative to G1. We rearranged the Stokes-Einstein relation (Equation 4.4):

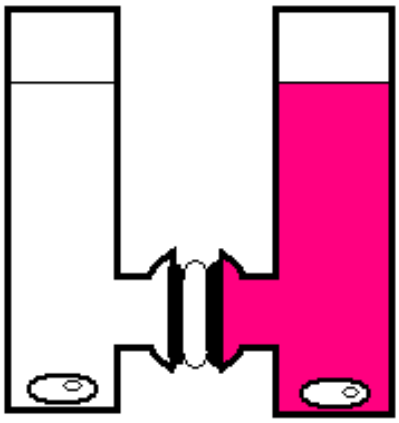

Figure 4.3. Diffusion experiment set-up. The absorbance at the reservoir cell (left) was monitored at 546 nm as the species diffused from the feed cell (right).

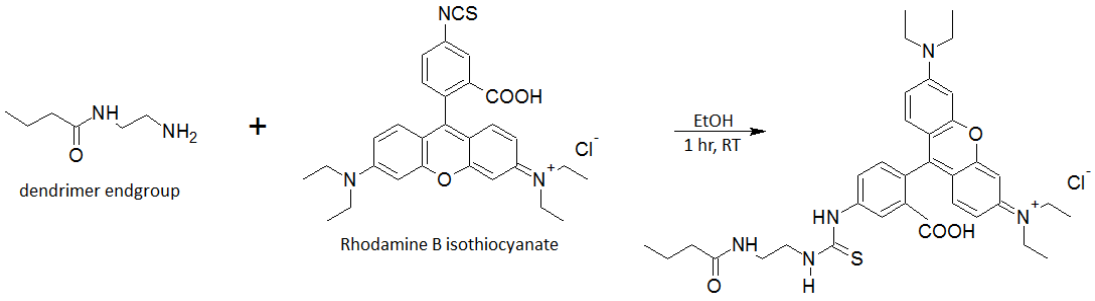

Figure 4.4. Reaction scheme for dye-labeling dendrimers. The reaction was carried out at room temperature in a minimal amount of anhydrous EtOH under N_2 gas to minimize decomposition of the dye.

$$R_{\mathrm{H}} = \frac{k_{\mathrm{B}} \times T}{6\pi\eta \times D_{\mathrm{sol}}} \tag{4.4}$$

(where R_{H} is the Stokes-Einstein radius, k_B is the Boltzmann constant, T is temperature and η is the solution viscosity) to give an estimate of the relative diffusion rates, $D_2/D_1 = R_{\mathrm{H1}}/R_{\mathrm{H2}}$, assuming similar viscosities for the dendrimer solutions in water (the concentrations were sufficiently low to make this a valid assumption). The ratios of the dendrimer radii were then used as correction factors to account for the fact that bulkier molecules will diffuse more slowly even in free solution.

The results for nanofrits sintered from 100 nm spheres (7.5 nm 'radius' nanopores) showed an abrupt change in diffusion rates from G2 to G3. While G2 dendrimer diffused as fast as G1, G3 has an apparent diffusion rate ca. 1.5 times lower, and G4 appeared to have roughly the same diffusion rate as G3.

Table 4.2. Estimated diameters of the diffusing species. The value for Rhodamine B is taken from literature[12] while the diameters of the unmodified dendrimers are as provided by the manufacturer.

Diffusing species	Diameter, nm	No. of -NH_2 end groups per dendrimer molecule	No. of dye molecules per dendrimer molecule
Rhodamine B	1.6		
G1	1.9	8	2.9
G2	2.6	16	2.8
G3	3.6	32	2.7
G4	4.4	64	1.4
G5	5.7	128	5.7

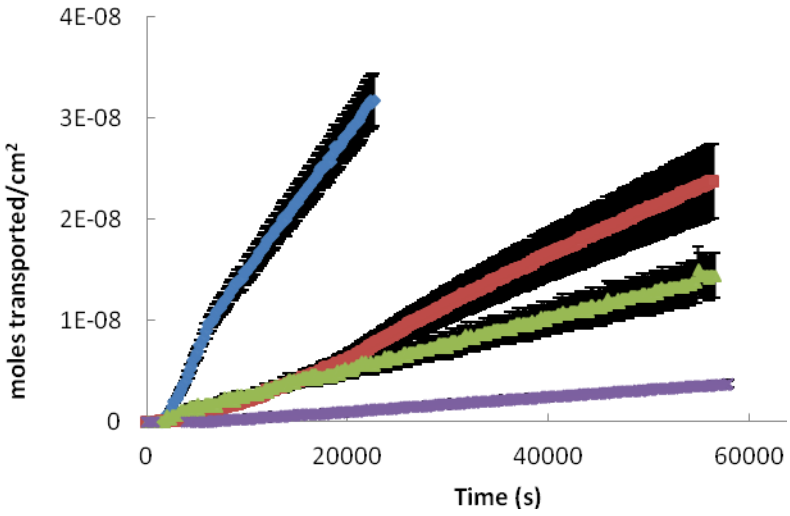

Figure 4.5. A representative flux plot for Rhodamine B (blue) and dye-labeled PAMAM G1 (red), G4 (green) and G5 (purple). Data shown were particularly for a rehydroxylated nanofrit with 252 nm sphere size and 0.597 mm thickness.

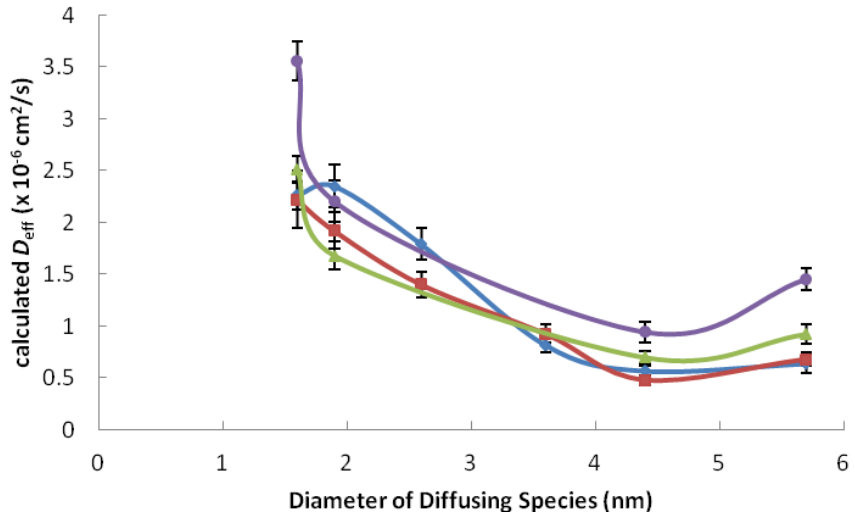

Figure 4.6. Comparison of the calculated D_{eff} (× 10^{-6} cm^2/s) with increasing size of diffusing species through nanopores of 7.5 nm 'radius' for sintered (blue) and rehydroxylated (red) membranes and through nanopores of 27.2 nm 'radius' for sintered (green) and rehydroxylated (purple) membranes.

The diffusion coefficient for G5 was slightly higher than that for G4. Since the dendrimers cannot be considered as hard spheres, we attributed this to the possibility of shape distortion from a sphere into an ellipsoid that helped G5 to "squeeze" through the nanopores. Globular dendrimers are well-known to be deformable, especially in confined spaces where crowding enhances interaction with one another through a relatively soft pair potential.[13]

Resultant selectivities suggest an effect of tortuosity, considering there is only about 3 - 4 nm difference in the diameters of G3 from that of G1 dendrimers.

Nanofrits were constructed from three different sphere sizes, which allowed us to observe how molecular transport was affected by changing the nanopore size. It is apparent from Tables 4.3 and 4.4 that the calculated D_{eff} for any given diffusing species was dependent on the nanopore size, with the smallest values generally corresponding to diffusion experiments through the 7.5 nm pore 'radius' nanofrits. Size selectivity is expected to improve as the nanopores became narrower, until a point is reached where complete blockage to diffusion occured as the nanopore became too small to accommodate a diffusing species. Given the estimated diameters of the diffusing species (Table 4.2) and the nanopore sizes of the membranes employed in this study, it was not surprising that complete blockage (particularly of the smaller species G1 and G2 dendrimers) was not observed.

While the apparent transport rate for G4 was about twice as slow as that of G1 through larger nanopores of 27 nm 'radius' (Table 4.4), normalization revealed that the observed decrease in flux was due to the inherent differences in diffusion coefficients as a result of increased size for higher generation dendrimers. Moreover, we observed the diffusion coefficient for G5 dendrimer through 27 nm nanopores that is 1.5 times higher than that of G4 dendrimer. We attribute this observation to the flexibility of G5 dendrimer, as discussed above.

Another set of nanofrits composed of 252 nm spheres (19 nm nanopore 'radius') was investigated and the results were intermediate between the two already discussed. In the hopes of achieving better selectivities, attempts were made to construct nanofrits from 101 nm spheres[14]

Table 4.3. Summary of calculated average effective diffusion coefficients and selectivities through as-sintered and rehydroxylated frits (100 ± 6 nm diameter silica spheres).

PAMAM species	Radius correction coefficient	D_{eff} (cm^2/s) × 10^{-6}	% D_{eff} ratio relative to G1
		As-sintered	
G1	1.0	2.4 ± 0.4	100
G2	0.73	1.8 ± 0.3	104 ± 30
G3	0.53	0.8 ± 0.2	66 ± 20
G4	0.43	0.6 ± 0.1	55 ± 10
G5	0.35	0.6 ± 0.2	77 ± 30
		Rehydroxylated	
G1	1.0	1.9 ± 0.4	100
G2	0.73	1.4 ± 0.2	100 ± 30
G3	0.53	0.9 ± 0.2	90 ± 20
G4	0.43	0.5 ± 0.1	58 ± 20
G5	0.35	0.7 ± 0.1	66 ± 20

(as-made), which eventually shrunk to diameters of 65 nm upon sintering (Figure 4.1). However, the production of membranes with sufficiently large surface area and uniform thickness proved to be difficult, either by vertical or sedimentation deposition methods.

In order to confirm that the observed selectivities were due to size discrimination and not electrostatic effects, the diffusion experiments were also performed using rehydroxylated nanofrits. The difference between as-sintered and rehydroxylated frits was that the former have a greater number of terminal siloxanes Si-O-Si on the surface.[15] During the rehydroxylation, the

Table 4.4. Summary of calculated average effective diffusion coefficients and selectivities through as-sintered and rehydroxylated frits (362 ± 30 nm diameter silica spheres).

PAMAM species	Radius correction coefficient	D_{eff} (cm^2/s) × 10^{-6}	% D_{eff} ratio relative to G1
		As-sintered	
G1	1.0	1.7 ± 0.3	100
G4	0.43	0.7 ± 0.1	98 ± 20
G5	0.35	0.9 ± 0.2	158 ± 40
		Rehydroxylated	
G1	1.0	2.2 ± 0.4	100
G4	0.43	0.9 ± 0.2	100 ± 30
G5	0.35	1.4 ± 0.2	189 ± 50

nucleophilic attack of OH^- on the Si atom converted the terminal siloxanes into the surface silanol Si-OH groups.[7a] Thus, in contact with an aqueous medium as-sintered frits should have a smaller negative charge on the surface compared to the rehydroxylated ones, whose surface silanols (pK_a 6 – 8)[16] can dissociate to give $Si\text{-}O^-$. This rationalization was supported by zeta potential (ζ) measurements of -41.22 mV for sintered and -44.92 mV for rehydroxylated samples (compared to -46.88 mV for as-made silica spheres from the same batch). If transport selectivity of the dendrimers through the nanofrits was due to electrostatic effects, different diffusion rates through the rehydroxylated frits would be expected as the process would be affected not only by concentration gradient but also by electrostatic interactions between the negatively charged nanopore surface and the cationic dye-labeled dendrimers. Comparison of both calculated D_{eff} and selectivity values showed (Tables 4.3 and 4.4) that while there was generally no apparent

difference between the as-sintered and the rehydroxylated nanofrits, G3 has almost the same diffusion coefficient as G2 for the rehydroxylated membranes with smaller pores. The diffusion coefficient only decreased significantly for G4, whereas the corresponding selectivity in the as-sintered nanofrits occurred for G3. This demonstrated that the transport of the dendrimers was also affected by the interaction between the diffusing molecules and the nanopore surfaces. Enhanced electrostatic attractions with rehydroxylated surfaces could facilitate the transport of the cationic dendrimers, thus explaining the slight difference in selectivities. Nevertheless, the transport properties were dominantly governed by size-selectivity.

Finally, some comments should be made about the durability of the constructed nanofrits. The frits used in this work were sufficiently robust to last for several months, and more often than

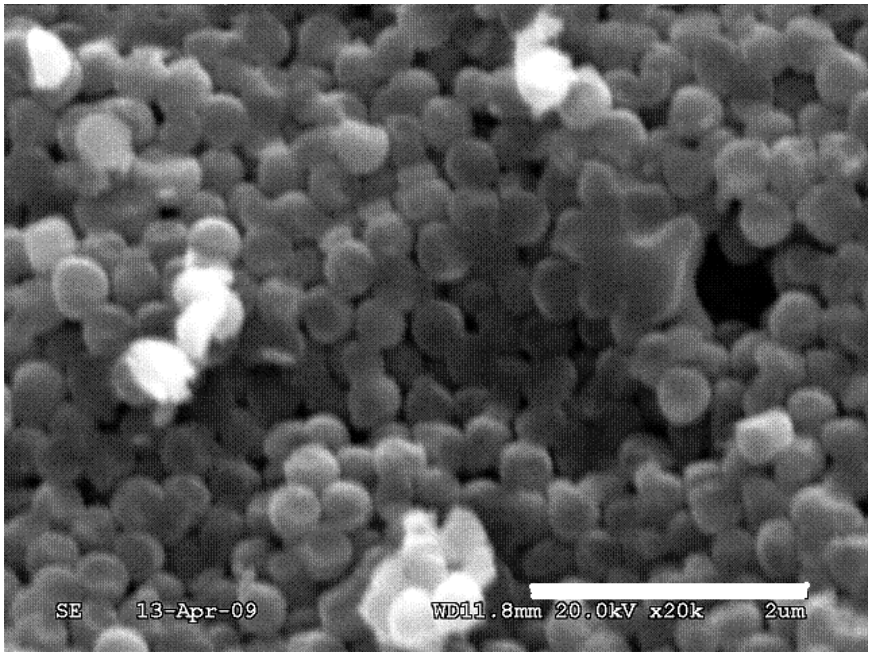

Figure 4.7. SEM image of a used nanofrit of 362 nm diameter spheres (size bar = 2 μm). The surface was considerably less orderly than prior to its use, and the presence of point defects appeared to be more frequent.

not, it was the epoxy resin that first fell apart leading to the disintegration of the nanofrit assembly. However, prolonged and repeated usage affected the performance. Diffusion experiments of dye-labeled PAMAM G4 dendrimers through as-sintered frits conducted two months after the initial use of the nanofrits yielded calculated D_{eff} values that were higher than the calculated results for G3 dendrimers. Specifically, the results were 1.71×10^{-6}, 2.75×10^{-6} and 5.31×10^{-6} cm^2/s through 0.413, 0.614 and 0.790 mm-thick nanofrits, respectively. SEM images revealed that the surface of a used nanofrit was less orderly and seemed to contain more point defects throughout the colloidal membrane (Figure 4.7).

Conclusions

Molecular transport of five generations of dye-labeled PAMAM dendrimers through robust, free-standing silica colloidal membranes (nanofrits) has been studied by recording the flux using UV/Vis spectroscopy. The effective diffusion coefficients for each of the generation dendrimers have been calculated and the selectivities for varying size of diffusing species were also evaluated. We demonstrated that molecular transport through silica colloidal crystals is size-selective and the selectivity is enhanced by the tortuous path diffusing molecules take through the colloidal crystal. Comparison of results for diffusion through as-sintered (with less negative surface charge) and rehydroxylated (with greater number of negative surface charges attributed to surface silanol dissociation in aqueous environment) nanofrits demonstrated that the observed selectivities were affected by electrostatic interactions between the negative silica surface and the cationic diffusing species but were mostly due to size discrimination.

Our proof-of-concept experiments showed that the nanofrits have potential applications in size-selective separations but their efficiency has to be further optimized by controlling the nanopore size. There is a need for further work in this direction, specifically the development of nanofrits with even smaller nanopore sizes. Studies directed towards applying these nanofrits for

the separation of biomolecules will be the focus of Chapter 5, where we investigated the ability of our colloidal membranes to discriminate diffusing species in a mixture of several biomolecules of known masses, size and shape[17,18] (such as lysozome, bovine serum albumin and bovine hemoglobin).

References

(1) IUPAC. Compendium of Chemical Terminology, 2nd ed. ("Gold Book") Compiled by A.D. McNaught and A. Wilkinson. Blackwell Scientific Publications, Oxford (1997).

(2) Skoog, D.A.; Holler, F.J.; Crouch, S.R. *Principles of Instrumental Analysis, 6th ed.*; Thompson Brooks/Cole: California, 2006.

(3) Tomalia, D.A.; Baker, H.; Dewald, J.; Hall, M.; Kallos, G.; Martin, S.; Roeck, J.; Smith, P. *Macromolecules* **1986**, *19*, 2466.

(4) McCain, K.S.; Schluesche, P.; Harris, J.M. *Anal. Chem.* **2004**, *76*, 930.

(5) Hermansen, G.T. *Bioconjugate Techniques*; Academic Press: San Francisco, 1996.

(6) (a) Stöber, W.; Fink, A.; Bohn, E. *J. Colloid Interface Sci.* **1968**, *26*, 62. (b) Wang, W.; Gu, B.; Liang, L.; Hamilton, W. *J. Phys. Chem. B* **2003**, *107*, 3400.

(7) (a) Le, T.V.; Ross, E.E.; Velarde, T.R.C.; Legg, M.A.; Wirth, M.J. *Langmuir* **2007**, *23*, 8554. (b) Chabanov, A.A.; Jun, Y.; Norris, D.J. *Appl. Phys. Lett.* **2004**, *84*, 3573. (c) Zheng, S.; Ross, E.; Legg, M.A.; Wirth, M.J. *J.Am. Chem. Soc.* **2006**, *128*, 9016.

(8) Schlapak, D.A.; Saucedo-Zeni, N.; Latini, G.; Gruber, H.J.; Mesquida, P.; Samotskaya, Y.; Hohage, M.; Cacialli, F.; Howorka, S. *Langmuir* **2007**, *23*, 8916.

(9) Newton, M.R.; Morey, K.A.; Zhang, Y.; Snow, R.J.; Diwekar, M.; Shi, J.; White, H.S. *Nano Lett.* **2004**, *4*, 875.

(10) Cussler, E.L. *Diffusion: Mass Transfer in Fluid Systems, 2nd ed.*; Cambridge University Press: New York, 1997.

(11) Bruice, P.Y. *Organic Chemistry, 3rd ed.*; Prentice Hall: New Jersey, 2001.

(12) Klein, S.A.; Wilk, S.J.; Thornton, T.J.; Posner, J.D. *International Symposium on Advanced Nanodevices and Nanotechnology Journal of Physics: Conference Series* **2008**, *109*, 012022.

(13) Hudson, S.D.; Jung, H.-T.; Kewsuwan, P.; Percec, V.; Cho, W.-D. *Liquid Crystals* **1999**, *26*, 1493-1499.

(14) Hiramatsu, H.; Osterloh, F.E. *Langmuir* **2003**, *19*, 7003.

(15) Jal, P.K.; Patel, S.; Mishra, B.K. *Talanta* **2004**, *62*, 1005.

(16) Rosenholm, J.M.; Czuryszkiewicz, T.; Kleitz, F.; Rosenholm, J.B.; Linden, M. *Langmuir* **2007**, *23*, 4315.

(17) Yu, S.; Lee, S.B.; Kang, M.; Martin, C.R. *Nano Lett.* **2001**, *1*, 495.

(18) (a) Chun, K.Y.; Stroeve, P. *Langmuir* **2002**, *18*, 4653. (b) Smith, C.; Kirk, R.; West, T.; Bratzel, M.; Cohen, M.; Martin, F.; Bioarski, A.; Rampersaud, A.A. *Diabetes Technol. Therap.* **2005**, *7*, 151. (c) Leoni, L.; Attiah, D.; Desai, T.A. *Sensors* **2002**, *2*, 111.

CHAPTER 5

SIZE- AND CHARGE-SELECTIVE TRANSPORT OF PROTEINS THROUGH NANOPOROUS FREE-STANDING COLLOIDAL MEMBRANES

Introduction

There has been increasing interest in the use of nanoporous materials for separations involving biomolecules such as proteins and DNA.[1] Protein purification is crucial not only in medical and pharmaceutical research but also in clinical diagnosis.[2] For example, one of the biggest challenges that remain in proteomics is the removal of highly abundant proteins in biological samples as they usually complicate the detection of other proteins of interest with much lower abundance.[3]

Electrophoretic separations, despite being widely used, have several disadvantages such as low reproducibility (highly dependent on sample loading and requires some experience), small scalability (limited to small quantities)[4] and difficult accessibility for further analysis (resolved biomolecules remain trapped in the gel thus requiring blots, which make the process inconvenient and time-consuming). Chromatographic methods provide high purification efficiencies. However, the effectiveness of these pressure-driven separations can suffer from pressure fluctuations and diffusion limitations that restrict efficiency and applicability for large-scale systems,[5] in addition to requiring costly materials.

Another biomacromolecule separation method that recently gained attention is the use of membranes. Filtration membranes provide considerable economic, environmental and safety

advantages[6] compared to (as an example) protocols for plasmid isolation that employ toxic solvents, mutagenic reagents and animal-derived enzymes.[7,8] Compared to the gels used in electrophoresis, membranes have better physical and chemical stability, ease of handling[9] and provide tunable pore sizes.[4] For smaller-scale applications, membranes can be integrated into "lab-on-a-chip" systems to include a preconcentration and purification modules prior to detection.[7,10] One of the most versatile aspects of working with membranes is the almost limitless choice of constituent material. Organic ion-permeable acrylamide-based polymer and hydrogel membranes,[10] inorganic alumina membranes[6] and composite assemblies such as free-standing thin film networks of polypyrrole-coated $Cu(OH)_2$ nanostrands[11] as well as gold-coated nanotubules within the pores of a polycarbonate scaffold[12] have all been evaluated for proteins separations. The excellent durability (even under extreme conditions) and thermal stability of ceramic membranes, as well as their long operation life make for attractive features. At small pore sizes, however, the flux suffers as porosity decreases to less than 36 %,[6] in addition to the effect of the presence of dead-end pores. Hybrid organic-inorganic membranes retain the advantages associated with durable platforms, while surface modification of nanopores provides stimuli-responsive systems whose properties can be fine-tuned with careful choice of modifiers. Because substance transport and separation capabilities of membranes rely on pore density and shape (linear vs. tortuous) and surface chemistry (prevention of nonspecific interactions with proteins), these have to be studied and optimized.[13]

We have chosen silica colloidal crystals as free-standing membranes for studying protein transport. The ability to vary the pore diameter and surface chemistry of these nanopores make them ideal model systems for studying the rate and selectivity of permeate transport in membranes. Silica is biocompatible and mechanically robust,[14] and well-established silane chemistry can be used for the surface modification[15] with amine, thiol and carboxyl groups that facilitate conjugation with almost any moiety ranging from small molecules to polymers and biomolecules (e.g. peptides and oligonucleotides).[1a] Silica colloidal membranes contain pores

with uniform and narrow size distribution while retaining high porosity and surface area.[1] Silica nanoparticles are well-studied in terms of their interactions with biological media.[15] Due to silanol (Si-OH) groups, the silica surfaces possess negative charges whose magnitude depend on the pH of the surrounding medium.[6] While this can be exploited to enhance selectivity and separation efficiency of charge-bearing species (like many biomolecules),[16] it also renders the silica surfaces susceptible to nonspecific adsorption (due to electrostatics, dispersion forces and solvation forces) and can lead to problematic clogging of the pores. To address this issue, Rosen and Gu functionalized silica nanoparticles with cysteine[15] and showed increased stability with respect to aggregation in solutions of lysozyme and bovine serum albumin due to the low-fouling zwitterionic surface. White and co-workers[17] employed a monolayer of cyanosilanes to impart neutrality and biological inertness while allowing the aqueous medium to fully wet the nanopore. Elsewhere, a large number of literature[18,19] reports the use of polymers to control the surface properties of silica. For example, poly(ethylene glycol) (PEG) was shown to create stealth layers with notable resistance to opsonization[15] by preventing nonspecific adsorption of proteins.[12,14,20,21]

This chapter describes the preparation and characterization of silica nanofrits whose surfaces have been modified with PEG chains as anti-biofouling coatings. Using spectroscopic measurements to monitor the diffusion through our various membranes, we investigated the effect of surface functionality, pore charge and pore size on biomolecular transport through the nanopores.

Experimental Section

Materials

Chemicals. Ammonium hydroxide (28-30 % as NH_3, EMD Chemicals, Inc.), tetrabutylammonium hydroxide (40 % wt solution in water, Sigma-Aldrich), potassium phosphate monobasic (Sigma), potassium dibasic trihydrate (Mallinckrodt), sodium carbonate anhydrous

(Mallinckrodt Chemicals), tetraethylorthosilicate (99.999+ %, Alfa Aesar), 3-aminopropyltriethoxysilane (99 %, Aldrich), poly(ethylene glycol) monomethyl ether mono(succinimidyl succinate) ester (Polysciences, Inc.), lysozyme (from chicken egg white, Sigma), albumin (from bovine serum, lyophilized powder, Sigma), hemoglobin (from bovine blood, lyophilized powder, Sigma), nitric acid (68-70 %, ACS-grade, EMD Chemicals, Inc.), xylene (ACS, Fisher Scientific), ethanol (200 proof, ACS-grade, Pharmaco-Aaper), methanol (ACS Reagent, Sigma-Aldrich), N,N-dimethylformamide (Mallinckrodt) and tetrahydrofuran (HPLC solvent, J.T. Baker) were all used as received. Millipore water (18 MΩ•cm) used in all experiments was obtained from a Barnstead "E-pure" water purification system. Acetonitrile (HPLC grade, VWR Scientific) was freshly distilled from calcium hydride.

Instrumentation. Scanning electron microscopy (SEM) images were obtained using either a Hitachi S3000-N or an FEI NanoNova instrument. Transmission electron microscopy (TEM) images were obtained using an FEI Philips Tecnai T-12 instrument. UV/Vis measurements were collected using an Ocean Optics USB2000 or USB4000 instrument. A Branson 1510 sonicator was used for all sonications. A Clay Adams Compact II Centrifuge (3200 rpm, Becton Dickinson) was used for all centrifugations. A Fisher Scientific Isotemp Programmable Muffle Furnace (Model 650) was used for all sintering purposes. All zeta-potential measurements were carried out in water using a NICOMP 380 ZLS Zeta Potential/Particle Sizer (PSS•NICOMP Particle Sizing Systems). Thermogravimetric analyses were performed using a TA Instruments TGA 2950 Thermogravimetric Analyzer.

Methods

Preparation of silica spheres. Three batches of silica spheres with varying sizes were prepared as previously described in earlier reports.[22] SEM images of the preshrunk (i.e., calcinated at 600 °C for 4 h) spheres were taken and the sizes were determined from 100

individually measured spheres to be 231 ± 20, 350 ± 20 and 427 ± 30 nm in diameter, respectively.

Preparation of free-standing nanofrits. The nanofrits were prepared as described in Chapter 4. SEM images of these nanofrits were taken to give average diameters of 252 ± 10 nm, 100 ± 6 nm and 362 ± 27 nm, respectively in the order of description above, as measured from 100 individual spheres in each colloidal membrane. The thickness of each colloidal membrane was measured with a Vernier caliper at six points throughout the piece. To make as-sintered frits, the pieces were then sandwiched between two PTFE washers (5.0 mm inner diameter, 14.0 mm outer diameter and 1.0 mm thickness, Small Parts, Inc.) with Loctite Hysol 0151 Epoxy. Nanofrits constructed as such were allowed to cure for at least 24 h prior to use for diffusion experiments.

Rehydroxylation of free-standing nanofrits. Prior to performing surface modifications on the sintered colloidal membranes, hydroxyl groups were reintroduced onto the surfaces by immersing the pieces in an aqueous pH 9.5 solution of tetrabutylammonium hydroxide (in a polyethylene bottle) maintained at 60 °C for 24 h in an oil bath.[22] The rehydroxylated pieces were then washed with Millipore water, 1 M nitric acid, methanol, Millipore water and acetonitrile consecutively. The air-dried pieces were then made into nanofrits in the same manner mentioned above.

Surface-modification with PEG chains. Prior to PEGylation, the preshrunk particles and rehydroxylated membranes were initially aminated. To silica substrates immersed in 40 mL dry acetonitrile, 0.20 mL of 3-aminopropyltiethoxysilane was added and the mixture was kept under N_2 (g) overnight. The modified silica spheres and membranes were rinsed with acetonitrile, tetrahydrofuran, xylene, twice with water and twice with acetonitrile, followed by air-drying.

PEG chains were tethered onto the surfaces of aminated silica using a modification of a literature method.[23] Briefly, 0.020 mmol of amines (aminated silica) was immersed in aqueous

0.05 M K_2CO_3 followed by the addition of 0.020 mmol poly(ethylene glycol) monomethyl ether mono(succinimidyl succinate) ester dissolved in minimal tetrahydrofuran. The final pH was adjusted to 7. After 1 h, the modified silica samples were collected and rinsed with *N*,*N*-dimethylformamide, two portions of water and two portions of acetonitrile. The air-dried pieces were made into nanofrits as previously described.

Determination of extent of protein adsorption. Preshrunk and PEGylated silica (0.035 g each) were separately dispersed into 6.0 mL pH 6 10 mM phosphate buffer and each colloidal solution was then divided into three 2-mL aliquots. Individual solutions (0.025 mM) of Lz, BSA and BHb were prepared using the same buffer and 2.0 mL of each protein solution were added separately to an aliquot of unmodified and modified silica followed by incubation for 24 h with gentle stirring at ambient conditions. The mixtures were centrifuged and the UV/Vis absorbance was recorded for each of the supernatants.

Diffusion measurements through nanofrits. Diffusion experiments through the colloidal membranes were performed by placing a nanofrit between two connected 1-cm quartz cuvettes. The feed cell contained 4.00 mL of a pH 6 phosphate-buffered aqueous protein solution while the reservoir cell contained 4.00 mL of the buffer solution. The nanofrit was placed between two Kalrez o-rings to guard against leaking, and the whole assembly was then secured with a clamp. Each cell was covered with Parafilm to prevent eventual evaporation, and the contents of both cells continually stirred. The reservoir cell was placed between two fiber optic cables and was initially blanked. The flux was monitored by recording the absorbance in the reservoir cell for at least 12 h. In diffusion experiments with a mixture of two proteins in the feed cell, the absorbances at both λ_{max} values for BSA and BHb (277 nm and 499 nm, respectively) were simultaneously recorded. Data points were acquired every 150 s with an initial delay of 150 s. Prior to using a nanofrit for a new trial, the pieces were immersed in buffer for at least 2 days and the water replaced occasionally to ensure removal of any previous probe molecule from within the colloidal films.

Results and Discussion

Diffusion through as-sintered membranes

The size of the 3D nanopores inside the nanofrits can be estimated from the geometry considerations of the *fcc* packing system. The distance from the center of the nanopore projection to the nearest silica sphere surface is ca. 15% of the sphere radius.[24] Thus, nanofrits composed of 100, 252 and 362 nm-diameter spheres (Table 5.1) have nanopores whose centers are 7.5, 19 and 27 nm, respectively, away from the nearest silica sphere surface.

Table 5.1. Summary of preparation conditions and sizes of silica spheres.

	Measured diameter, nm	
	DLS	SEM
[TEOS] = 0.2 M, [NH_3] = 1.1 M, [H_2O] = 17.0 M, 25 °C for 24 h		
As made	388 ± 30	
Preshrunk	359 ± 30	346 ± 20
Sintered		252 ± 10
[TEOS] = 0.2 M, [NH_3] = 0.4 M, [H_2O] = 16.0 M, 25 °C for 24 h		
As made	260 ± 30	261 ± 20
Preshrunk	239 ± 30	235 ± 20
Sintered		100 ± 6
[TEOS] = 0.2 M, [NH_3] = 4.0 M, [H_2O] = 5.0 M, 10 °C for 6 h		
As made	444 ± 40	432 ± 30
Preshrunk	418 ± 30	427 ± 30
Sintered		362 ± 30

The simplest basis for separations using nanoporous membranes is the difference in size of the analytes relative to the nanopore diameter.[1b] To determine whether size-selective biomolecular transport could be achieved with the simple system of as-sintered nanofrits (i.e. without further change in surface chemistry), we studied the diffusion of several common proteins. Lysozyme (Lz),[12] bovine hemoglobin (BHb)[25] and bovine serum albumin (BSA)[26] were chosen for their availability, size and shape range, and the existence of earlier reports that allow direct comparison with published data (Table 5.2).[1,3,6,10,12,16,27-29] Comparison of the diffusion rates for the first two proteins will provide information about the size selectivity, while comparison of the last two proteins will afford insight into the effect of the shape of the protein on the diffusion through the nanopores (BHb is roughly spherical whereas BSA has an ellipsoid shape).

The diffusion rate R_D (mol·sec^{-1}) through a nanofrit of a known thickness L and area S (cm^2) was determined by recording the number of moles of a protein that diffused through the membrane as a function of time. Knowing the value of R_D allowed for the calculation of the molecular flux $J_{colloid}$ (mol·sec^{-1}·cm^{-2}) through the nanofrit (Equation 5.1):

$$R_D = J_{colloid} \times S \tag{5.1}$$

$$J_{colloid} = \frac{\Delta C}{L} \times D_{eff} \tag{5.2}$$

A solution of Fick's law for diffusion (Equation 5.2) was then used to determine the effective diffusion coefficient D_{eff} (cm^2·sec^{-1}) of a diffusing species in the buffer solution as it traversed through the colloidal nanofrit.[30] D_{eff} values take into account the effect of intrinsic

Table 5.2. Characteristics of the proteins studied. Spectroscopic data were experimentally determined from prepared sets for calibration curves in pH 6 phosphate buffer.

	Lysozyme	Bovine Hemoglobin	Bovine Serum Albumin
Mass (kDa)	14	65	67
Dimensions (nm)	3.2 (spherical)	6.4 × 5.5 × 5	4 × 4 × 14
Stokes radius (nm)	2[12]	3.2[31]	3.6[12]
p*I*	11.4	7.1	4.8
λ_{max} Abs (nm)	280	499	277
a (L/mol·cm)	34,908	36,751	43,292

colloidal crystal properties such as void fraction ($\varepsilon = 0.26$) and tortuosity ($\tau \sim 3.0$) compared to the free diffusion coefficient in a given solvent D_{sol} (Equation 5.3):

$$D_{eff} = \frac{\varepsilon}{\tau} \times D_{sol} \tag{5.3}$$

Figure 5.1 shows the flux of the three proteins studied through as-sintered frits of 19 nm pore 'radius'. Table 5.3 summarizes the calculated D_{eff} values. We found a general trend of decreasing rate of transport with increasing size of the diffusing species. Lz diffused 3.75 and 2.1 times faster than BHb and BSA, respectively, due to its smaller size (Table 5.2). We needed to assess if the nanopores were providing the size selectivity since we used large proteins of different size. We can rearrange the Stokes-Einstein relation (Equation 5.4):

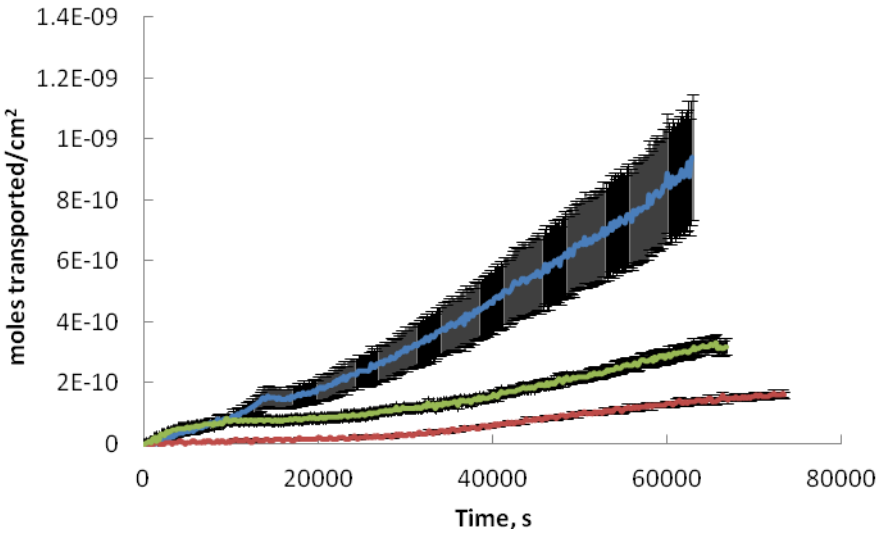

Figure 5.1. Comparison of the flux of Lz (blue), BHb (red) and BSA (green) through as-sintered frits with 19 nm pore 'radius'.

Table 5.3. Summary of protein average D_{eff} (cm^2/sec) as measured through as-sintered nanofrits.

Nanopore radius (nm)	19	7.5
Lysozyme	$(3 \pm 2) \times 10^{-6}$	$(8 \pm 2) \times 10^{-7}$
Bovine Hemoglobin	$(8 \pm 2) \times 10^{-7}$	No diffusion observed
Bovine Serum Albumin	$(1.4 \pm 0.3) \times 10^{-6}$	$(8 \pm 1) \times 10^{-8}$

$$R_{\mathrm{H}} = \frac{k_{\mathrm{B}} \times T}{6\pi\eta \times D_{\mathrm{sol}}} \tag{5.4}$$

(where R_{H} is the Stokes-Einstein radius, k_B is the Boltzmann constant, T is temperature and η is the solution viscosity) to give an estimate of the relative diffusion rates of the proteins, $D_1/D_2 = R_{\mathrm{H2}}/R_{\mathrm{H1}}$, assuming similar viscosities for the 0.25 mM protein solutions in the buffer used.[12] Hence, the Stokes-Einstein equation predicted that in free solution the diffusion coefficient of Lz would be 1.6 and 1.8 higher than those of BHb and BSA, respectively. That the ratios of fluxes for the nanofrits were higher indicates hindered transport of the proteins through the nanopores. It is furthermore important to note that while BHb and BSA were expected to diffuse at almost equal rates, BSA diffused 1.8 times faster than BHb. It is possible that the prolate ellipsoid shape of BSA may allow it to traverse more readily through the nanopores compared to the more spherical BHb despite their similar molecular weights (Table 5.2). This illustrated that the nanofrits were capable of both size-selective transport as well as shape-selectivity.

Another set of nanofrits were constructed from smaller sphere size (leading to nanopore 'radius' of 7.5 nm), which allowed the investigation of how biomolecule transport was affected by the pore size. It is apparent from Table 5.3 that D_{eff} for all diffusing species depends on the nanopore size. There is a trade-off between selectivity and throughput (or permeability) that is typically observed for membrane-based separations.[12] Size selectivity was expected to improve as the nanopores became narrower until a point where complete blockage occurred as the nanopore became too small to accommodate a diffusing species. Given the estimated diameters of Lz and BSA (Table 5.2) compared to the nanopore 'radii' employed in this study, it was not surprising that complete blockage for these proteins was not observed. However, the diffusion rates for Lz and BSA were reduced 3.7- and 18-fold, respectively, whereas a cut-off was observed for bulkier BHb. The use of smaller nanopores led to improved selectivity of 10.2 for Lz over BSA and also suggested that a clean separation of a mixture of BHb and BSA could be achieved.

The decreased diffusion is the result of using nanopores with smaller volumes. However, given the similar sizes of BSA and BHb, the dramatic difference reveals that we have to consider the proteins' interaction with the nanopore.

Protein-nanopore surface interactions

Molecular transport in small pores and confined spaces is strongly affected by the solute-wall interactions, resulting in significant reductions in diffusion coefficients.[32] Protein interactions with silica surfaces have been widely studied[1,14,33] and it is well-known that at physiological pH, silica surfaces bear a negative charge that facilitates rapid nonspecific binding of proteins[15] via van der Waals and electrical double layer forces.[16] At pH 6, Lz and BHb are both cationic according to their *p*I values (Table 5.2) with Lz bearing at least +8 charge[16] attributed to lysine residues (three of which are located in the helix-loop-helix domain of the protein which is thought to be responsible for protein-membrane binding).[34] On the other hand, BSA is anionic at pH values above its pK_a of 4.7.[2] We believe the BHb cut-off to be a consequence of electrostatic attractions between the cationic proteins and the negatively charged nanopore walls, which may promote adsorption of a layer of the BHb effectively leading to reduced nanopore volumes. This was supported by zeta potential measurements (ζ) of -46.45 mV for unmodified membranes. If so, it was reasonable that the transport rate of BHb was the most affected since its large size translated to complete nanopore blockage upon protein adsorption. In contrast, electrostatic repulsion between the anionic BSA and like-charged nanopores minimized nanopore clogging due to adsorption.

Sang and co-workers[1] reported that higher amounts of proteins are adsorbed at pH values close to the *p*I. The decreased strength of repulsive protein-protein electrostatic interactions as the net charge approached zero[16] allowed protein molecules to pack more closely and thus, more proteins can be adsorbed for a given silica unit surface. Holt and Bowcott concluded from adsorption isotherms that BSA has maximum adsorption onto silica at pH 5.[33] Thus, we decided

to use pH 6 in order to avoid working at the *p*I of any of these three proteins. To address the possibility of protein nonspecific adsorption onto silica and to further suppress the potential nanopore clogging, we chose to use short PEG chains as anti-fouling surface modifiers, which are widely used for this purpose.[35]

Preparation and characterization of PEGylated membranes

To prepare PEGylated nanofrits, hydroxyl groups were reintroduced first (Figure 5.2). Amine groups were then introduced onto the rehydroxylated surfaces, resulting in thin polymeric layers of silamines. PEG with MW 1,900 (n ~ 30) was chosen as an anti-fouling surface modifier to keep the nanopore size relatively unchanged (about 1 nm thick coating).[12] The

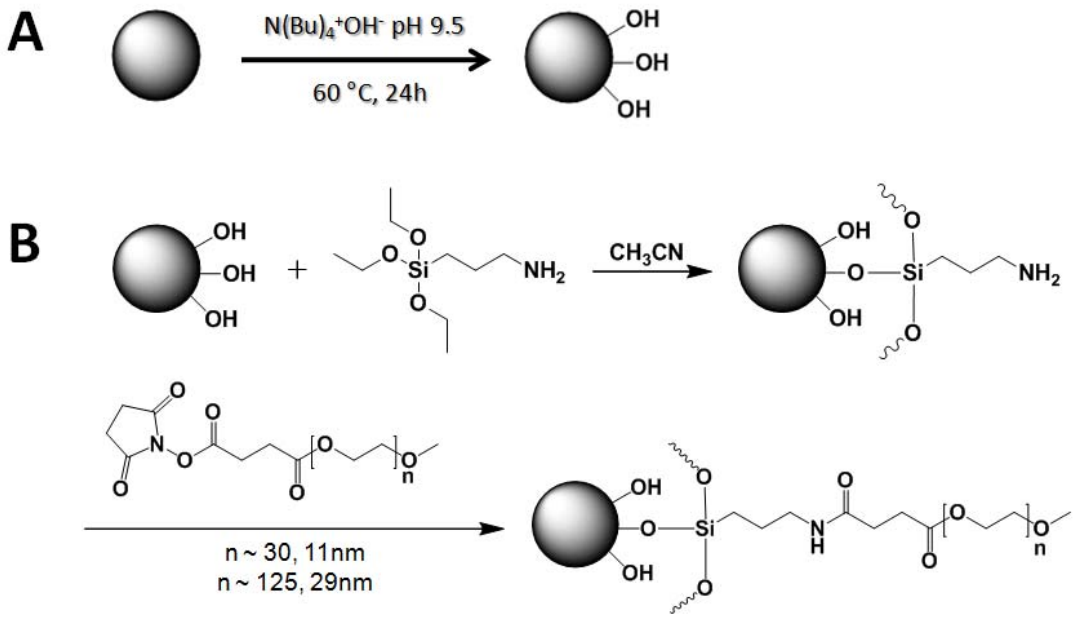

Figure 5.2. Schematic for the surface modifications of silica: (A) rehydroxylation and (B) PEGylation.

conjugation of activated PEG chains to the primary amine groups occurred in a facile reaction involving a nucleophilic attack of the $–NH_2$ on the carbonyl C of the succinimidyl succinate ester (Figure 5.2) to form an amide linkage. This process was also carried out in colloidal solution to afford TEM images (Figure 5.3) that clearly showed the success of the PEGylation via the appearance of a uniform organic coating enveloping each individual nanoparticle. These modifications were also monitored via ζ-potential measurements. The installment of the silamines was verified by the change from ζ -46.45 to +38.13 mV as a result of the presence of protonated amine groups in water. Upon PEGylation, the ζ decreased to -3.99 mV due to the conversion of amines to amide groups.

TGA was employed for loose silica spheres of varying diameters to quantify the surface coverage with PEG chains. Its results are summarized in Table 5.4. All samples remained white in color after heat treatment up to 800 °C, which assured the complete combustion of all organic matter that were removed as volatile components (as opposed to forming a black soot as typical of incomplete combustion). Comparison of derivative TGA curves (Figure 5.4) for aminated and PEGylated samples showed % weight loss from 494 to 602 °C may be attributed to the

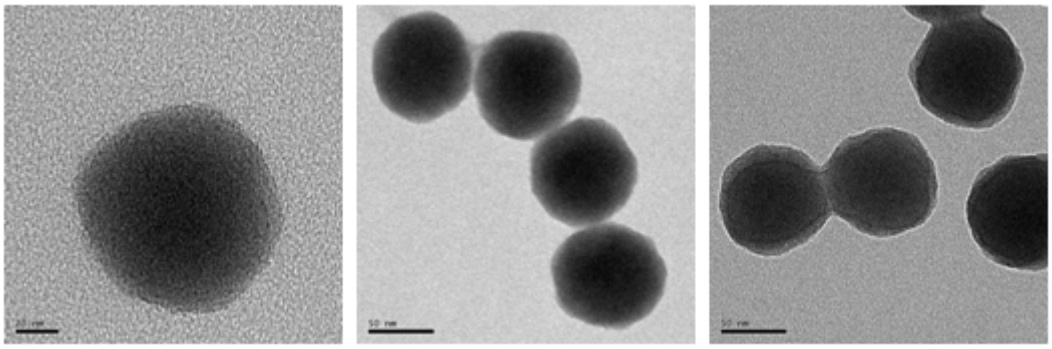

Figure 5.3. TEM images of (Left) bare (scale bar = 20 nm), (Middle) aminated (scale bar = 50 nm) and (Right) PEGylated silica spheres of 50 nm nominal diameter (scale bar = 50 nm).

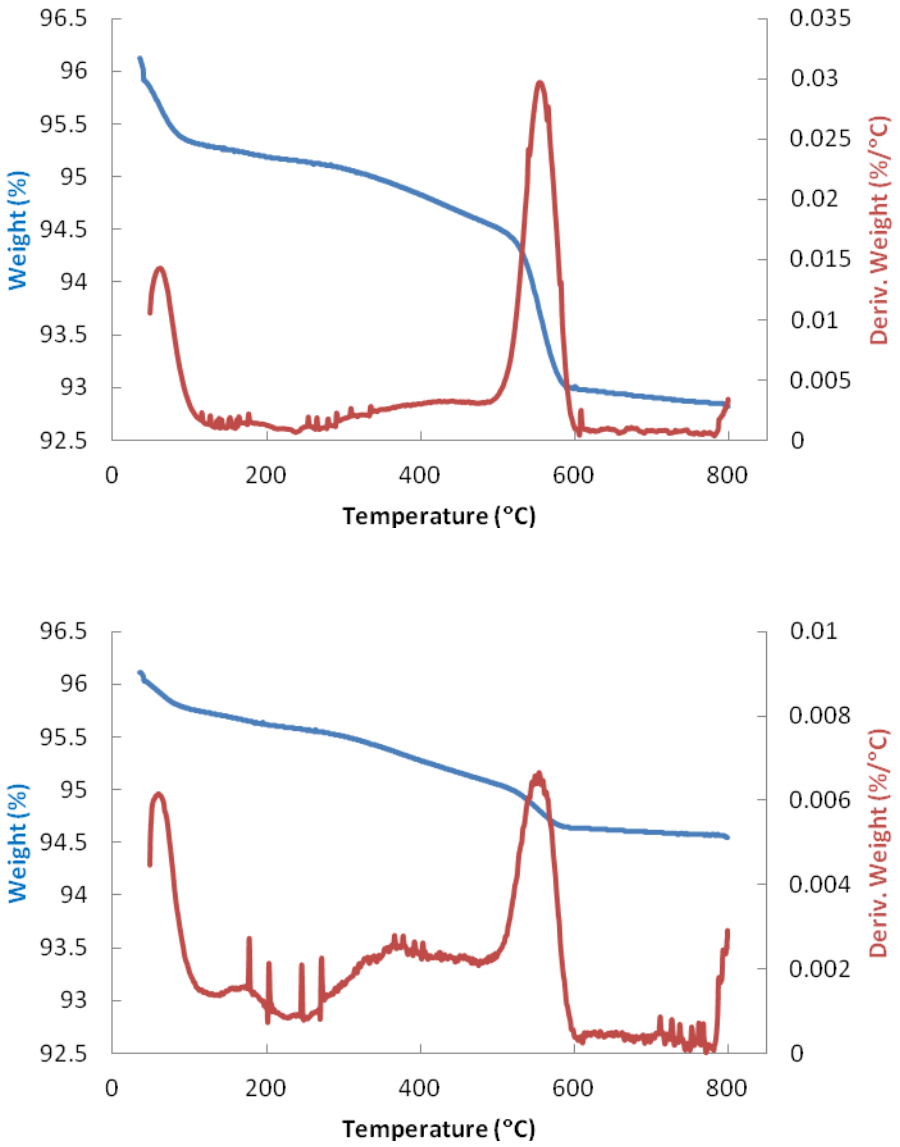

Figure 5.4. Comparison of the TGA curves for (Top) aminated and (Bottom) PEGylated silica.

Table 5.4. Summary of calculated results from TGA data.

Nanoparticle diameter (nm)[a]	% Weight loss	Surface density
84 ± 6	0.614% to 210 °C	
	0.495% to 500 °C	0.029 PEG chain/nm^2
	0.215% to 628 °C	4.88 –NH_2/nm^2 (monolayer)
346 ± 20	0.387% to 203 °C	
	0.551% to 496 °C	0.313 PEG chain/nm^2
	0.487% to 795 °C	27.6 –NH_2/nm^2 (~7 layers)
427 ± 30	1.864% to 203 °C	
	1.431% to 800 °C	0.324 PEG chain/nm^2
	0.805% to 800 °C[b]	14.2 –NH_2/nm^2 (~3 layers)

[a] From SEM measurements
[b] From a separate TGA of aminated spheres

degradation of silamines, while PEG was lost from 227 to 500 °C. These results are in agreement with an extensive study by Madathringal and Wunder[36] where neat PEG was observed to degrade at 350 – 440 °C whereas physisorbed PEG were removed at 180 – 300 °C depending on H-bond formation between PEG carbonyl O and silanol H atoms. That we observed PEG loss up to >400 °C was indicative of covalent tethering of the PEG chains onto our silica surfaces rather than mere physisorption. Table 5.4 shows TGA data suggesting that (at our current best optimization of reaction conditions) silica spheres of diameter 346 ± 20 and 427 ± 30 nm have similar PEG coverage. A 10-fold smaller surface density was calculated for silica nanoparticles of smaller size. This correlated well with the concept of increased number of contacts points

between PEG and silica with increasing ratio of particle to PEG size.[36] As the size of PEG approached that of the silica sphere, fewer contact points were possible since the polymer chains would need to adopt energetically unfavorable conformations in order to form amide linkages with amines on the surface. For the free-standing membranes, it is most likely the PEG chains remained close to the silica surface rather than freely extending to the center of the nanopore due to the modest surface density.

We then sought to evaluate the effectiveness of PEG chains in suppressing protein adsorption onto silica surfaces. From the UV-Vis absorbance measurements of remaining dissolved proteins in supernatant aliquots prior to and after incubation of unmodified and PEGylated loose silica spheres (under buffer conditions matching those of the diffusion experiments), we verified the usefulness of PEG layers in minimizing nonspecific protein binding. We preferred a spectroscopic method over a gravimetric determination because the free proteins in the supernatant cannot be completely removed by repetitive rinsing without introducing inaccuracies since the adsorption may be reversible.[33] On the other hand, if the particles were not washed, dissolved protein in residual supernatant would have given erroneously higher mass losses in TGA. The silica nanoparticles were isolated from the supernatant by centrifugation at speeds that were suitably low so as not to cause sedimentation of the dissolved proteins from solution (which would have also resulted in a positive bias for amount of adsorbed protein). Lz adsorption was decreased in half while BHb fouling was reduced by a factor of 1.6 (Table 5.5). A slight improvement in extent of BSA binding was also observed despite the fact that the fouling was already low even for unmodified particles due to electrostatic repulsion of the anionic protein from the like-charged silica surfaces. Particularly for the cationic proteins, the significant biofouling was indicative of less than optimal surface coverage with PEG chains.

Table 5.5. Summary of amount of adsorbed protein onto silica surfaces.

	Lysozyme	Bovine Hemoglobin	Bovine Serum Albumin
		Unmodified	
mmol protein/g silica	1.29×10^{-3}	1.63×10^{-3}	2.88×10^{-4}
protein/nm^2	0.223	0.284	0.050
% adsorbed protein	23.3	38.6	6.9
		PEGylated	
mmol protein/g silica	6.26×10^{-4}	1.24×10^{-3}	2.25×10^{-4}
protein/nm^2	0.109	0.217	0.039
% adsorbed protein	12.0	23.8	5.7

Diffusion through PEGylated membranes

Figure 5.5 shows surprising trends in the protein diffusion through PEGylated nanopores (19 nm 'radius') with diffusion rates increasing in the order BSA > Lz > BHb. Lz still diffused 1.8 times faster than BHb and good selectivity for BSA over BHb (ca. 6) was once again evident. That BSA was transported at higher rates than the smaller protein Lz through PEGylated membranes revealed that while cationic protein flux was hindered due to adsorption (and possibly pore blockage), anionic proteins also experienced hindered transport through as-sintered nanofrits due to protein-nanopore wall charge repulsion. The presence of PEG on the silica surface effectively screened the BSA from the negative silica charges and contributed to almost doubled transport rates through PEG-modified pores compared to as-sintered membranes (Figure 5.6). BHb diffusion rates were comparable through PEGylated and as-sintered nanopores (Figure 5.7).

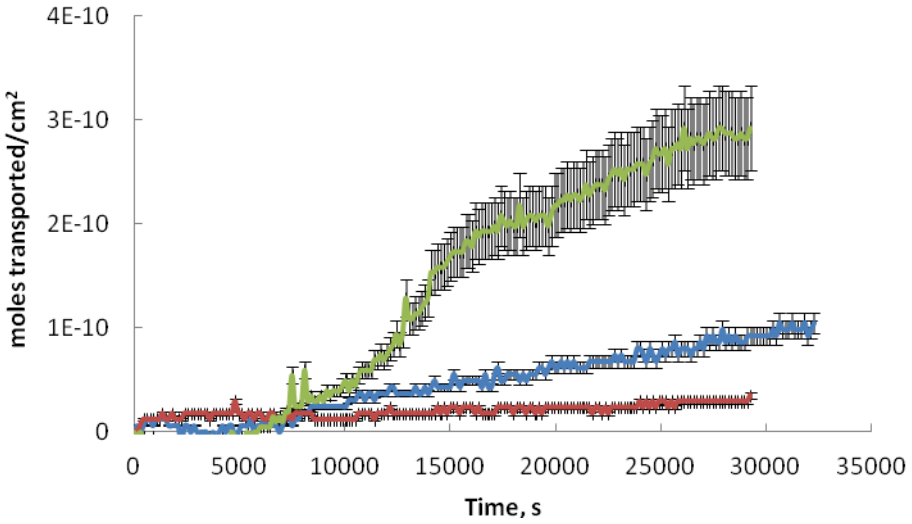

Figure 5.5. Comparison of the flux of Lz (blue), BHb (red) and BSA (green) through PEGylated frits with 19 nm pore 'radius'.

Table 5.6. Summary of protein average D_{eff} (cm^2/sec) as measured through PEGylated nanofrits.

Nanopore radius (nm)	18.9	27.2
Lysozyme	$(9 \pm 2) \times 10^{-7}$	$(2.0 \pm 0.6) \times 10^{-6}$
Bovine Hemoglobin	$(5 \pm 1) \times 10^{-7}$	$(6.1 \pm 0.2) \times 10^{-7}$
Bovine Serum Albumin	$(3 \pm 1) \times 10^{-6}$	$(1.33 \pm 0.02) \times 10^{-6}$

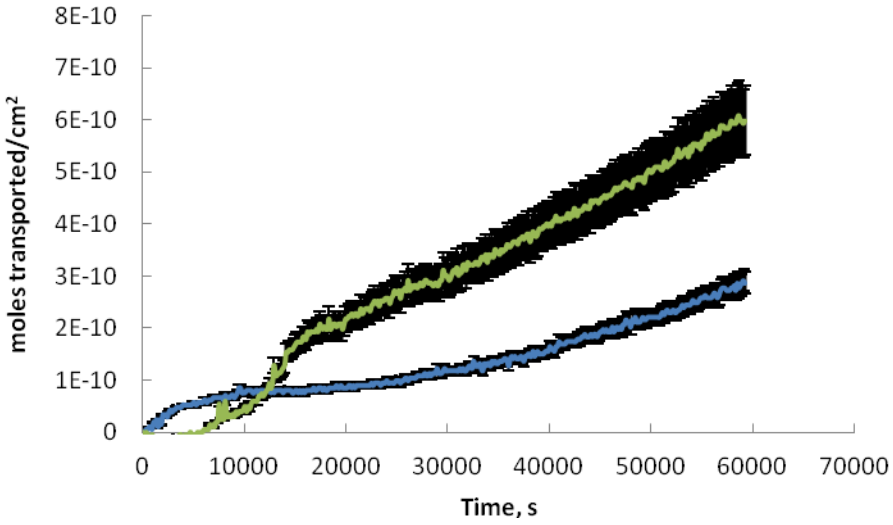

Figure 5.6. Comparison of the flux of BSA through as-sintered (blue) and PEGylated (green) membranes (of comparable 19 nm pore 'radii').

Even though it appeared that PEGylation improved the transport rates of BSA and BHb, it was unclear why Lz diffusion was hindered through these nanopores (Figure 5.8). To explain the effect of surface PEGylation on Lz transport, more studies are necessary to fully understand the interactions between the protein and PEG chains. A mapping of surface potentials as well as simulations of interaction strengths as a function of relative orientation will be needed for this investigation.

PEGylated membranes of larger nanopore 'radius' (27 nm) were also constructed and studied. The D_{eff} values are summarized in Table 5.6. Generally, transport rates were higher through these pores of increased diameter. In addition, the pores were sufficiently wide that any possible steric hindrance to flux (due to PEG chains) was not evident such that rates of transport were in the typical order of Lz > BSA > BHb. A BSA/BHb selectivity of 2.2 persisted even with the use of nanopores this large.

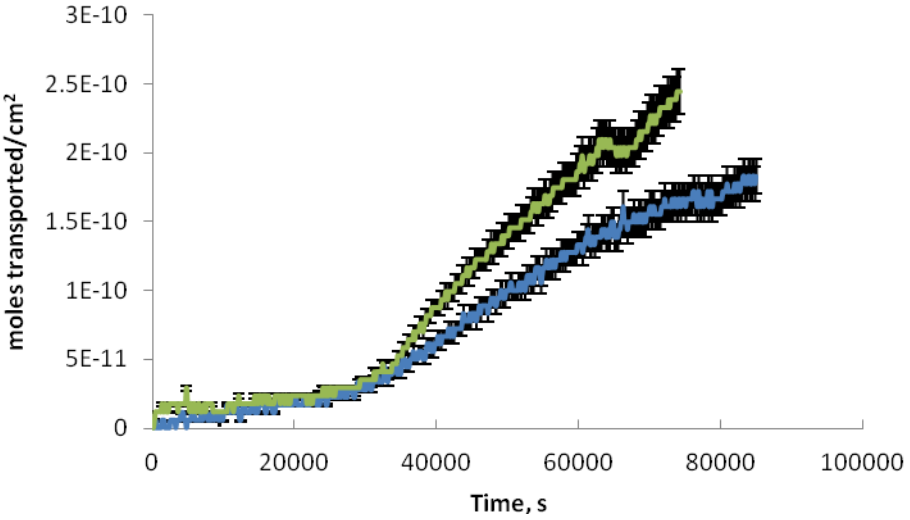

Figure 5.7. Comparison of the flux of BHb through as-sintered (blue) and PEGylated (green) membranes (of comparable 19 nm pore 'radii').

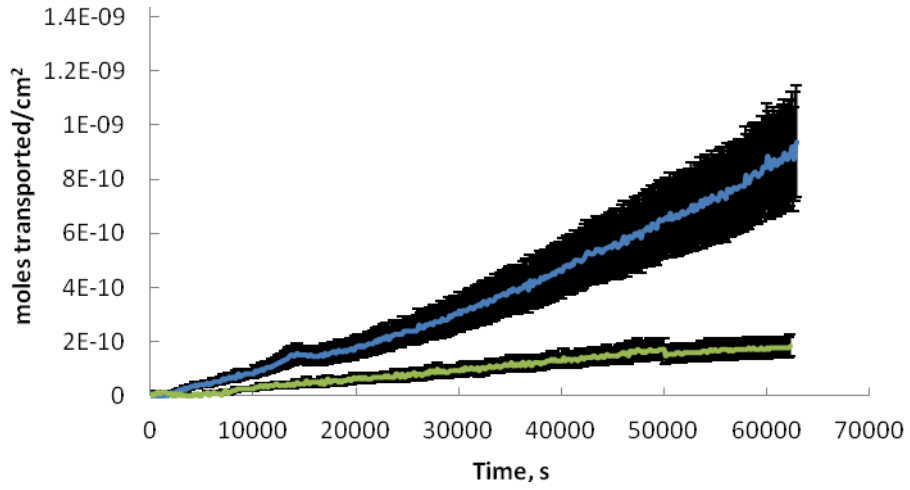

Figure 5.8. Comparison of the flux of Lz through as-sintered (blue) and PEGylated (green) membranes (of comparable 19 nm pore 'radii').

Finally, in an effort to evaluate the separations capabilities of our PEGylated free-standing membranes (nanopore 'radius' 19 nm) for real-life applications, two-species diffusion experiments were performed. To account for absorbance of BHb in the UV region, its concentration was first determined from the Vis absorbance and subtracted from the total absorbing species at the λ_{max} for BSA. The selectivity for BSA in a mixture with BHb was significantly lower than the selectivity (1.5 < 6) calculated from single-species diffusion experiments. More work will be needed to understand why the selectivity is lower. We speculate that this might be due to protein-protein electrostatic attractions between cationic BHb and anionic BSA that could deter the flux of the latter. This rationalization was consistent with calculated average D_{eff} of (6.5 ± 0.5) × 10^{-7} and (9 ± 2) × 10^{-7} cm^2/sec for BHb and BSA, respectively.

Conclusions

We showed that the transport of proteins across silica colloidal membranes depends strongly on nanopore size and surface functionality. Overall, the membranes studied in this work exhibited size-selective transport where smaller proteins generally diffused faster. Larger pores led to higher throughput but at the cost of selectivity. In addition to size-selectivity, we also demonstrated that these membranes have promising ability of discriminating according to shape between biomolecules of comparable molecular weight, unlike conventional dialysis membranes that would have failed since they operate on the basis of a molecular weight cut-off.

These results are more complicated than we can explain with the current preliminary data. Presently, we propose that protein-nanopore interactions determine the rate at which proteins are transported, wherein both cationic and anionic species can experience hindered flux due to different mechanisms. As a result of electrostatic attraction, cationic proteins adsorb significantly on the surfaces, producing a layer that effectively reduces pore volume due to partial blockage. As a result of electrostatic repulsion between similarly-charged anionic proteins and

nanopore wall, there may be a low extent of nonspecific protein binding but the flux was nevertheless decreased. We propose that separation efficiencies could be improved by incorporating charge selectivity along with size exclusion in the nanopores. This can be achieved by controlling the pH (depending on the *p*I of the proteins of interest) and modifying the nanopore surface to bear excess positive or negative charges. Transport selectivity based on affinity could also be achieved using this colloidal crystal platform via conjugation of specific and selective receptor moieties such as antibodies to capture one component from a mixture. Overall, extensive work is needed to transition from the promising preliminary results described in this chapter to a functional protein separation system based on colloidal nanofrits.

References

(1) a) Sang, L.-C.; Vinu, A.; Coppens, M.-O. *Langmuir* **2011**, *27*, 13828. b) Hou, X.; Guo, W.; Jiang, L. *Chem. Soc. Rev.* **2011**, *40*, 2385.

(2) Wang, J.; Liu, B. *Chem. Commun.* **2009**, *45*, 2284.

(3) Zhang, M.; He, X.; Chen, L.; Zhang, Y. *Nanotechnology* **2011**, *22*, 065705.

(4) Heller, C.; Beck, S. *Electrophoresis* **1993**, *14*, 162.

(5) Chang, C.-S.; Ni, H.-S.; Suen, S.-Y.; Tseng, W.-C.; Chiu, H.-C.; Chou, C.P. *J. Membr. Sci.* **2008**, *311*, 336.

(6) Ke, X.B.; Shao, R.F.; Zhu, H.Y.; Yuan, Y.; Yang, D.J.; Ratinac, K.R.; Gao, X.P. *Chem. Commun.* **2009**, *45*, 1264.

(7) Tomanee, P.; Hsu, J.T. *Biotechnol. Prog.* **2006**, *22*, 532.

(8) Wang, Z.; Le, G.; Shi, Y.; Węgrzyn, G. *Biotechnol. Lett.* **2002**, *24*, 121.

(9) Mohamed, H.; Szarowski, D.H.; Lepak, L.A.; Spencer, M.G.; Martin, D.L.; Caggana, M.; Turner, J.N. *NSTI-Nanotech* **2005**, *1*, 446.

(10) Nge, P.N.; Yang, W.; Pagaduan, J.V.; Woolley, A.T. *Electrophoresis* **2011**, *32*, 1133.

(11) Peng, X.; Jin, J.; Ichinose, I. *Adv. Funct. Mater.* **2007**, *17*, 1849.

(12) Yu, S.; Lee, S.B.; Kang, M.; Martin, C.R. *Nano Lett.* **2001**, *1*, 495-498.

(13) Yusko, E.C.; Johnson, J.M.; Majd, S.; Prangkio, P.; Rollings, R.C.; Li, J.; Yang, J.; Mayer, M. *Nature Nanotechnology* **2011**, 6, 253.

(14) Hu, H.; Zhou, H.; Du, J.; Wang, Z.; An, L.; Yang, H.; Li, F.; Wu, H.; Yang, S. *J. Mater. Chem.* **2011**, *21*, 6576.

(15) Rosen, J.E.; Gu, F.X. *Langmuir* **2011**, *27*, 10507.

(16) Bharti, B.; Meissner, J.; Findenegg, G.H. *Langmuir* **2011**, *27*, 9823.

(17) White, R.J.; Evin, E.N.; Yang, T.; Chen, X.; Daniel, S.; Cremer, P.S.; White, H.S. *J. Am. Chem. Soc.* **2007**, *129*, 11766.

(18) Segat, D.; Tavano, R.; Donin, M.; Selvestrel, F.; Rio-Echevarria, I.M.; Rojnik, M.; Kocbek, P.; Kos, J.; Iratni, S.; Scheglmann, D.; Mancin, F.; Dusi, S.; Papini, E. *Nanomedicine* **2011**, *6*, 1027.

(19) Daniels, C.R.; Reznik, C.; Kilmer, R.; Felipe, M.J.; Tria, M.C.R.; Kourentzi, K.; Chen, W.-H.; Advincula, R.C.; Willson, R.C.; Landes, C.F. *Colloids Surf., B* **2011**, *88*, 31.

(20) Lee, S.W.; Shang, H.; Haasch, R.T.; Petrova, V.; Lee, G.U. *Nanotechnology* **2005**, *16*, 1335.

(21) Popat, K.C.; Gopal Mor, G.; Grimes, C.A.; Desai, T.A. *Langmuir* **2004**, *20*, 8035.

(22) Ignacio-de Leon, P.A.; Zharov, I. *Chem. Commun.* **2011**, *47*, 553.

(23) Du, Y.J.; Brash, J.L. *J. Appl. Polym. Sci.* **2003**, *90*, 594.

(24) Newton, M. R.; Morey, K. A.; Zhang, Y.; Snow, R. J.; Diwekar, M.; Shi, J.; White, H. S. *Nano Lett.* **2004**, *4*, 875.

(25) Leoni, L.; Attiah, D.; Desai, T. A. *Sensors* **2002***, 2,* 111.

(26) Smith, C.; Kirk, R.; West, T.; Bratzel, M.; Cohen, M.; Martin, F.; Boiarski, A.; Rampersaud, A.A. *Diabetes Technol. Therap.* **2005**, *7*, 151.

(27) Pujar, N.S.; Zydney, A.L. *J. Chromatogr., A* **1998**, *796*, 229.

(28) Chun, K.-Y.; Mafé, S.; Ramírez, P.; Stroeve, P. *Chem. Phys. Lett.* **2006**, *418*, 561.

(29) Rohani, M.M.; Zydney, A.L. *J. Membr. Sci.* **2009**, *337*, 324.

(30) Cussler, E.L. *Diffusion: Mass Transfer in Fluid Systems, 2nd ed.*; Cambridge University Press: New York, 1997.

(31) Hart, T.K.; Pino, R.M. *The American Journal of Anatomy* **1986**, *175*, 49.

(32) Bhatia, S.K.; Bonilla, M.R.; Nicholson, D. *Phys. Chem. Chem. Phys.* **2011**, *13*, 15350.

(33) Holt, P.F.; Bowcott, J.E.L. *AMA Arch. Ind. Hyg. Occup. Med.* **1954**, *9*, 503.

(34) Ioffe, V.M.; Gorbenko, G.P.; Kinnunen, P.K.J.; Tatarets, A.L.; Kolosova, O.S.; Patsenker, L.D.; Terpetschnig, E.A. *J. Fluoresc.* **2007**, *17*, 65.

(35) Heyes, C.D.; Groll, J.; Möller, M.; Nienhaus, G.U. *Mol. Biosyst.* **2007**, *3*, 419.

(36) Madathingal, R.R.; Wunder, S.L. *Thermochim. Acta* **2011**, *523*, 182-186.

CHAPTER 6

SUMMARY AND OUTLOOK

Summary

In this thesis, we focused on the preparation and investigation of free-standing silica colloidal membrane materials for applications in separations.

First, we prepared Au-coated silica colloidal membranes and modified their surface with poly(methacrylic acid), with the goal of creating a pH- and ion-responsive membrane. The use of a gold surface increased the surface density of organic modifiers compared to a silica surface, provided a method for nanopore size manipulation and allowed us to explore new types of nanopore surface modification. We found that the diffusion through polymer-modified membranes increased when the polymer conformation changed from extended to collapsed at low pH and in the presence of ions that interact with the polycarboxylate.

Next, we prepared silica colloidal membranes which are modified with chiral selectors such as small molecules or polymers of amino acid derivatives. The diffusion studies of enantiomers of a chiral probe molecule through these membranes showed the potential of the membranes for chiral recognition and enantiopermselectivity, most likely due to differences in the strength of noncovalent interactions between the surface selector and the chiral probe.

We next explored the size-selectivity of silica colloidal membranes by studying the diffusion of various generations of poly(amidoamine) dendrimers. We found that the selectivity is enhanced by the tortuous path diffusing molecules take through the membrane.

This was followed by the preparation of silica colloidal membranes modified with poly(ethylene glycol) as an anti-fouling layer inside the nanopores. The diffusion rates of proteins were dependent on the protein size, nanopore size and nanopore surface functionality. With the use of a 7.5 nm pore 'radius', we observed a cut-off for bovine hemoglobin whereas lysozyme and bovine serum albumin diffused through the membrane.

Overall, this work demonstrates that we are able to control the molecular transport at the nanoscale via the modification of nanopore size and surface functionality. This thesis has illustrated that silica colloidal membranes can be prepared with transport selectivity based on size, charge and molecular recognition.

Future Directions

The results in Chapters 3 and 4 have shown the trade-off between throughput and selectivity with the use of smaller nanopores. This highlighted the need to minimize non-selective diffusion, which can be achieved by reducing the pore size or by filling the pore volume with polymers bearing functional groups for maximized interactions with a diffusing species of interest. To obtain smaller nanopores (< 5 nm), silica colloidal membranes can be prepared from sub-100 nm silica nanospheres. However, the production of membranes with large dimensions (at least 1 cm^2 and 0.2 cm thickness) remains a challenge. Thus, there is a need to optimize the conditions for the preparation of good quality colloidal membranes (i.e. of uniform thickness, free of major defects such as cracks) from sub-100 nm spheres. The quality of the colloidal crystals is dependent on the colloidal solution concentration, solvent, temperature and the rates of deposition and solvent evaporation. The effect of these variables on the thickness of the resulting colloidal membranes must be systematically studied.

Chiral selectivity can also be improved with increased surface density of selector moieties. To this end, it might be beneficial to employ Au-coated membranes whose surfaces can be modified with SAMs of up to 10 thiols/nm^2. Synthetic organic and polymer chemistry can be

used to incorporate surface-bound moieties that can control the size and chemical function of the nanopore by: (1) acquiring charges via protonation/deprotonation,[1,2] binding of ions, and oxidation; (2) changing conformation in response to external stimuli such as temperature, pH, light and binding of ions and/or molecules. For example, modification with ionizable polypeptides that can undergo helix/coil transitions (e.g., poly(*L*-glutamic acid)) [3-5] can be used to control the sterics inside the nanopore.

The work outlined in Chapter 5 represents a preliminary study of the application of silica colloidal membranes for biomolecule separations. Future work on this project should involve studying the diffusion of proteins as a function of pH. Variation of pH to match the p*I* of a particular protein such that other proteins in the solution will be positively and/or negatively charged can be exploited to impart charge-selectivity in addition to size exclusion. Surface modification with PEG was shown to be effective in reducing the extent of nonspecific protein adsorption, but the exact mechanism for this nonfouling property remains to be fully understood.[6] To optimize the selectivity in nanopores modified with PEG, its interactions with proteins must be elucidated. One way to do this is to simulate the strength of protein-PEG interactions as a function of protein orientation, PEG conformation and solution pH by mapping the surface potential of both protein and nanopore using computational methods. Other studies that can be conducted include the diffusion of linear biopolymers through the colloidal membranes. The diffusion rates for 3 kb and 10 kb double-stranded DNA (dsDNA)[7] can be monitored via fluorescence spectroscopy by labeling the DNA with a fluorophore (e.g., YOYO-1).[8]

References

(1) Lee, S.B.; Martin, C.R. *Anal. Chem.* **2001**, *73*, 768.

(2) Bao, Z.; Bruening, M.L.; Baker, G.L. *J Am. Chem. Soc.* **2006**, *128*, 9056.

(3) Whitesell, J.K.; Chang, H.K. *Science* **1993**, *261*, 73.

(4) Smuleac, V.; Butterfield, D.A.; Bhattacharyya, D. *Chem. Mater.* **2004**, *16*, 2762.

(5) Ito, Y.; Park, Y.S.; Imanishi, Y. *Langmuir* **2000**, *16*, 5376.

(6) Heyes, C.D.; Groll, J.; Möller, M.; Nienhaus, G.U. *Mol. Biosyst.* **2007**, *3*, 419.

(7) Robertson, R.M.; Laib, S.; Smith, D.E. *Proc. Natl. Acad. Sci. U.S.A.* **2006**, *103*, 7310.

(8) Pluen, A.; Netti, P.A.; Jain, R.K.; Berk, D.A. *Biophys. J.* **1999**, *77*, 542.